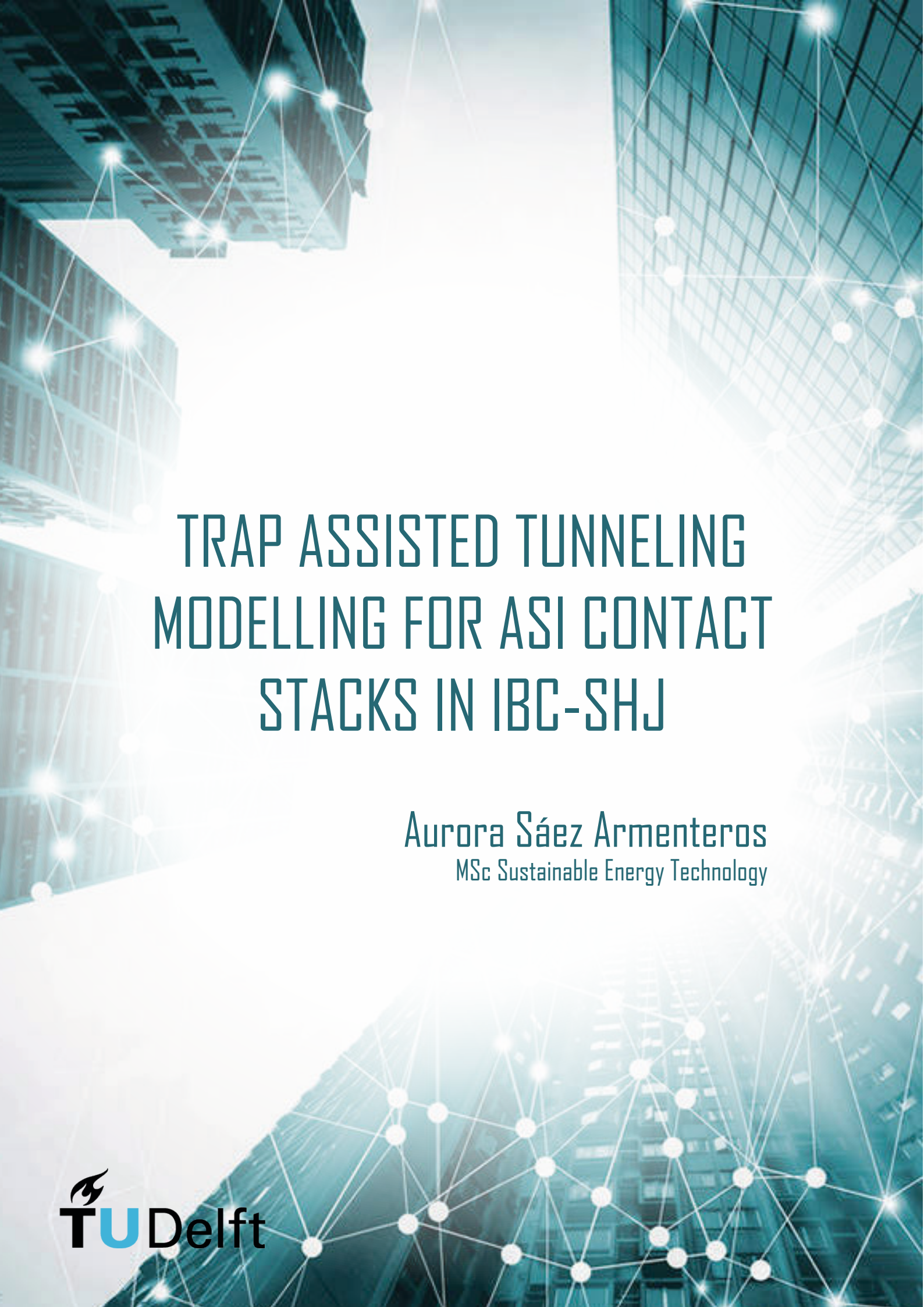

TRAP ASSISTED TUNNELING MODELLING FOR ASI CONTACT STACKS IN IBC-SHJ

Aurora Sáez Armenteros
MSc Sustainable Energy Technology

TU Delft

Trap assisted tunneling modelling for aSi contact stacks in IBC-SHJ

by

A. Sáez Armenteros

in partial fulfillment of the requirements for the degree of

Master of Science
in Sustainable Energy Technology

at the Delft University of Technology,
to be defended publicly on September 21, 2018 at 14:00 PM.

Student number: 4631226
Project duration: September 7, 2017 – September 21, 2018
Thesis committee:

Dr. ir. O. Isabella	TU Delft, ESE - PVMD	Supervisor
Dr. P. A. Procel Moya	TU Delft, ESE - PVMD	Daily supervisor
Prof. dr. ir. M. Zeman	TU Delft, ESE - PVMD	Head of the ESE Department
Dr. Ir. M. Mastrangeli	TU Delft, ME - ECTM	External committee member

TU Delft Delft University of Technology

Abstract

Interdigitated back contact silicon heterojunction (IBC-SHJ) solar cells have demonstrated 26.6% world record efficiency by combining outstanding passivation of Si thin film layers with the absence of front shading contact in the crystalline silicon (c-Si) absorber bulk. Furthermore, this type of solar cell merges advantages of c-Si with Si thin film technology that allows for adjustment and tuning of bandgap and Fermi energy in deposited layers, and thus, modifying material properties that also impact the carrier collection. As heterointerfaces tailor to band offset and potential barriers for collecting carriers, the transport is described by thermionic emission and tunneling mechanisms. Moreover, Si thin film layers typically exhibit a defective matrix with characteristic traps and charge distribution that affect solar cell external parameters. Such phenomena involves the so called trap assisted tunneling (TAT) together with trap recombination mechanisms in a complex physical system.

In this work, the effect of TAT mechanisms on IBC-SHJ is studied by means of numerical simulations based on TCAD Sentaurus. Firstly, the TAT model is implemented as non-local process. It was found that TAT exhibits a negligible effect on electron collection, but dominates transport mechanisms in case of hole contact. Such an effect depends on band alignment at the doped layer/transparent conductive oxide (TCO) interface, where band-to-band tunneling in combination with TAT describe the transport of holes. In particular, TCO carrier concentration in combination with activation energy of deposited layer allows the collection by either TAT or band-to-band tunneling. In more detail, the density of traps described typically as dangling bond improves the transport of collecting carriers. Thus, the collection of carriers is evaluated in terms of energy and trap concentration, demonstrating that traps with an energy level of 0.5 to 0.7eV over the valence band enhances the FF, and thus, the solar cell performance.

Finally, the complete model is calibrated by comparing measured with simulated external parameters from a reference solar cell with and without TAT mechanisms. From this analysis, it is demonstrated that solar cell external parameters deploys more consistent values for Shockley-Read-Hall (SRH) recombination associated to bulk lifetime and surface recombination velocity using TAT model.

Preface

This master thesis marks the end of my studies in Delft, as well as the start of a new beginning. Looking back in these two last years, I can not help but smile. They have been full of incredible experiences and fantastic people, that made this time unforgettable. In here, not only I gained a deep understanding in sustainable energy technologies, but also in so many other aspects of life.

Completing this thesis was a beautiful challenge. A challenge that could have not been completed without the help of many people. First of all, I would like to thank Paul, my daily supervisor, for his guidance and support. He transmitted me his passion for semiconductor physics and patiently taught me how to use Sentaurus and how not to lose my nerve while trying. I thank him for his availability and kindness, for enriching me as a student and as a person. Moreover, my gratitude goes to Dr. ir. Olindo Isabella, my main supervisor, for letting me carry out this project under his guidance. I thank him for his valuable insights and for his dedication. I would also like to express my gratitude to all the cSi cluster, for showing interest in my thesis progress and for their fruitful comments during our meetings. Furthermore, thanks to Prof. dr. ir. Miro Zeman and Dr. ir. Max Mastrangeli for their willingness to being part of my graduation committee.

I would also like to thank all the people that supported me along the completion of this project. Thanks to Delft S.E.A and all the SETies for all the good times. Big thank you to my friends in Spain, to Celia, Cristina, Lucia, and of course to *trivial*, for supporting me from the distance. Thanks to my PV colleagues - Julen, Paolo, Andrés, Simona, Chris and Haiyuan - for the coffee breaks, the discussions and the support, especially in the last weeks. Furthermore, my gratitude goes to my housemates and all OP1 friends - Anna, Thomas, Michael, Bea, and Michael Houlder - for their constant support, for the BBQs and for all the late chats in the kitchen. Also, I would like to thank Ali, for supporting me from the start. Thanks to Anna Filippi, because I can always count on her, even for making my thesis cover. Special thanks to Michael, for being patient enough to correct my grammar and to fix the latex template, but most importantly, thank you for being there.

Finally, I want to thank my family, because they made this possible. Thanks to my parents for their endless care, and thanks to Jose and Kasia for always believing in me and making me believe in myself. *Gracias familia, os quiero.*

A. Sáez Armenteros
Delft, September 2018

Contents

List of Figures

List of Tables

List of Symbols

Latin Symbols

A^*	Richardson Constant for Thermionic Emission	J_{sc}	Short Circuit Current
c_i^n	Electron Capture Rate	J_{Tun}	Tunneling Current
C_p	Auger Coefficient for holes	k	Boltzmann Constant
C_n	Auger Coefficient for electrons	m_e	Tunneling mass of Electron
D	Diffusion Coefficient	m_h	Tunneling mass of Hole
e_i^n	Electron Emmision Rate	n	Electron Density
$\vec{E}$	Electric Field	n_i	Intrinsic Density
E_a	Activation Energy	$n_{i,eff}$	Effective Intrinsic Density
E_{C0}	Characteristic Energy of CBT	N_0	Trap density (SRH)
E_{DB}	Center of dangling bond distribution	N_A	Ionized Acceptor Atom
E_e	Electrostatic Potential of Electron	N_{C0}	Conduction Band Tail Density
E_{fe}	Quasi Fermi Level of Electron	N_{CBT}	CBT density of states
E_{fh}	Quasi Fermi level of Hole	N_D	Ionized Donor Atom
E_F	Fermi level	N_{DB}	Dangling Bond Density
E_h	Electrostatic Potential of Hole	N_{V0}	Valence Band Tail Density
E_T	Trap energy level	N_{VBT}	VBT density of states
E_{trap}	Trap Energy	p	Hole Density
E_{V0}	Characteristic Energy of VBT	q	Elemental Electrical Charge
f^n	Occupation of Traps by Electrons	r	Distance
f^p	Occupation of Traps by Holes	r_i^n	Emission rate
g	Degeneracy factor	R	Recombination Rate
G_{Tun}	Local Generation Current	$R_{net,n}$	Net Recombination Rate
h	Planck Constant	SRV	Surface Recombination Velocity
J	Current Due to Thermionic Emission	T	Temperature
$\vec{J}_{diff}$	Diffusion current	v_{th}	Thermal velocity
$\vec{J}_{drift}$	Drift current	V_{bi}	Built-in Voltage
$\vec{J}_n$	Current Electron Density	V_{oc}	Open Circuit Voltage
$\vec{J}_p$	Current Hole Density		

Greek Symbols

Γ_e	Tunneling Probability of Electron
Γ_h	Tunneling Probability of Hole
δ	Excess Carrier Generation
ΔE_C	Conduction Band Offset
ΔE_G	Energy Band Offset
ΔE_V	Valence Band Offset
ϵ	Relative Permitivity
ϵ_0	Relative Permitiviy in Vacuo
ε	Energy Level
λ	Wavelength
μ	Mobility
ρ	Charge density
σ_{db}	Standard deviation of dangling bond Gaussian distribution
σ	Capture cross section
τ	Minority Carrier Lifetime
τ^{SRH}	SRH Average Lifetime
τ_{eff}	Effective Lifetime
ϕ	Electrostatic Potential
χ	Electron Affinity
ψ_e	Electrostatic Potential Profile of Electron
ψ_h	Electrostatic Potential Profile of Hole

List of Acronyms

ARC	Anti-reflective Coating
aSi	Amorphous Silicon
BSF	Back Surface Field
BTBT	Band-to-band Tunnelling
CB	Conduction Band
CBT	Conduction Band Tail
CRN	Continuous Random Network
cSi	Crystalline Silicon
DB	Dangling Bonds
DOS	Density of States
EQE	External Quantum Efficiency
FCA	Free Carrier Absorption
FF	Fill Factor
FOM	Figures of Merit
FSF	Front Surface Field
FTPS	Fourier Transform Photocurrent
GaAs	Gallium Arsenide
IBC	Interdigitated Back Contact
SHJ	Silicon Heterojunction
SiN	Silicon Nitride
SWE	Staebler-Wronski Effect
TAT	Trap Assisted Tunneling
TMM	Transfer Matrix Method
TCO	Transparent Conductive Oxide
VB	Valence Band
VBT	Valence Band Tail
WKB	Wentzel-Kramers-Brillouin

1

Introduction

In response to the increasing global energy demand, photovoltaic installations have increased throughout the last decade, reaching 402.5GW of total installed capacity and and 97.5 GWp global production in 2017 [10]. Taking a closer look at the market, as shown in figure1.1, crystalline silicon (cSi) dominates the PV power production, having around 90% of the share. This is due to the high technological development, the material abundance and stability, and a considerably high conversion efficiency [11].

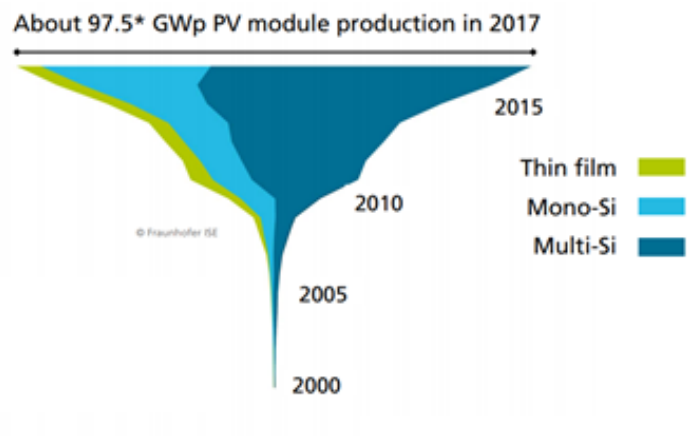

Figure 1.1: Annual PV production by technology [1].

Regarding cSi cell technologies, there are multiple concepts available in the market, as well as in the development stage. In figure 1.2a, the market trend for different cell technologies is illustrated, showing that PERC[1]/PERL[2]/PERT[3] technologies are expected to dominate the market. However, a rise in the market share is expected for back contacted cells and silicon heterojunctions (SHJ). Regarding back contacted cells, interdigitated back contact (IBC) architecture has achieved record results

[1]Passivated Emitter and Rear Cell
[2]Passivated Emitter Rear Locally-diffused
[3]Passivated Emitter Rear Totally Diffused

[12], [13] due to the absence of front shading. Furthermore, SHJ concepts have demonstrated excellent passivation quality, achieving high values for open-circuit voltage (V_{oc}) and fill factor (FF). Thus, by combining both configurations in IBC-SHJ, excellent results are achieved. In fact, this configuration holds the world record efficiency for single cell junctions at 26.6% (Kaneka [14].

Moreover, as shown in figure 1.2b, the market is expected to shift towards n-type silicon wafer, from the conventionally used p-type. Therefore, in this project the focus is on an IBC-SHJ cell, featuring n-type cSi bulk. Additionally, the silicon alloy used for the contacts is aSi, enabling a low temperature fabrication process.

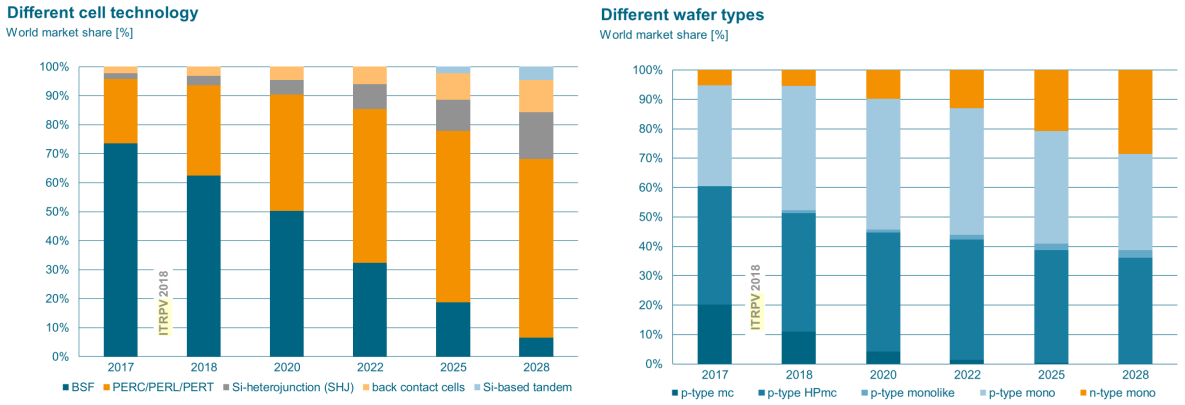

(a) (b)

Figure 1.2: Worldwide market shares for **a)** different cell technologies and **b)** different wafer types

Besides the excellent results reported for such configurations, the fabrication process requires further optimization so that eventually this cell technology allows the fabrication of cost competitive modules. In order to optimize the design process, it is crucial to reproduce the opto-electrical behaviour of this configuration by means of modelling.

From a physics point of view, IBC-SHJ configuration exhibits heterointerfaces, in which charge carrier transport is described by thermionic emission and tunneling mechanisms. Moreover, aSi layers, typically characterized by a distribution of defects, enable an additional transport mechanism - trap assisted tunneling (TAT). In addition, the presence of defects involve recombination processes, such as Shockley-Read-Hall. The combination of these phenomena results in a complex physical system, and therefore, one of the main challenges of modelling.

1.1. Motivation and outline of the thesis

The motivation of this work lies in the understanding of how the properties of the materials affects the band alignment in IBC-SHJ and thus influences the charge carrier transport. In order to do so, two main research questions are raised:

1. *Is TAT a dominating carrier transport mechanism in IBC-SHJ?*
2. *Can Sentaurus reproduce in detail the opto-electrical behaviour of an IBC-SHJ with aSi and ITO contact stacks?*

To be able to answer these questions, a background in semiconductor physics is presented in chapter 2, as well as the physical properties of the materials featured in IBC-SHJ. Furthermore, in chapter 3, the simulation approach used in semiconductor devices is described, highlighting the particularities of IBC-SHJ modelling. Then, in chapter 4 the implementation of TAT in Sentaurus TCAD is described. In addition, the TAT simulation results are discussed. Finally, in chapter 5 the opto-electrical calibration of the reference IBC-SHJ is performed.

2

Fundamentals

In this chapter, the fundamentals of semiconductor physics, heterojunction solar cells, and interdigitated back contact solar cell configuration will be described. Respectively, in section 2.1 the fundamental semiconductor equations are presented, focusing on transport in semiconductor junctions. Later, in section 2.2, the concept of silicon heterojunction solar cells and the materials used in this configuration will be elucidated. Lastly, in section 2.3, IBC-SHJ cell architecture is explained with detail. It is necessary to explore these concepts in order to understand the modelling of an IBC-SHJ cell and draw reliable conclusions from simulation results.

2.1. Semiconductor physics

In this section the fundamental physics of semiconductor materials are explained. It is crucial to understand the numerous parameters that are involved in the modelling of semiconductor devices. The drift-diffusion model is usually used to describe semiconductor device behaviour, in the next sections, the equations comprised in this modelled are presented.

2.1.1. Poisson equation

Two types of mobile charge carriers are considered: electrons (negative) and holes (positive). There are also immobile charges, which are ionized dopant atoms or traps. Hence, the total charge density can be written as shown in equation 2.1. The immobile charges are determined by the doping concentration of the semiconductor material being either n-type or p-type. The mobile charges are subject to the state in which the material is found, such as temperature, external voltage, lightning, etc.

$$\rho = q(p - n + N_D - N_A) - \rho_{trap} \tag{2.1}$$

where p and n are the hole and electron densities respectively, N_D and N_A are the ionized donor and acceptor atoms, ρ_{trap} is the charge contributed by traps and fixed charges, and q is the elemental electrical charge ($q = 1.602 \cdot 10^{-19} C$).

The density of both the mobile and immobile electric charges determines the electrostatic potential. The *Poisson equation*, shown in Equation (2.2), relates the electric charge density to the electrical potential.

$$\nabla \cdot (\nabla \phi) = -\frac{\rho}{\epsilon \epsilon_0} \tag{2.2}$$

where ϕ is the electrostatic potential, ϵ is the relative permitivity of the semiconductor, and ϵ_0 is the permitivity in *vacuo*.

Substituting 2.1 in 2.2 we obtain:

$$\nabla \cdot (\nabla \phi) = -\frac{1}{\epsilon \epsilon_0}\Big[q(p - n + N_D - N_A) - \rho_{trap}\Big] \tag{2.3}$$

2.1.2. Charge carrier transport

The charge carrier transport in semiconductors always obey the continuity equations, which describe charge conservation. There is a continuity equation for holes (2.4) as well as for electrons (2.5).

$$-\nabla \cdot \vec{J_p} = qR_{net,p} + q\frac{\partial p}{\partial t} \tag{2.4}$$

$$\nabla \cdot \vec{J_n} = qR_{net,n} + q\frac{\partial n}{\partial t} \tag{2.5}$$

where R_{net} is the net recombination rate, and $\vec{J_n}$ and $\vec{J_p}$ are the electron and hole current densities respectively. The current density is determined by the charge carrier transport within the semiconductor. Primarily, there are two basic transport mechanisms: drift and diffusion.

Drift

Drift is the motion of charge carriers caused by the presence of an electric field. The electric field accelerates the charge carriers, moving the holes in the direction of the field, and the electrons in the opposite direction. The average velocity of electrons and holes is proportional to the mobility (μ). The movement of the charge carriers leads to drift current of electrons (2.6) and holes(2.7).

$$\vec{J}_{drift,n} = -q \cdot n \cdot \mu_n \cdot \vec{E} \tag{2.6}$$

$$\vec{J}_{drift,p} = q \cdot p \cdot \mu_p \cdot \vec{E} \tag{2.7}$$

where $\vec{E}$ is the electric field.

Diffusion

Diffusion is the motion of charge carriers caused by a concentration difference within the semiconductor. As seen in equations 2.8 and 2.9, the diffusion current is proportional to the diffusion coefficient (D) and the concentration gradient.

$$\vec{J}_{diff,n} = qD_n \nabla n \tag{2.8}$$

$$\vec{J}_{diff,p} = -qD_p\nabla p \tag{2.9}$$

The *drift-diffusion model* takes into account the contribution of both drift and diffusion currents.

$$\vec{J}_n = \vec{J}_{drift,n} + \vec{J}_{diff,n} \qquad \vec{J}_p = \vec{J}_{drift,p} + \vec{J}_{diff,p} \tag{2.10}$$

2.1.3. Generation and recombination

In a non-illuminated semiconductor in equilibrium, the generation and recombination rates are equal. These processes take place due to the thermal excitement of the electrons in the lattice. However, when the semiconductor is exposed to illumination, there is an excess carrier generation ($\delta n, \delta p$) and recombination (R_n, R_p) which is defined as:

$$R_n = \frac{\delta n(t)}{\tau_{n0}} \tag{2.11}$$

The time that the excess minority carrier takes to recombine is determined by the minority carrier lifetime (τ). There are multiple recombination mechanisms. There are recombination mechanisms which are inherent to the properties of the material, one of which being the band structure. Other recombination mechanisms are related to defect density.

Radiative recombination

Radiative recombination consists of the recombination of an electron and a hole, with the emission of a photon. This type of recombination is characteristic of direct band gap materials, for example GaAs. This process is not very relevant for Silicon due to the indirect band gap. This type of recombination, together with the auger recombination, is intrinsic to the material energy band characteristics.

Auger recombination

As opposed to radiative recombination, when an electron and a hole recombine through auger recombination, a phonon emission takes place, instead of a photon. This implies that thermal energy is released into the lattice. Such a phenomenon is particularly important for indirect band materials such as Silicon and highly doped semiconductors. Conventionally, the net Auger recombination rate is expressed as follows:

$$R^A_{net} = (C_n n + C_p p)(np - n^2_{i,eff}) \tag{2.12}$$

where C_n and C_p are the Auger coefficients, and $n_{i,eff}$ is the effective intrinsic density. Currently, however, there are state of the art enhanced Auger recombination models. Once such model, proposed by [15], is used in this project. The model takes into consideration the recombination injection dependency for a range of dopant concentrations.

Shockley Read Hall recombination

Defects can often occur in the semiconductor crystalline structure. If the density of states of these defects is not too large, they will create a discrete energy state at the forbidden energy bandgap,

also called traps. These traps may act as recombination centers, and may capture and emit electrons or holes. We consider two different types of traps, donor-type and acceptor-type. The first type is neutral when it contains an electron, the second type is negatively charge when it contains one.

There are four processes involved in the SRH recombination, which are described by the emission and capture of electron and holes. In figure 2.1 the trap occupation dynamic is shown.

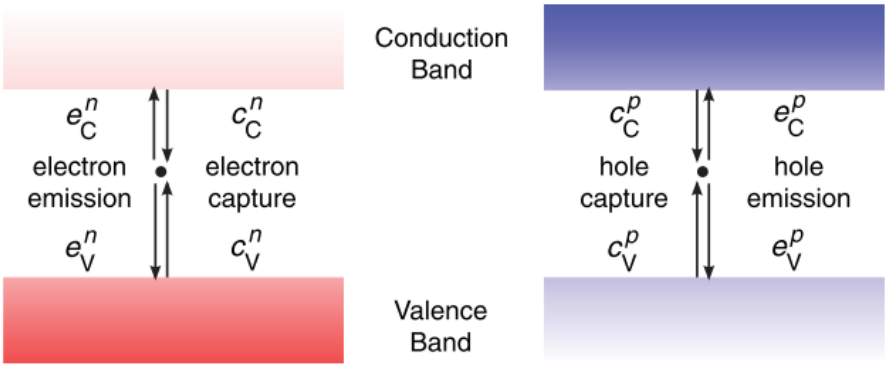

Figure 2.1: Trap occupation dynamics [2]

The occupation of traps, by electrons (f^n), can be expressed by the following equations:

$$\frac{\partial f^n}{\partial t} = \sum_i r_i^n \tag{2.13}$$

$$r_i^n = (1 - f^n)c_i^n - f^n e_i^n \tag{2.14}$$

where c_i^n is the electron capture rate and e_i^n is the electron emission rate. Note that the occupation is represented by a value between 0 and 1. For stationary processes the expression results in

$$f^n = \frac{\sum c_i^n}{\sum (c_i^n + e_i^n)} \tag{2.15}$$

Eventually with the combination of these processes, if the trap attracts both, an electron and hole, recombination will occur. This can be expressed with the equation below:

$$R_{net} = \frac{N_0 v_{th}^n v_{th}^p \sigma_n \sigma_p (np - n_{i,eff}^2)}{v_{th}^n \sigma_n (n + n_1/g_n) + v_{th}^p \sigma_p (p + p_1/g_p)} \tag{2.16}$$

with

$$n_1 = n_{i,eff} \cdot exp\Big(\frac{E_{trap}}{kT}\Big) \qquad p_1 = n_{i,eff} \cdot exp\Big(\frac{-E_{trap}}{kT}\Big) \tag{2.17}$$

where v_{th} is the thermal velocity of the charge carriers, σ is the capture cross section and g is the degeneracy factor.

This expression is only valid when the trap distribution is known. For crystalline silicon, however, the trap distribution is not provided. Therefore, the average lifetime of charge carriers is used,

assuming a single trap energy level. The SRH recombination rate can be expressed by the following expression:

$$R_{SRH} = \frac{(np - n_i^2)}{\tau_n^{SRH}(p + p_1) + \tau_p^{SRH}(n + n_1)} \tag{2.18}$$

where τ_n^{SRH} and τ_p^{SRH} are the SRH average lifetimes for electrons and holes respectively, and E_{trap} is the energy of the trap, usually assumed to be at the midgap.

SRH recombination not only takes place in the bulk of the material, but also at the surface, where the concentration of defects is usually higher. This can be expressed with the following equation:

$$R_{SRH}^{SURF} = \frac{SRV_n SRV_p(np - n_{i,eff}^2)}{SRV_n(p + p_1) + SRV_p(n + n_1)} \tag{2.19}$$

where SRV_n and SRV_p denote the surface recombination velocities of electrons and holes respectively.

Each type of recombination can be represented by an average lifetime of electrons and holes. Combining them all in parallel, an effective electron and hole lifetime (τ_{eff}) can be defined.

2.1.4. The pn junction in solar cells

As seen in the previous sections, in order for the free charge carriers to move, a concentration difference of charge carriers or an electric field is crucial.

This can be achieved by creating a junction of two or more materials with different work functions, such as the same semiconductor with different doping (homojunction), two types of semiconductors (heterojunction), or a metal and a semiconductor (MS junction).

As a p-type and n-type material are brought together, the electrons diffuse into the p-region and the holes into the n-region until they reach an equilibrium. Thus, positively and negatively ionized dopant atoms are left, forming the so-called space charge region. This directly results in the formation of an electric field, forcing the charges to move in opposite directions. When no external voltage is applied, the pn junction is under equilibrium. The induced electrostatic potential in equilibrium is called built-in voltage (V_{bi}).

Under illumination, excess charge carriers will be generated in the junction through the photoelectric principle. Applying this concept to a solar cell, as the excess charge carriers are generated, the goal is to collect them before they recombine. Due to the difference in electrostatic potential, the charge carriers can be separated and transported to the contact before the recombination takes place. For homojunctions, drift and diffusion causes the charge carrier transport. For heterojunctions, however, the transport mechanisms differ.

2.1.5. Transport in heterojunctions

In this section, the particularities of heterojunctions are explored. In this junction type, the bandgap of both materials are different. This results in a discontinuous energy band, and an extra energy barrier which the charge carriers must overcome. The relative alignment of the energy bands is called band offset. As shown in equation 2.20, the sum of the conduction band offset and the valence band offset needs to be equal to the bandgap difference between both materials (ΔE_G). The conduction

band offset (ΔE_C) is determined by the electron affinity difference of both materials (χ_1 and χ_2) as shown in equation 2.21. Finally, the valence band offset (ΔE_V) can be calculated as presented in equation 2.22.

$$\Delta E_G = \Delta E_C + \Delta E_V \tag{2.20}$$

$$\Delta E_C = \chi_1 - \chi_2 \tag{2.21}$$

$$\Delta E_V = \Delta E_G - \Delta E_C \tag{2.22}$$

An example of a heterojunction is shown in figure 2.2. The typical p- and n-contact stack of a Silicon heterojunction (SHJ) is shown, and two heterointerfaces, cSi-aSi and cSi-TCO, can be observed. The SHJ structure will be discussed in more depth in section 2.2. First, however, several physical phenomena need to be introduced.

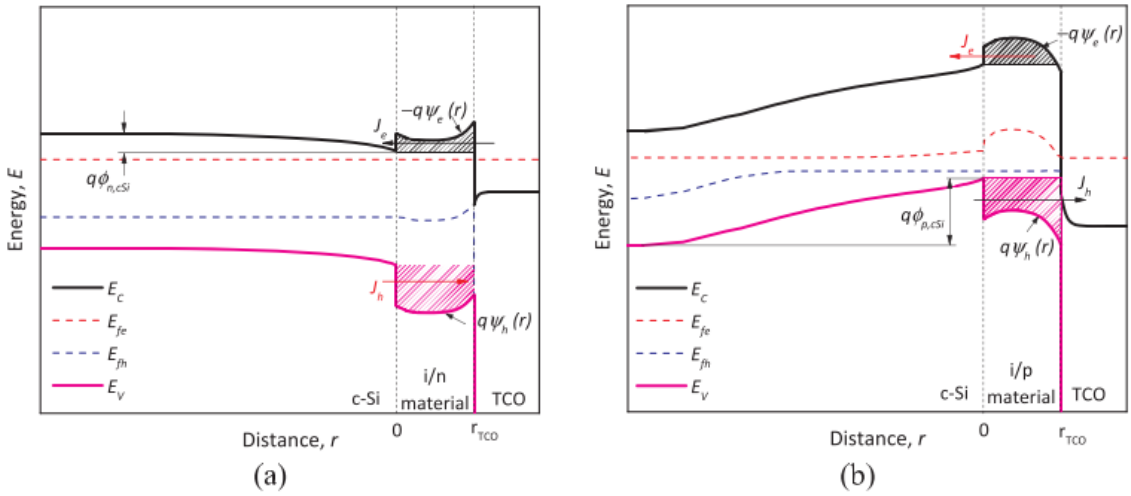

Figure 2.2: Band diagrams under illumination of a) n-contact and b) p-contact of a Silicon heterojunction. n-type c-Si, a-Si and TCO [3]

There are several mechanisms through which the charge carriers overcome the energy barrier between materials. The main transport mechanisms are thermionic emission and tunneling.

Thermionic emission

Thermionic emission is the process through which charge carriers travel over a potential barrier given a sufficient amount of thermal energy. In [16] the numerical modelling of thermionic emission in heterojunctions was discussed. The current due to thermionic emission can be expressed with the following equation:

$$J = A^* T^2 exp\Big(-\frac{q\phi_0}{kT}\Big) \tag{2.23}$$

where ϕ_0 is the barrier height, and T is the temperature. The *Richardson constant for thermionic emission* (A^*) is derived in [17]

$$A^* \equiv \frac{4\pi q m_n^* k^2}{h^3} \tag{2.24}$$

Tunneling

Tunneling is a quantum phenomenon in which the charge carrier has a finite probability of penetrating the energy barrier and appearing in the following region [17]. Tunneling current depends on a wide range of non-local variables, since the probability of tunneling highly depends on the transparency of the energy barrier. In the figure above, we distinguish two types of tunneling processes. In figure 2.2a, the electron travels from the conduction band of the cSi to the conduction band of the TCO. This phenomenon is called **direct tunneling**. In figure 2.2b, the hole tunnels from the valence band of the cSi until it recombines with an electron from the TCO conduction band, thus, generating a hole in the TCO. This process is called **band-to-band tunneling**.

In [18], the tunneling current (J_{Tun}) is described as a local generation current (G_{Tun}). The generation and the tunneling current are related by the following expression:

$$G_{Tun}(r) = \frac{dJ_{Tun}}{d\varepsilon} \cdot \vec{E} \tag{2.25}$$

where r is the distance, ε is the energy level, and $\vec{E}$ is the electric field. The tunneling electron generation rate used for the band diagram in 2.2, as derived in [18], is shown in 2.26. The tunneling hole generation rate is shown in 2.27.

$$G_{Tun,e}(r) = \frac{A^*T}{k}\vec{E} \cdot \Gamma_e(r) ln\left[\frac{1 + exp[-(E_{e,cSi} - E_{fe,cSi})/kT]}{1 + expo[-(E_{e,TCO} - E_{fe,TCO})/kT]}\right] \tag{2.26}$$

$$G_{Tun,e}(r) = \frac{A^*T}{k}\vec{E} \cdot \Gamma_h(r) ln\left[\frac{1 + exp[-(E_{fh,cSi} - E_{h,cSi})/kT]}{1 + exp[-(E_{e,TCO} - E_{fe,TCO})/kT]}\right] \tag{2.27}$$

where Γ is the tunneling probability, k is the Boltzmann constant, E_e and E_h are the electrostatic potentials of the charge carriers at the energy bands, and E_{fe} and E_{fh} represent the Quasi Fermi levels of electrons and holes respectively. It can observed from the equations that the tunneling generation current is proportional to the tunneling probability. The ratio inside the logarithm compares the filled energy states at the cSi/aSi interface with the filled energy states at the aSi/TCO interface. Hence, a higher density of filled states at the cSi/aSi interface, and a lower density of filled states at the aSi/TCO interface, results in a higher tunneling generation current. To calculate the tunneling probability, [18] uses the Wentzel-Kramers-Brillouin (WKB) approximation, which results in the following expressions for electrons (2.28) and holes 2.29).

$$\Gamma_e(r) = exp\left[-\frac{2}{\hbar}\int_0^r \sqrt{2m_e(E_{fe,TCO} - E_{C,cSi} - q\psi_e(r))}dr\right] \tag{2.28}$$

$$\Gamma_h(r) = exp\left[-\frac{2}{\hbar}\int_0^r \sqrt{2m_h(q\psi_h(r) - (E_{V,cSi} - E_{fe,TCO}))}dr\right] \tag{2.29}$$

where $\hbar$ is the reduced Planck constant, m_e and m_h are the tunneling masses for electrons and holes respectively, and ψ represents the electrostatic potential profile. From the equations we can

see that the tunneling probability decreases with the increase of the energy barrier. In figure 2.2, the area of the barriers is shown. As suggested by [19] and [20], direct tunneling and band-to-band tunneling (BTBT) are the dominant charge carrier transport mechanisms if the band mismatch is small. As the band mismatch increases, however, it is suggested that another mechanism dominates the transport, namely, **trap assisted tunneling (TAT)**.

Trap assisted tunneling

Tunneling and trap assisted tunneling can have a significant impact on the charge transport, not only for photovoltaic applications, but also for other microelectronic components. Therefore, many have concentrated their efforts in trying to solve this phenomenon analytically. Numerous models are available, however, most of them consider dielectric barriers which have different properties than aSi. With varying degrees of detail, [21], [22], [23], [24], and [25] all agree that there are several crucial parameters to take into consideration, namely:

- Energy barrier that needs to be overcome by the charge carrier
- Trap occupancy dynamics
- Trap density and trap distribution

Equation 2.30 shows the net recombination rate of the non-local tunneling model. An extensive explanation of the model can be found in [2]. The purpose of displaying the equation is to show the complexity of the numerical calculations and the considerable number of variables involved.

$$\begin{aligned} R_{net,n}^{TAT} =& C_n \int_0^1 \frac{\Gamma_C(x, E_C(0))}{\tau_n(x)} \frac{T(0)+T(x)}{2\sqrt{T(0)T(x)}} [exp\left[\frac{E_{F,n}(0)-E_C(0)}{kT(0)}\right] f^p(x) - \\ & - exp\left[\frac{E_T(x)-E_C(0)}{kT(x)}\right] f^n(x)]dx \end{aligned} \tag{2.30}$$

$$\Gamma_C(x,\varepsilon) = W_C(x,\varepsilon) exp\left(-2\int_0^x \kappa_C(x,\varepsilon)dr\right) \tag{2.31}$$

where τ_n is the electron lifetime, f^n is the electron occupation probability at the defect level, and f^p is the hole occupation probability at the defect level.

As mentioned in subsection 2.1.3, the defects, or so-called traps, in semiconductors can act as a discrete energy level in the forbidden bandgap. These intermediate energy levels may not only contribute to SRH recombination, but also help the charge carriers pass through an energy barrier. Accordingly, trap assisted tunneling combines the theory of emission and capture of charge carriers with tunneling.

In figure 2.3, the different types of tunneling are shown. Direct and band-to-band tunneling were already mentioned in the last section. In this section, elastic and inelastic trap assisted tunneling are focused on.

The main difference between these two phenomena, is that in inelastic TAT, the charge carrier is assisted by a phonon in order to reach the trap energy level. This translates into the emission of a phonon into the lattice, which ultimately converts into thermal energy. In the elastic process, however, the charge carrier maintains the same level of energy.

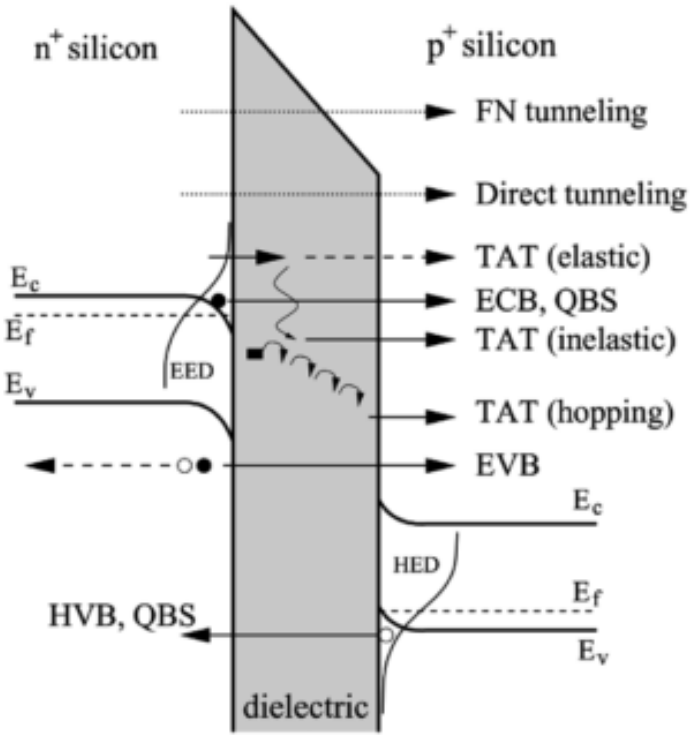

Figure 2.3: Tunneling processes in a MOS structure [4]

In the case of dielectrics, it has been suggested in several studies that the inelastic process is mainly responsible for the transport [26]. As suggested by [19] and [20], since amorphous silicon behaves as a direct bandgap material, elastic TAT can be considered as the main transport mechanism. Consequently, phonon emission is not considered in this study's TAT model.

In the following section, a more in-depth description of silicon heterojunctions will be provided. Characteristics of the materials in use, such as amorphous silicon and tunnel conductive oxides (TCO), are also presented.

2.2. Silicon heterojunction: Concept and materials

The principle of heterojunction solar cells involves the presence of at least two different materials. The use of heterojunctions is especially interesting for selective contacts. This can be applied to several technologies, however, in this study, focus is placed on Silicon heterojunctions. In addition, for the passivating contact, amorphous silicon is used. It is worth mentioning that recent studies performed by [27] and [13] have shown that new materials can produce such passivating effects with cSi.

2.2.1. Silicon heterojunctions in solar cells

Unlike other types of contact such as diffused homojunctions, heterojunctions offer excellent passivation qualities and selectivity. The basis behind achieving such characteristics lies in the selection of materials with an adequate work function, such as aSi, as to allow a sufficient electrostatic po-

tential to be induced in the cSi bulk. In addition to p- and n-doped aSi, the passivation quality also occurs due to the inclusion of a thin intrinsic hydrogenated aSi layer. This layer enhances the chemical passivation, and significantly reduces the recombination at the heterointerface [5]. An important parameter to take into consideration is the doping concentration in the aSi. Higher doping concentration reduces the activation energy, thus increasing the selectivity of the contact. Moreover, there is an inversion layer at the cSi/aSi interface which translates into field-effect passivation. SHJ features result in values of V_{oc}, ranging from 730mV to 760mV ([28],[29], [30], [31]), which is a significant increase compared to that of conventional homojunction technology.

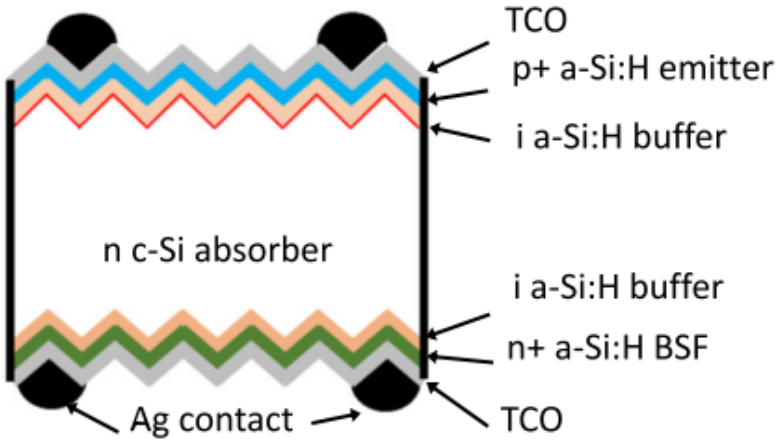

Figure 2.4: Typical scheme for SHJ [5]

The typical scheme for SHJ is shown in figure 2.4. The absorber is made from n-type cSi. N-type bulk presents a series of advantages, as it inherently has better electronic bulk quality. Typically, higher efficiencies have been reported for n-type bulk SHJ, due to the better passivation of n-type cSi with aSi [32].

Regardless of the numerous advantages that this type of configuration presents, there are still challenges that SHJ has to face. Due to the poor conductivity of the aSi, there needs to be a TCO layer in both the front and back contact to enhance the lateral transport of the charge carriers. Besides this, aSi has an impact in the optic performance of the cell due to the parasitic light absorption, accounting for rather significant losses in short circuit current (J_{sc}). In some cases, up to $2.1 mA{\cdot}cm^{-2}$ [33] is lost. Moreover, the aSi layer deposition can cause a high defect density at the heterointerface, increasing recombination, and therefore decreasing V_{oc}. Additionally, a large band offset at the valence band has shown to affect the carrier collection, and thus, decrease the fill factor (FF) [5].

In this work, the focus will be on the contact stacks, composed of intrinsic and doped aSi together with the TCO. In the following sections, the properties of these materials will be explored in order to understand how to integrate them optimally.

2.2.2. Hydrogenated amorphous silicon

Amorphous silicon is a material used in multiple applications for microelectronics and the photovoltaic industry. For the latter, it is of particular interest in thin film solar cells and as mentioned

in the last section, for passivation purposes in SHJ. One of the main advantages of aSi is that it can be deposited over large areas at a relatively low temperature, making the process less costly. For electronic applications, an alloy of aSi and hydrogen is used, or so called, hydrogenated amorphous silicon (a-Si:H). Note that from here on, hydrogenated amorphous silicon is referred to as simply amorphous silicon or aSi.

For SHJ modelling it is necessary to understand the properties of the materials involved in it. To that end, the general properties such as structure and density of states are presented in the following section. Besides this, the models used to describe the physical behaviour of aSi are presented.

Atomic structure

In order to better understand the atomic structure of aSi, it is worth mentioning briefly the structure of cSi. In crystalline silicon structure, silicon atoms have four covalent bonds, all of the same length and forming the same angle. This leads to a repetitive structure in space. Such a regular atomic structure is qualified as *long range order*. Unlike cSi, aSi structure does not present a long range order. Nevertheless, it has a similar local atomic configuration, or so-called, *short-range order*. This results in a structure called *continuous random network* (CRN). [6]

The concept of defects for cSi and aSi also differ. While in cSi a defect is considered as an atom out of place, in aSi, the concept is no longer applicable since there is not a long range order. For a continuous random structure, a defect is considered a coordination defect, meaning that the atom has either more or less than four bonds. Often, an atom has an unpaired electron, or so called *dangling bond*, also present in unpassivated cSi surfaces. Dangling bonds are not regularly distributed in the CRN, they can group in divacancies, multivacancies and nanosized voids [34]. The incorporation of hydrogen in aSi has the purpose of passivating the dangling bonds, hence reducing the dangling bond density. The hydrogen content varies between 5% and 15%, reducing the defect density down to $10^{16} cm^{-3}$ [35]. This can be observed in figure 2.5 that shows a scheme of the atomic structure of both, cSi and hydrogenated aSi.

Density of energy states

Due to the different atomic structure, the distribution of allowed energy states of aSi differs from that of cSi. The long range order of cSi atoms leads to determined ranges of energy in which the electrons are allowed to be, as well as the ones that are forbidden (energy band gap). Conversely, aSi does not have a well defined band gap. As we can see in figure 2.6, the energy states of the valence and conduction bands spread further. This extension is known as tail states. It was observed that charge carriers are frequently trapped in localized band tails, reducing the mobility. Therefore, band edge was defined as *mobility edge* [36]. The definition of conduction band and valence band is given as the energy level that separates the extended states and the localized states of the aSi. Notice that the mobility edge acquires a value of around 1.7 eV, greater than that of cSi at typically 1.12 eV. In addition, centered in the mobility edge, the defect states or so called dangling bonds, make a contribution to the density of state (DOS). The defect states can usually be approximated by two gaussians distributions. In the following sections, the DOS models of aSi are presented in more detail.

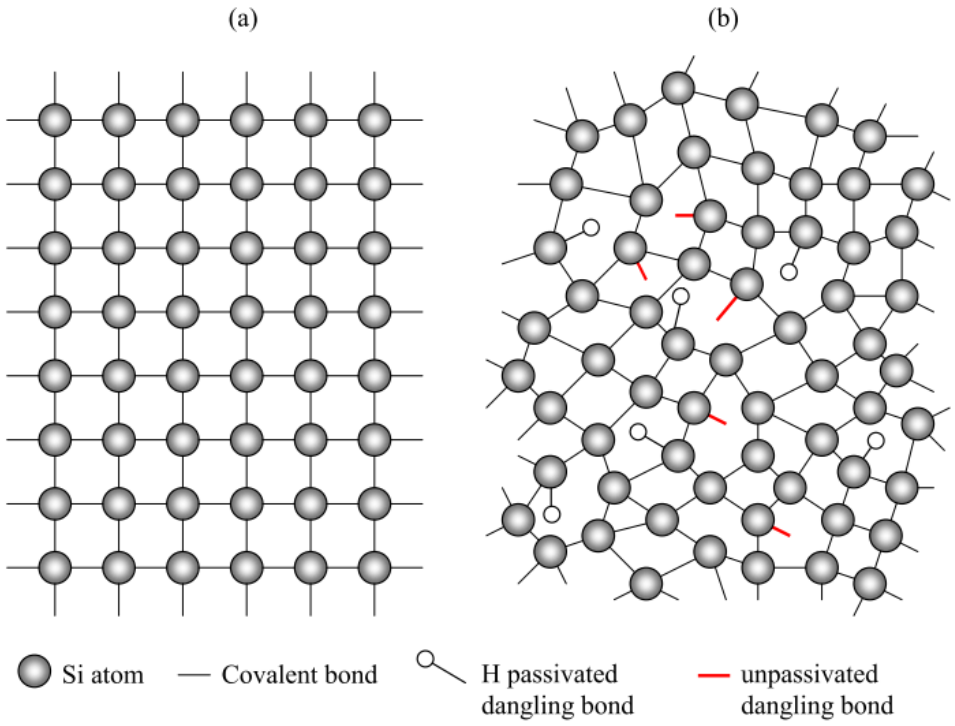

Figure 2.5: Atomic structure of a) crystalline silicon and b) hydrogenated amorphous silicon [6]

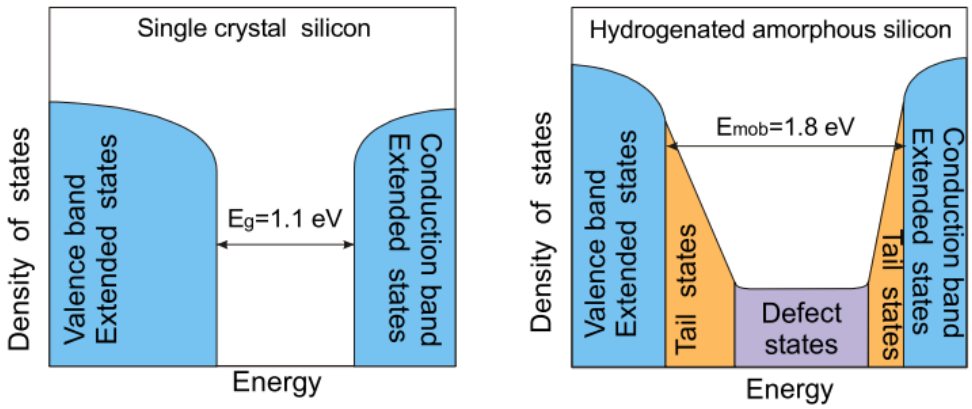

Figure 2.6: Density of states of cSi on the left hand side and aSi on the right hand side [6]

Optical properties

Amorphous silicon is characterized by its high absorption coefficient. Unlike cSi, aSi exhibits the properties of a direct band gap material due to its atomic structure. In figure 2.7 it can be observed that aSi absorbs around 100 times more light in the visible spectrum than cSi. Morever, the absoption coefficient can be modified by alloying the aSi with other materials such as Germanium.

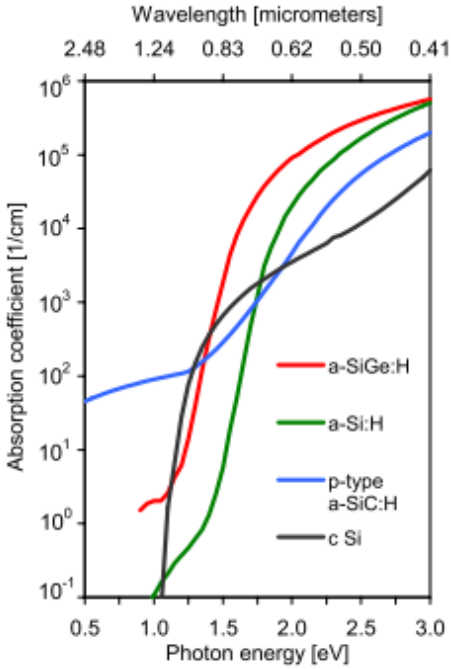

Figure 2.7: Absorption coefficient of several aSi alloys (TU Delft) and cSi [6]

The optical properties of aSi can play as an advantage in some cases, like in thin film applications, where the absorber is made from this material. However, when aSi is used with passivation purposes, it plays a major role in the non-desirable parasitic absorption.

Modelling of aSi

Modelling of aSi is particularly complex because of the aforementioned differences with cSi. The DOS has to be characterized in several regions: extended states found above the mobility edge of CB, below the mobility edge of VB, and localized states in between the mobility edges [7]. In addition, the charge carrier transport takes place not only in the extended states, but also in the mobility band helped by the defect states.

There are several models for aSi DOS. Here, **standard model** [35] and **Defect pool model** [37] are to be discussed. The standard model of density of states, describes the band tails as an exponential distribution for both conduction and valence band tails. The analytic expressions for the conduction band tail (CBT) and valence band tail (VBT) are shown in equations 2.32 and 2.33 respectively.

$$N_{CBT}(E) = N_{C0} exp\left[-\left(\frac{E - E_C^{tail}}{E_{C0}^{tail}} \right) \right] \tag{2.32}$$

$$N_{VBT}(E) = N_{V0} exp\left[-\left(\frac{E - E_V^{tail}}{E_{V0}^{tail}} \right) \right] \tag{2.33}$$

where E_{C0}^{tail} and E_{V0}^{tail} represent the characteristic energy of CBT and VBT respectively, and similarly, N_{C0} and N_{V0} are the conduction and valence band tail density of states.

To model the dangling bond states or defect states, two Gaussian distributions are chosen. There are 3 groups of dangling bond states: neutral, positive and negative. A way of representing the three groups is with the partial superposition of 2 Gaussian distributions, namely, one acceptor-like ($DB^{0/-}$) state and one donor-like state ($DB^{+/0}$). The distributions are centered in the so-called transition levels $E_{DB}^{0/-}$ and $E_{DB}^{+/0}$ respectively. In addition, the transition energy levels are separated by a correlation energy, U. The correlation energy is the energy needed for an a second electron to occupy a neutral dangling bond. The Gaussian distributions can be described mathematically as follows:

$$N_{DB^{+/0}}(E) = \frac{N_{DB}^{tot}}{\sigma_{db}\sqrt{2\pi}} exp\left[- \frac{(E - E_{DB}^{+/0})^2}{2\sigma_{db}^2} \right] \tag{2.34}$$

$$N_{DB^{0/-}}(E) = \frac{N_{DB}^{tot}}{\sigma_{db}\sqrt{2\pi}} exp\left[- \frac{(E - E_{DB}^{0/-})^2}{2\sigma_{db}^2} \right] \tag{2.35}$$

where N_{DB}^{tot} is the density of dangling bonds, and σ_{db} is the standard deviation of the Gaussian distribution.

An illustration of an example of density of states distribution can be found in figure 2.8.

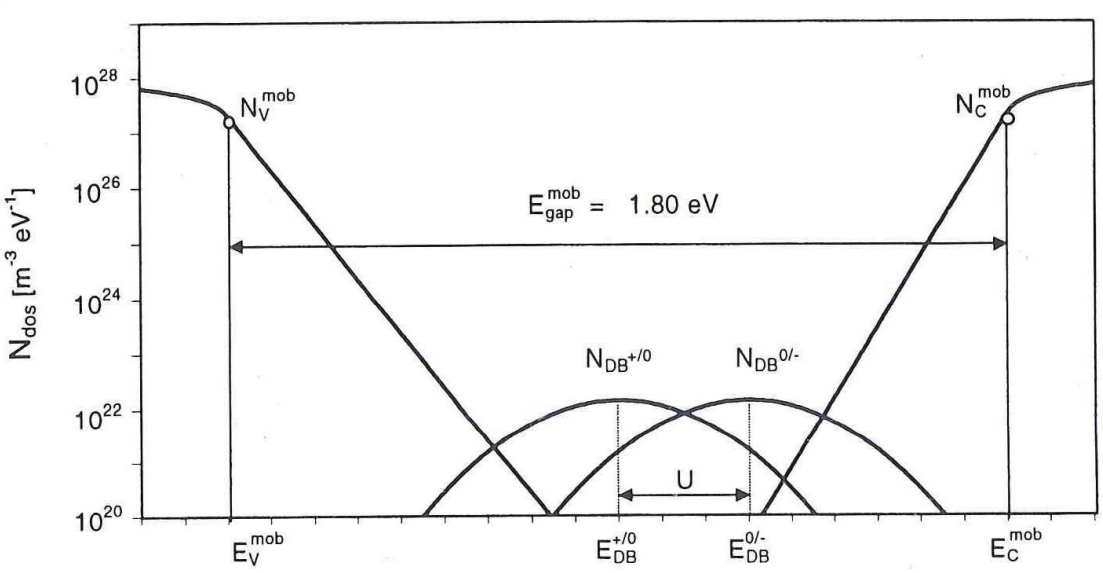

Figure 2.8: Standard model of density of states in aSi [7]

The defect pool model only refers to the defect states. It suggests that there is a strong relation between the Fermi level and the distribution of the dangling bonds. As illustrated in figure 2.9, intrinsic aSi shows DB centered in the mobility band, while it shifts closer to the bands for doped aSi.

2.2.3. Transparent conductive oxide (TCO)

The TCO has a very important function in the cell. When placed at the front of the cell, for front contacted cells, it acts as an electric contact. The TCO is increasingly being used for other purposes,

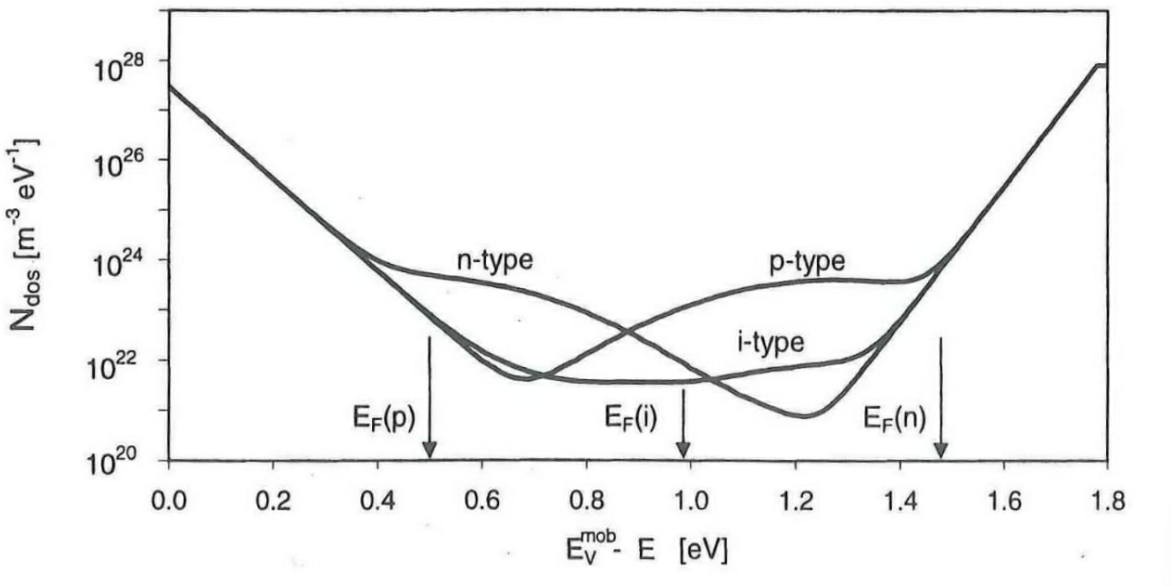

Figure 2.9: Dangling bond distribution according to pool defect model for different Fermi levels [7]

such as diffusion barriers and control contact work function [38]. More specifically for heterojunctions, it becomes useful when using aSi for passivating contacts. Since the aSi is not a very good conductor, the TCO helps the charge carriers to reach the contacts. To that end, it is fundamental to choose a material with the appropriate work function and conductivity.

The importance of the band alignment in SHJ, can be clearly seen in figure 2.10. As seen in the figure, the TCO work function plays a major role in the band alignment, and therefore in the transport of charge carriers. Through simulations, [3] has suggested that the transport at the p-contact improves for higher values of TCO work function.

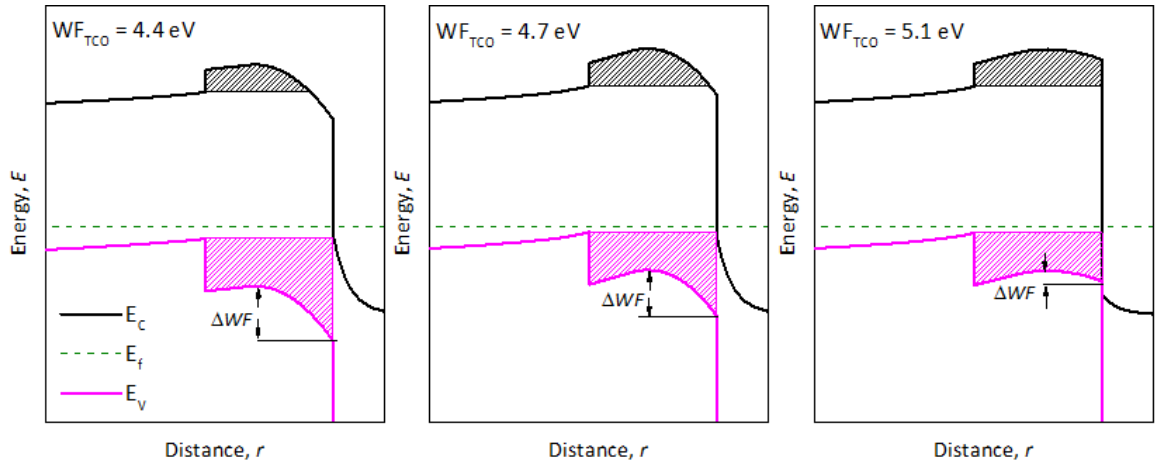

Figure 2.10: Band diagrams in equilibrium of p-contact stack for different work functions of TCO and same activation energy. From left to right: n-type cSi, i-aSi, p-aSi and TCO [3]

In figure 2.11 a comparison of typical TCO used in the PV industry can be seen, namely, indium tin oxide (ITO), aluminum-doped zinc-oxide (AZO) and antimony-doped tin oxide (ATO).

Based on the diagram, the interesting TCO for SHJ would be in the top right corner, having high

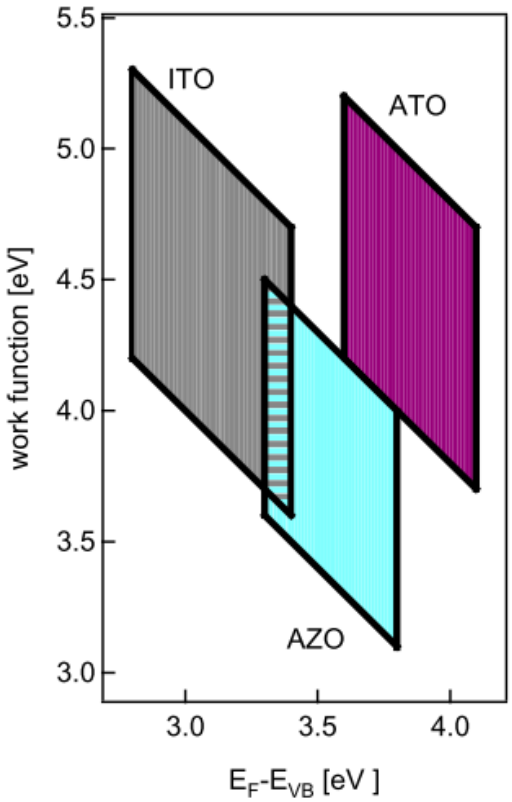

Figure 2.11: Work function and Fermi level position of ITO, ATO and AZO [8]

work function and high conductivity. The conductivity (σ) of the TCO is described by $\sigma = \mu \cdot N_{TCO}$, being μ the mobility and N_{TCO} the carrier density of the TCO. Accordingly, the carrier density is directly related to X axis of figrue 2.11, the larger the difference between the Fermi level (E_F) and the valence band energy (E_V) is, the larger the carrier density and hence the conductivity.

Concerning the modelling of TCO, it is normally modeled as a metal with a specific work function. Nevertheless, this assumption may underestimate transport mechanisms at heterointerfaces [39].

2.3. IBC-SHJ

Once the main advantages of silicon heterojunctions are understood, a particular configuration can be focussed on, namely, interdigitated back contact (IBC). IBC configuration has repeatedly demonstrated record results due to the absence of shading losses [40], [41], [13]. The combination of IBC and SHJ presents numerous advantages that are explained in this section.

2.3.1. Cell architecture

IBC architecture's main advantage is that it avoids front shading losses, thus achieving a higher J_{SC} [42]. Conversely, the deposition of thin hydrogenated amorphous silicon at the front and rear of the cell provides excellent chemical passivation of the cSi absorber [5], thus achieving a higher V_{oc}. Thanks to the combination of both features, IBC-SHJ yielded world record efficiency for single junction cSi cells at 26.7% [14]. This section is dedicated to explaining the structure an IBC-SHJ cell

in more detail. A typical IBC-SHJ geometry can be found in figure 2.12. From the top to bottom of the cell:

- Anti-reflecting coating (ARC)
- Front surface field (FSF)
- n-type c-Si bulk
- intrinsic hydrogenated a-Si passivating layer
- interdigitated structure of n and p-doped hydrogenated a-Si that act as back surface field (BSF) and emitter respectively.
- Tunnel conductive oxide (TCO)
- Metal

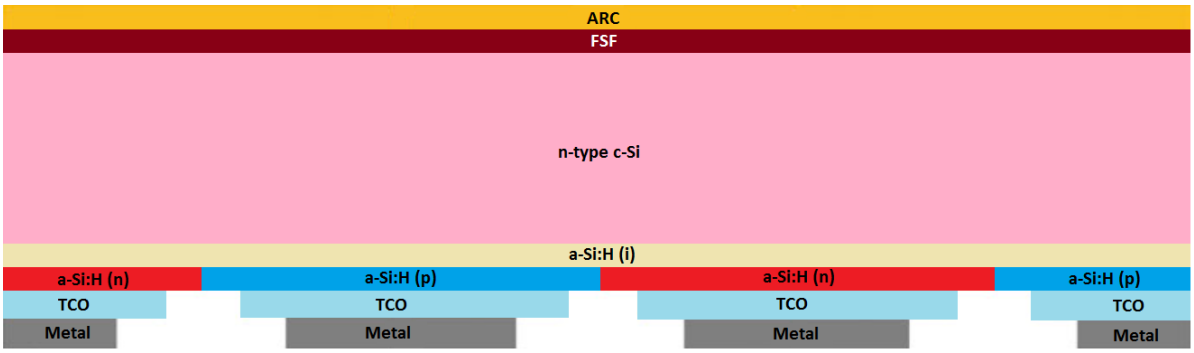

Figure 2.12: Sketch of a complete structure of an IBC-SHJ cell

It can seen that the contacts are indeed at the back of the cell configured in a periodic structure. This leaves the front free from shading losses due to the metallic grid. It is important, nevertheless, to have good light management at the front of the cell to reduce reflection. This is achieved by an anti-reflective coating for which many designs and materials have been studied [43]. In addition, good passivation has to be achieved in order to reduce front surface recombination, this can be done chemically - by depositing an intrinsic a-Si film - or by field passivation - with a highly doped a-Si layer. The bulk of the cell can be n-type or p-type c-Si indistinctly. It is worth noticing, however, that the bulk resistivity is very sensitive to dopant concentration [44]. Studies have proven that V_{OC} is increased by adding a thin intrinsic a-Si layer between the bulk and the doped a-Si layer. The performance of the cell, however, is highly sensitive to the thickness of it [45].

The configuration also presents certain disadvantages compared to conventional front contact architecture. Since both electrons and holes are collected on the back, a current crowding effect can be observed, thus increasing resistance [12]. In addition, the characteristic disadvantages of SHJ such as parasitic aSi absorption, and the need of TCO on the back to improve the conductivity, also apply for IBC SHJ.

2.3.2. Modelling of IBC-SHJ

Due to the interdigitated IBC configuration, one dimensional models, unlike for conventional architectures, are not sufficient to simulate the behaviour of such a cell. Consequently, the reference

software for cSi/aSi heterojunctions, AFORS-HET, cannot be used since only 1D models are available [46]. A set of softwares are available for two and three dimensional semiconductor device simulation, such as ATLAS [47], CoBoGui [48], Quokka [49], SARAH [50] (made specially for IBC modelling).

The numerical simulation tool selected for this work is Sentaurus Device, by Sypnosis [2]. It is an advance multidimensional software, which is able to simulate the optical, electrical and thermal behaviour of a wide range of silicon based semiconductor devices, as well as compound semiconductors. It was developed during the early 90's and it has significantly contributed to the development and innovation of semiconductor devices [51]. In addition, it offers a broad selection of state of the art semiconductor physics models. It is widely used and trusted by the semiconductor and PV industries due to having over 30 years of trajectory and user experience.

To summarize, the modelling of IBC-SHJ will be carried out in Sentaurus in a 2D domain. Accordingly, the use of the physical models described throughout this chapter is required. Continuity, generation, recombination and transport of charge carriers are solved by means of the models presented in section 2.1. Besides this, the characteristics of materials present in the cell, such as aSi and TCO, are modelled using the equations found in section 2.2.2 and 2.2.3.

In the next chapter, the semiconductor device simulation approach in Sentaurus will be described, focusing on the particularities of IBC-SHJ configuration.

3

Simulation Approach

In this chapter, the semiconductor device modelling approach is explained. Firstly, in section 3.1, the different modelling modules are introduced. Then, in the following sections, each module is addressed individually. The virtual device modelling is explained in section 3.2, and the optical and electrical models are described in sections 3.3 and 3.4 respectively. Finally, the limitation of the original model, by Procel et al. [52] will be introduced.

3.1. General semiconductor device modelling

The general approach for semiconductor device modelling is summarized in the figure below 3.1. Firstly, the virtual device is built by mimicking the geometry of the physical device, as well as other characteristics such as the doping profiles. As a result, the virtual device is defined by a mesh and a set of parameters that will be used as an input for the next process, the physical modelling.

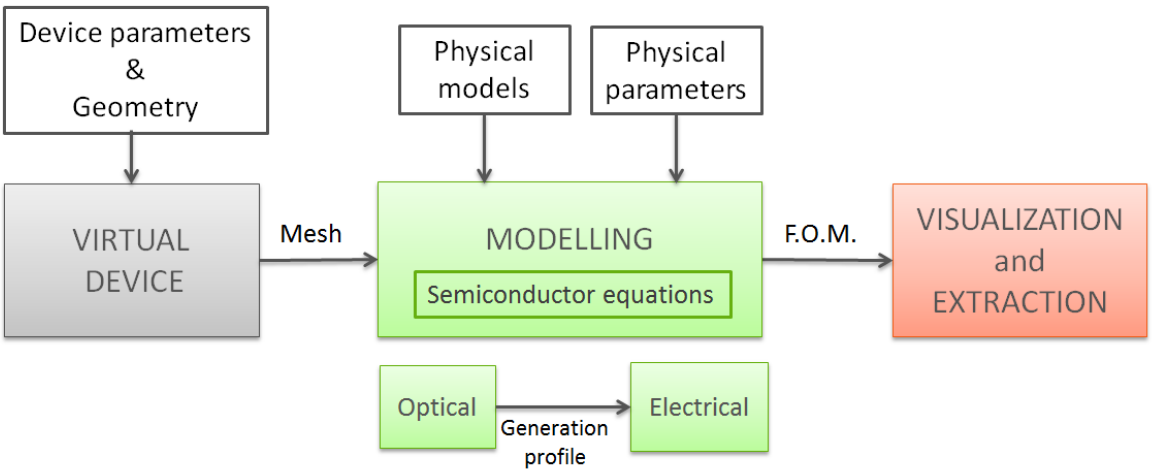

Figure 3.1: Simulation approach flowchart

In this module, the optical and the electrical behaviour of the device is modelled. For this purpose, the semiconductor equations - *based on the drift-diffusion model* - are solved for each point of the mesh. Coupled with those, a set of physical models are selected (table 3.2). In addition, the optical and electrical properties of the device are an input of this module.

Finally, after numerically solving the aforementioned equations, the figures of merit (FOM) are obtained. TCAD Sentaurus allows a detailed analysis of the device, providing information such as the energy band diagram, the tunneling current at a particular interface, recombination current, etc.

Throughout the next sections, the specific features of each module are outlined. Moreover, the selection and justification of the physical models used in this work are presented.

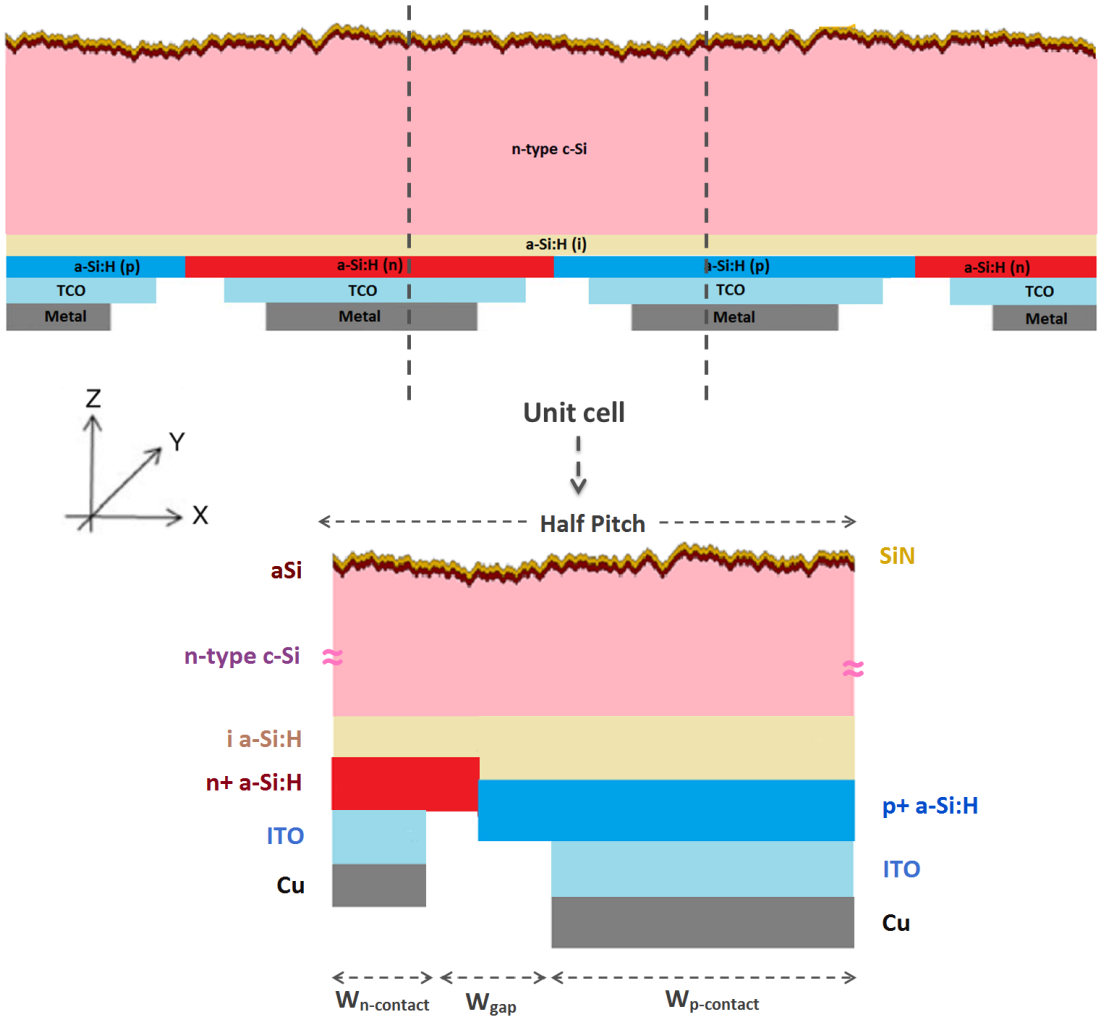

Figure 3.2: IBC-SHJ scheme and unit cell

3.2. Virtual device: cell modelling

Since IBC-SHJ presents a periodic structure, a unit cell, or so called *standard domain* (shown in figure 3.2), serves as a basis to simulate the physics of the whole device, whilst saving computational time. By doing so, it is assumed that the there is no charge exchange between symmetric elements. Moreover, as mentioned in section 2.3.2, IBC-SHJ cells can be modelled in 2 or 3 dimensions. Al-Shouq et

al. [53] reported that 3D simulations results were similar to the ones performed in 2D, with larger computational time. Thus, simulations of the unit cell in a two-dimensional domain are used in this work.

3.2.1. Mesh

Using the finite element approach in order to numerically solve the drift-diffusion model equations, it is necessary to discretize the domain with a mesh. The mesh is defined in accordance to the particular physics inside each region. Accordingly, mesh distance should be fine where the input or output parameters strongly depends on the distance. In particular, for PV devices, the regions where the mesh should exhibit a higher resolution are [51]:

- Near the front surface, since the short wavelength part of the solar spectrum is absorbed within few micrometers.
- Close to the metal contact at the rear, due to current crowding
- At interfaces, due to higher recombination rate and transport phenomena

Figure 3.4 shows an inset of the IBC-SHJ mesh in Sentaurus, describing that the mesh near the contacts displays higher resolution than in the bulk. To this end, as shown in figure 3.3, there are a set of parameters that are fixed to achieve the necessary mesh coverage and resolution.

Figure 3.3: Simplified scheme of mesh refinement parameters

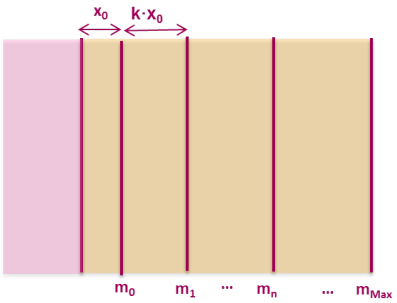

It is worth noticing that while setting the mesh parameters, a compromise between accuracy and computational time is made. Besides this, convergence is very sensitive to the mesh resolution. Accordingly, in this work, the mesh parameters for each particular region (x_0, k and Max) are selected following the aforementioned guidelines while guaranteeing convergence and valid numerical results.

3.2.2. Doping

In addition to the geometric characteristics, the materials and the doping of each particular region are defined. In this work, an evenly distributed doping density (**Constant doping profile**) is used to characterize every region.

When modelling silicon thin film alloys, the doping density is not provided, on the grounds that at a laboratory scale, it is only possible to measure the activation energy (E_a) of the deposited layer. This raises another challenge due to the fact that the activation energy not only depends on the doping concentration but also on the defect states, where charge can be trapped.

In this work, the doping density of the thin film layers is not solved analytically, but numerically. As the flowchart depicted in figure 3.5 shows, the doping density is tuned - *in an iterative process* - until reaching the activation energy of the physical layer, while the defect states are considered constant.

The doping density of crystalline materials such as cSi, however, are calculated by means of the

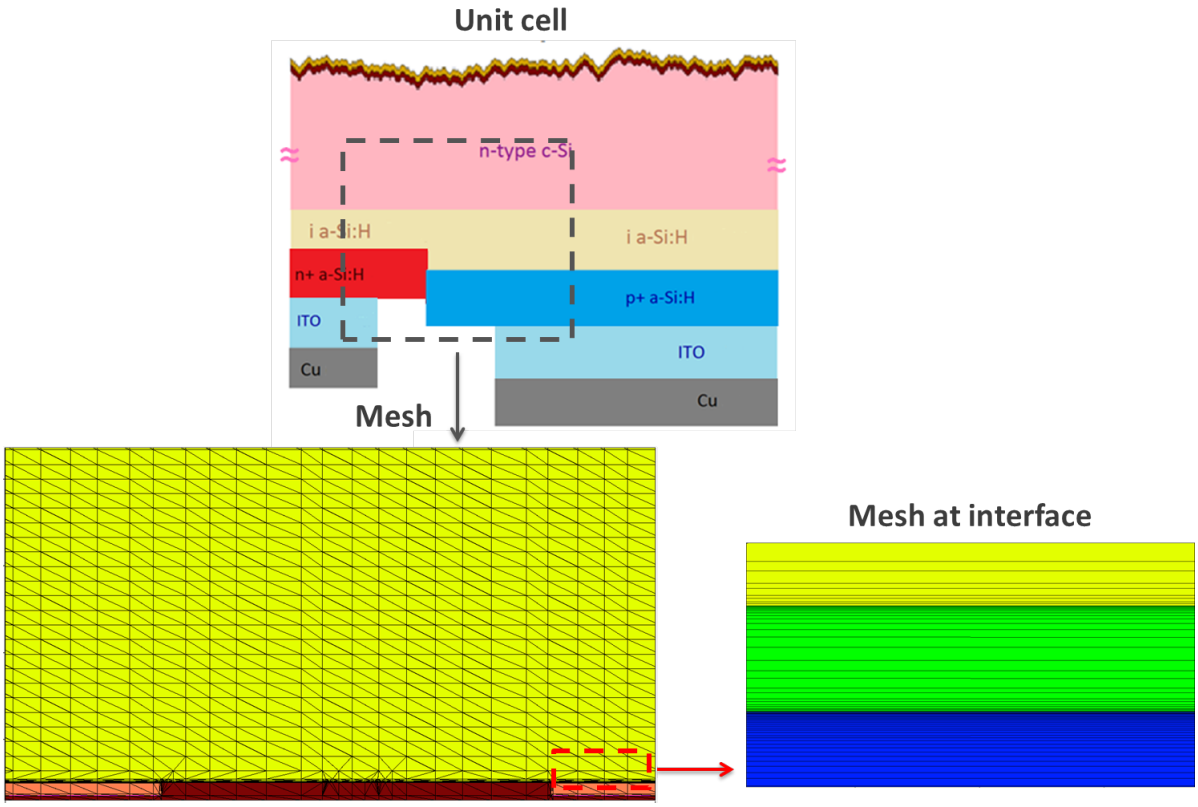

Figure 3.4: Inset IBC-SHJ mesh

experimentally measured bulk resistance. In this case, PV Lighthouse resistivity calculator [54] is used.

3.3. Optical modelling

The goal of the optical modelling is to obtain the optical generation profile of the cell. Sentaurus offers the possibility to input the optical generation profile from an external file or the possibility of calculating it by means of different methods. Since the scope of this thesis does not focus on optical modelling, only the methods that were used for this work are outlined, namely, *Monte Carlo tracing technique* [55][56] and *transfer matrix method (TMM)* [57].

3.3.1. Monte Carlo ray tracing technique

Monte Carlo ray tracing technique consists of tracing the rays that are reflected or transmitted at each layer by means of a probability. The aggregate of the path followed by numerous rays, gives information on the reflectance and transmittance of the different layers. This method is recommended given the rough surface on the front of the cell [2].

3.3.2. Transfer Matrix Method

The TMM, however, consists of the calculation of the wave propagation through a layered medium. This method solves the complex reflections by assuming that there is a continuity of the electric

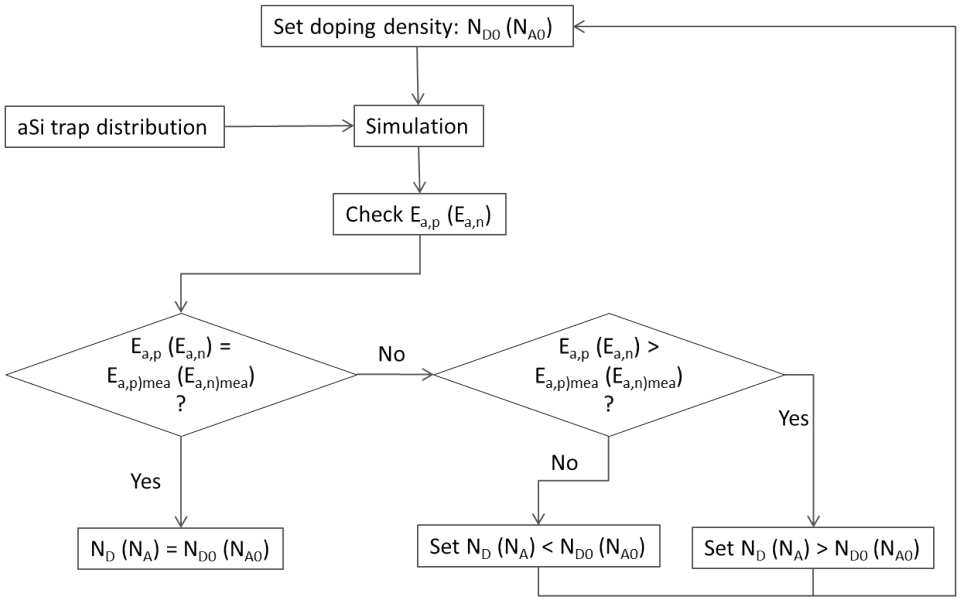

Figure 3.5: Flowchart to calculate doping density

field (Maxwell's equations). The layers can be represented by a matrix system, which ultimately is converted into reflection and transmission coefficients. It is important to set the boundary conditions in accordance to the domain simulated. Since we work with a symmetry element, it is necessary to specify that the vertical interfaces are fully reflectant.

It is worth noticing that while being an ideal simplification to solve such complex optic problems, the TMM also has its limitations. This method does not take into account a possible back reflection in the bulk, which leads to an underestimation of the long-wavelength photons scattering. Following the methods of Procel [52], in order to face this issue, a screen layer is placed over the illumination plane as illustrated in figure 3.6a. The screen layer is donated with a certain reflectance value, named R_2, which is considered a variable that needs calibration. The layer's purpose is to reflect the rear reflected rays that escape through the front, back to the cell with a certain probability (R_2).

Notice that the screen layer is only effective for the primary reflection and from a certain wavelength. Longer wavelengths are more likely to reach the rear of the cell, whereas short wavelengths are generally absorbed or reflected in the front layers. The distinction between short and long wavelength is highly dependant on the thickness of the simulated device. By means of simulation, the photons that are transmitted to the rear of the cell as a function of the wavelength are obtained, as seen in figure 3.6b. On this basis, the limit between short and long wavelength is set at 850 nm (table 3.1), which matches with the wavelength at which photons reach the rear of the cell.

Table 3.1: Short and long wavelength

Short wavelength	Long wavelength
$300nm < \lambda < 850nm$	$850nm < \lambda < 1200nm$

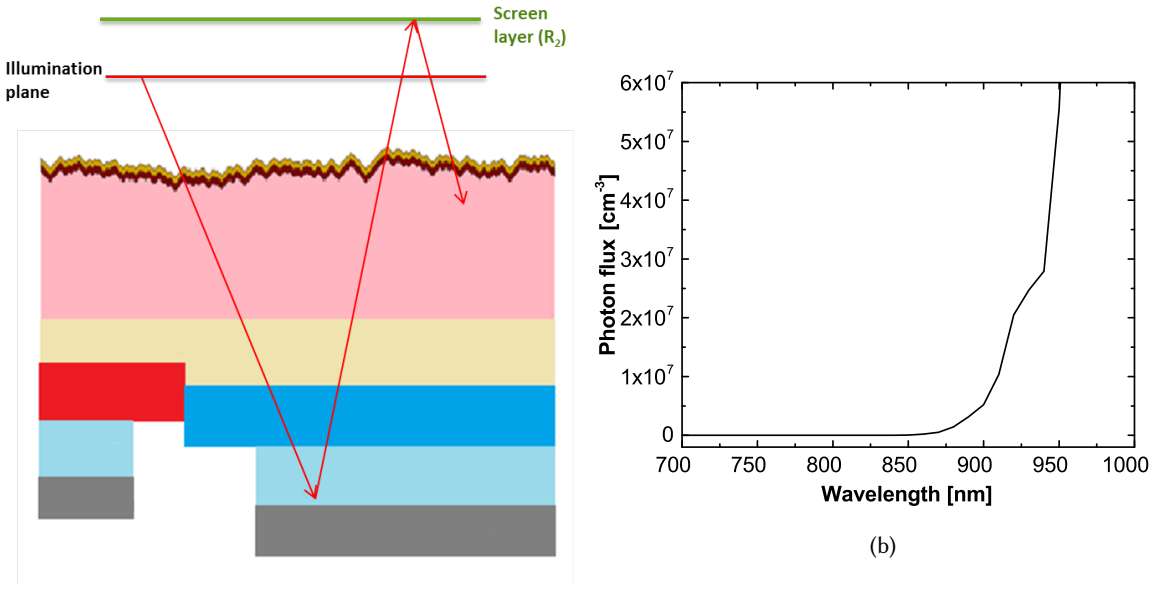

Figure 3.6: **a)**Screen layer scheme **b)**Photon flux transmitted to the rear of the IBC-SHJ cell. It is observed that at 850nm, the photons may be reflected out of the cell, hence the screen layer is enabled at that wavelength.

3.4. Electrical modelling

The objective of the electrical modelling is to describe the physics of the semiconductor device by means of numerical simulation. It is thus important to shed light not only on the physical models chosen to describe the IBC-SHJ but also on the numerical solving approach.

The drift-diffusion model is the basis to solve the physics of a semiconductor device, the basic equations that define the model are outlined in section 2.1. Accordingly, it is necessary to guide the solver by indicating the order in which the equations are tackled so as to have a numerically valid solution.

Firstly, the solution of the Poisson equation (2.2), serves as the initial boundary condition to solve the continuity equations of electrons (2.5) and holes (2.4). Initially, this is done under equilibrium - *no applied voltage and under no illumination* - and later it is solved for an increasing applied voltage. Each stage provides the initial conditions used for the next one. Ultimately, the behaviour of the device under dark conditions is obtained.

For simulating the device under illumination, however, the approach is a slightly different. Similar to the previous approach, equilibrium is the initial solution. Then, illumination is gradually increased - *under no applied voltage* - until 1Sun is reached. Once the solution under 1Sun is obtained, the voltage increases as previously described. Lastly, the results for the device under illumination are achieved.

A wide range of physical models which complement the drift-diffusion model are implemented in order to mimic the physical behaviour of the IBC-SHJ. In the following sections, the more relevant models for the scope of the thesis are addressed. All the physical models selected are summarized in table 3.2.

3.4.1. Generation and recombination

The optical generation profile is directly obtained from the optical modelling without further adjustments. Concerning the recombination, it is modelled following the physics described in section 2.1.3. Subsequently, the following categories can be distinguished:

- Intrinsic recombination: Auger and radiative
- Shockley Read Hall recombination

The model chosen for the intrinsic recombination by Ritcher et al. [15], combines both radiative and the auger recombination. For SRH recombination, however, the chosen model depends on whether the trap distribution in a specific region is provided or not. Specifically for IBC-SHJ, the defect distribution is not known in the following regions: 1)cSi bulk and 2)Front surface 3)cSi/n-aSi surface 4)cSi/p-aSi surface. Therefore, the equations 2.18 and 2.19 presented in section 2.1.3 are used to model the bulk and surfaces recombination respectively. Accordingly, the parameters that need to be set for each region are: 1)$\tau_{Bulk,SRH}$, 2)SRV_{front}, 3)SRV_n and 4)SRV_p. Additionally, the defect distribution in the deposited aSi layers is modelled, allowing to use the general model of SRH (eq. 2.16). The implementation of the aSi defects will be further explained in chapter 4.

Table 3.2: Summary of the physics model used for the electrical simulation

Device simulation	
Free carrier statistics	Fermi-Dirac [58]
Intrinsic carrier density	$9.65 \times 10^9 cm^{-3}$ Altermatt [59]
Intrinsic recombination: Auger and radiative	Ritcher [15]
Band gap narrowing	Schenk [60]
Free carrier mobility	Doping dependent mobility. Philips unified mobility model by Klaassen [61] High field saturation: Canali model [62]
Doping	Phosphorous and Boron constant profile
Tunneling	Non-local tunneling model [18]

3.4.2. Transport in heterojunctions

An introduction to heterojunctions was presented in section 2.1.5. In particular, in IBC-SHJ, the heterojunctions are formed between 1) the cSi bulk and the i-aSi layer and 2)the n-aSi(p-aSi) layers and the TCO.

Subsequently, the models for transport mechanisms in heterojunctions -*thermionic emission [63] and tunneling*- are implemented. Concerning tunneling, Sentaurus offers a wide range of models, from which the non-local tunneling model is selected given its reduced computational time [2]. The description of the model and the equations is presented in section 2.1.5. In addition to setting the tunneling parameters (m_e and m_h) - presented in equations 2.26 and 2.27 - the simulator requires the implementation of a **non-local mesh**. As illustrated in 3.7a, "the non-local mesh consist of non-local lines that that represent the tunneling paths for carriers" [2]. Here, the non-local mesh is

defined in the interface between cSi and aSi (figure 3.7b), and it extents a distance *length* into the aSi layer. Furthermore, the non-local mesh "permeates" into the cSi bulk by a distance denoted by the *permeation* parameter. This results in the creation of paths at different energy levels in which the tunneling generation is calculated. It is worth noticing that, as for the local mesh, the adjustment of the parameters that define the non-local mesh is extremely important in order to obtain numerically valid results.

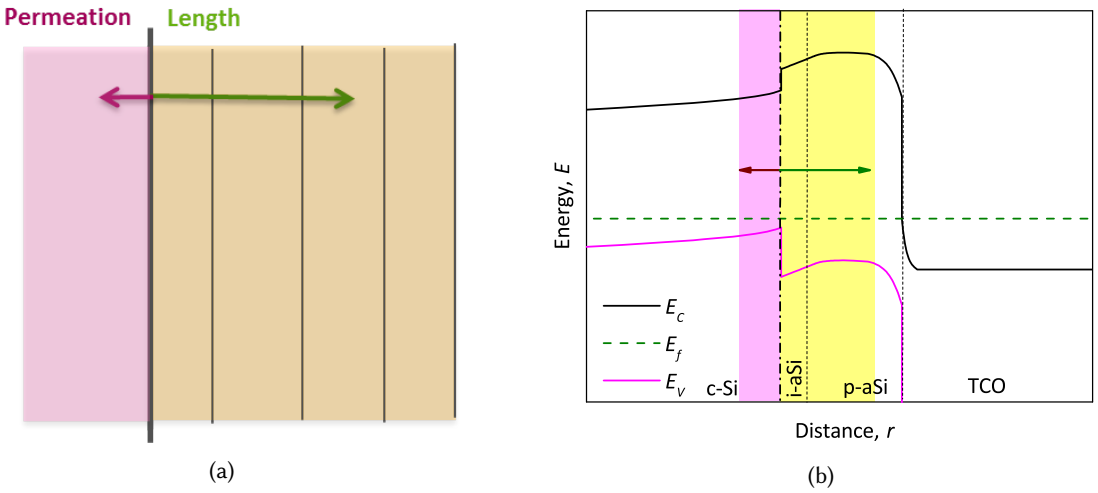

(a) (b)

Figure 3.7: **a)**Simplified scheme of non-local mesh and parameters **b)**Non-local mesh scheme in the cSi/aSi interface for IBC-SHJ p-contact stack.

3.5. The need of TAT implementation

The model introduced throughout this chapter, retrieved from Procel et al. [52], was validated for simulating IBC-SHJ cells with high conductive TCO (as defined in section 2.2.3). However, the reference cell used in this project, shown in section 3.2, presents ITO in its structure. This type of TCO, has a limited carrier density range as shown in figure 2.11, and thus limited conductivity. As shown in figure 2.10, band alignment at the contact stack, is highly sensitive to the TCO characteristics, hindering the carrier collection in certain cases. Moreover, as indicated in section 2.1.5, literature suggests that trap assisted tunneling mechanism starts dominating the charge carrier transport - in heterojunctions - in the absence of an ideal band alignment.

These observations raise the question: *Is TAT a dominating transport mechanism in IBC-SHJ solar cells comprising aSi and ITO in their structure?*

In order to answer this question, the next chapter will discuss TAT implementation in the aforementioned model.

4

TAT Implementation and Results

In this chapter, TAT implementation will be explained. To this end, the TAT models available in Sentaurus will be outlined in section 4.1, and the selection of the non-local TAT model will be justified. Then, in section 4.3, the simulation results - after the implementation of TAT - are presented. Next, the effect that the TCO and aSi traps have on the transport in IBC-SHJ will be analyzed. The research questions regarding TAT will subsequently be answered throughout this chapter.

4.1. Trap assisted tunneling modelling

TAT modelling presents a challenge, not only from the physics point of view, but also numerically. In section 2.1.5, the concept of TAT was introduced and the most important variables involved in it were described. As for the other types of tunneling (i.e. direct and band to band tunneling), TAT can be modelled as a non-local process. This implies that the trap assisted tunneling not only depends on the energy level at which the charge carrier is placed, but also on the energy barrier that it needs to overcome in order to hop to the trap.

In addition, the aSi traps need to be implemented using the models described in section 2.2.2. Changing the trap distributions in the aSi layers also influences the activation energy of the deposited layer. Consequently, the doping needs to be newly adjusted (flowchart 3.5) to fit the experimental measurements provided by the reference cell.

To sum up, there are many factors involved in TAT modelling. The combination of all the factors makes it numerically challenging for the simulator, requiring intricate local and non-local mesh adjustments in order to guarantee convergence and optimal computational time.

4.1.1. TAT models

TCAD Sentaurus makes a range of models available to simulate trap-assisted tunneling. On the one hand, certain approaches, such as Hurkx [64] and Schrenk [65], only consider local variables to model TAT. The advantage of these models is that they are easier to implement. Nonetheless, they are not suitable for modelling TAT in abrupt heterojunctions, in which the the band edge is more influenced by the material composition than the electric field [2].

On the other hand, while the **non-local TAT model** provides an exact calculation of the energy barrier by the WKB method, it proves more challenging to implement. Thus, it enables an accurate calculation of the TAT in heterojunctions which exhibit a more complex band structure. An expression to describe non-local TAT is presented in section 2.1.5 in equation number 2.30.

In particular, IBC-SHJ presents an abrupt heterojunction, exhibiting - as shown in figure 2.2 - a specific energy barrier shape. Therefore, in order to achieve accurate results, the chosen model is the non-local TAT model. In addition, Sentaurus offers the possibility of coupling non-local tunneling with traps. In order to do so, it is crucial to implement non-local tunneling and specify the trap distribution which will be coupled to this process. As described in 3.4.2, non-local tunneling was implemented with the creation of a non-local mesh (figure 3.7). For TAT, however, the creation of an additional non-local mesh is demanded.

4.1.2. Non-local mesh

In order to implement the second non-local mesh, it is necessary to first analyze the region in which TAT occurs. In the particular case of IBC-SHJ, TAT is likely to occur between the the cSi/aSi and the aSi/TCO interfaces. The non-local mesh at the cSi/aSi interface was previously defined for modelling the tunneling (section 3.4.2). In addition to that, as shown in figure 4.1, another non-local mesh needs to be defined in order to simulate the tunneling path that the charge carrier follows along both interfaces. Accordingly, the interface between aSi/TCO is selected for implementation of the second non-local mesh.

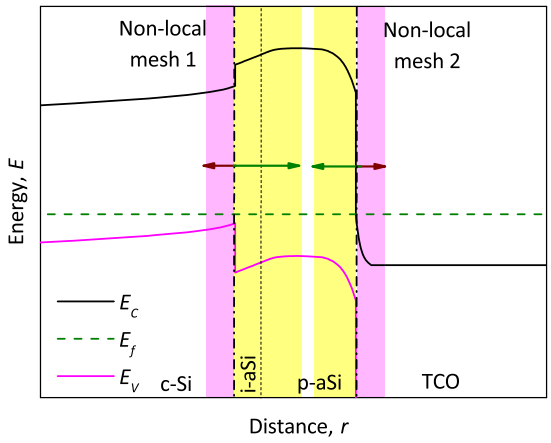

Figure 4.1: Scheme of non-local meshes implemented for non-local TAT model.

The creation of an additional non-local mesh raises a numerical challenge. Thus, adjusting the mesh parameters (figure 3.4.2) is essential to achieve convergence and optimal computational time. Furthermore, in addition to the non-local mesh, setting the optimal local mesh refinement parameters (section 3.2.1) is also of importance. Consequently, as shown in the flowchart depicted in figure 4.2, an iterative process is needed to fix local and non-local parameters.

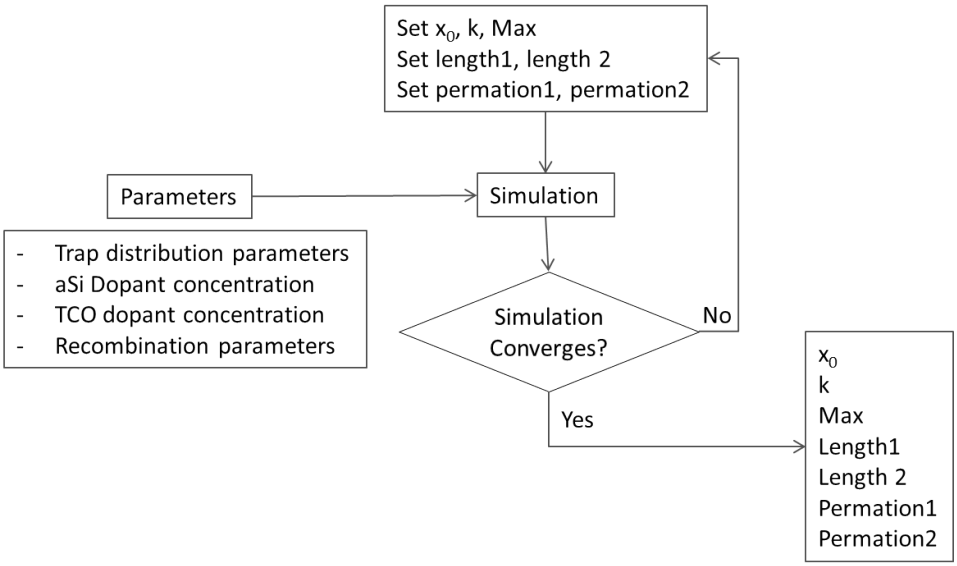

Figure 4.2: Flowchart used to adjust local and non-local mesh parameters.

4.1.3. Trap implementation

Non-local TAT is also modelled according to the material containing the traps which assist the transport. In this case, this is amorphous silicon. As previously mentioned, the defect states in aSi can be modelled as described in section 2.2.2. Therefore, in this work, as in the conventional model, the tail states are modelled as exponential distributions (eq. 2.33 and 2.32) and the defect states as two Gaussian distributions (eq. 2.34 and 2.35). Moreover, the Pool-Frenkel model is used to more accurately model the energy level of the defect states at the aSi doped layers.

Accordingly,the trap parameters, found in equations 2.32, 2.33, 2.34, and 2.35, are set to characterize each aSi layer: i-aSi, n-aSi and p-aSi. This results in three different trap distributions as shown in figure 4.13.

Moreover, the capture cross section is an important parameter used to characterize the traps. Selecting the appropriate capture cross section model is essential to simulate TAT. Consequently, in this work **the Poole-Frenkel capture cross section model** [66] is used. This model - usually chosen for amorphous films - predicts an enhanced emission probability in trapping centers [2].

4.2. Input parameters

The simulations of the following section are performed following the simulation approach mentioned in section 3. In addition, the input parameters for the selected models are summarized in table 4.1, adapted from [3].

Furthermore, the geometry of the reference IBC-SHJ cell is described in section 3.2. In this work, in particular, the dimensions of the reference cell are derived from a real device and can be found in table 4.1. Note that in order to save computational time when running simulations in the TAT study, the front surface of the cell is considered flat.

Lastly, two sets of trap distributions are initially used in the simulations - *SET I and SET II* - whose parameters are contained in table 4.2.

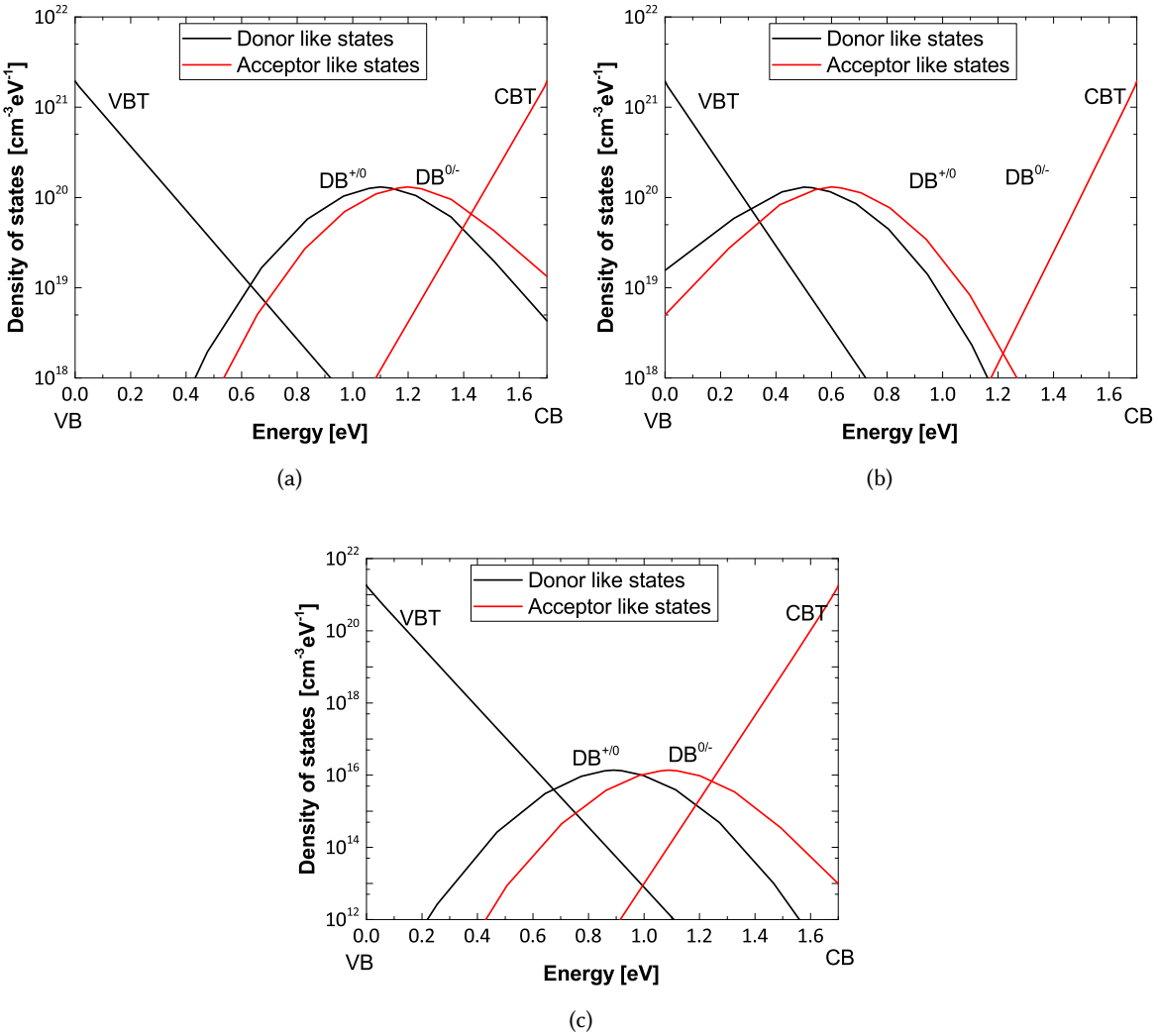

Figure 4.3: Trap distibution models of **a)** p-doped aSi layer, **b)** n-doped aSi layer and **c)** intrinsic aSi layer

4.3. Results and discussion

Now that TAT is implemented, the research questions could becan be addressed. In order to do so, the influence of each heterointerface is analyzed in the following sections. Firstly, the influence of the TCO is studied. Then, the effect of the trap distributions in the aSi is investigated.

4.3.1. TCO influence

First of all, relevant parameters are identified by observing the band diagrams of the contact stacks in figure 4.4. The activation energy of the p layer ($E_{a,p}$) and the n-layer ($E_{a,n}$), is directly related to tunneling barrier (eq. 2.28, 2.29): a higher activation energy translates into a higher energy barrier [3]. However, ΔTCO is defined as the energy difference between the Fermi level and the conduction band at the TCO. This parameter serves as an indicator of the conductivity of the TCO, namely, the larger the ΔTCO, the larger the carrier density in the TCO, the more conductive the TCO is. This reasoning can be found in section 2.2.3.

Indeed, as depicted in figure 4.5, ΔTCO is particularly relevant for the p-contact since it clearly

Parameter	Simulated device	Parameter	Simulated device
Bulk SRH lifetime	12 ms	SiN thickness	75 nm
Surface SRH SRV	0.1 cm/s	aSi/front thickness	5 nm
Bulk resistivity	3 Ω cm	n-type c-Si thickness	190 μm
χ i-a-Si:H and doped layers	4 eV	i a-Si:H thickness (n/p)	5 / 8.5 nm
m_t for i-aSi:H and doped layers	0.1 m_0	n-doped a-Si:H thickness	27 nm
i-a-Si:H bandgap	1.7 eV	p-doped a-Si:H thickness	22.5 nm
Doped layer bandgap	1.7 eV	ITO thickness	75 nm
ITO bandgap	3.1 eV	Cu thickness	3.1 μm
TCO work function (WF_{TCO})	variable 4.9	$E_{a,p}$	340 meV
Carrier concentration in TCO	4.9×10^{19} - $1 \times 10^{20} cm^{-3}$	$E_{a,n}$	201 meV
TCO electron or hole mobility	160 or 40 cm^2 /V s		

Table 4.1: Summary of general IBC-SHJ device parameters

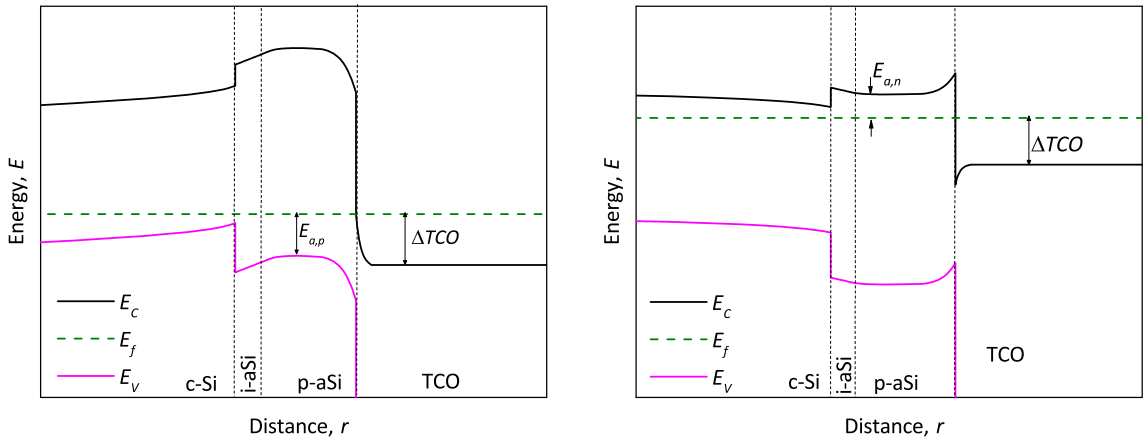

Figure 4.4: Band diagrams of **a)**p-contact and **b)**n-contact, defining activation energy ($E_{a,p}$,$E_{a,n}$) and ΔTCO as an indicator of the TCO conductivity.

influences the band alignment between the aSi and the TCO. An indication of the change is illustrated in the figure with ΔE. It is observed that for low values of ΔTCO, there is a positive energy difference ΔE, contributing to the band misalignment. On the contrary, for a high ΔTCO - *highly conductive TCO* - ΔE acquires negative values, indicating good band alignment.

The cell is simulated for a range of values of ΔTCO from 140 to 600 meV while maintaining a constant activation energy (E_p=340meV and E_n=210meV). This range of values is selected according to figure 2.11, where typical values of TCO $E_F - E_{VB}$ are provided. Initially, the simulations are performed without implementing TAT, therefore thermionic emission, direct tunneling and band to band tunneling are considered as the only transport mechanisms present at the hetero-interfaces. It can be observed from figure 4.6a that the cell exhibits a regular JV curve for a high conductivity TCO, whereas for a lower ΔTCO, the result shows that the device does not work as a solar cell. Subsequently, TAT is implemented in the simulations, resulting in the JV curves shown in figure 4.6b. Here, it is observed that at low TCO conductivity, the JV curves display a normal functioning of the cell, suggesting that TAT tunneling plays an important role in the carrier transport in the

		SET I [67]			SET II[68]		
Parameter	Unit	p-layer	i-layer	n-layer	p-layer	i-layer	n-layer
N_{v0},N_{c0}	$eV^{-1}cm^{-3}$	$2 \cdot 10^{21}$			$3.85 \cdot 10^{21}$		
Valence Band Tail Parameters							
E_{v0}	eV	0.12	0.05	0.094	0.100	0.045	
σ_n^+	cm^2	$7 \cdot 10^{-16}$			$2.16 \cdot 10^{-14}$		
σ_p^0	cm^2	$7 \cdot 10^{-16}$			$2.16 \cdot 10^{-15}$		
Conduction Band Tail Parameters							
E_{c0}	eV	0.08	0.035	0.068	0.065	0.027	
σ_n^0	cm^2	$7 \cdot 10^{-16}$			$2.16 \cdot 10^{-15}$		
σ_p^-	cm^2	$7 \cdot 10^{-16}$			$2.16 \cdot 10^{-14}$		
Dangling Bond Parameters							
N_{db}	cm^{-3}	$1.31 \cdot 10^{20}$	$1.38 \cdot 10^{16}$	$1.31 \cdot 10^{20}$	$4 \cdot 10^{18}$	$1.46 \cdot 10^{15}$	$8.0 \cdot 10^16$
σ_{db}	eV	0.21			0.2		
σ_p^-,σ_n^+	cm^2	$3 \cdot 10^{-14}$			$5.05 \cdot 10^{-13}$		
$5.05 \cdot 10^{-13}$	cm^2	$3 \cdot 10^{-15}$			$\sigma_p^-/10$		

Table 4.2: Overview of trap parameter values for SET I and SET II

heterojunction. On the other hand, it can be seen from the curves, that the decrease in ΔTCO translates into a similar effect to series resistance, lowering the FF. Indeed, this trend is confirmed in figure 4.6c, where the FF raises as ΔTCO increases. In particular from 150 to 300 meV, the FF shows a rapid increase up to approximately 83%, however, after that, it becomes more stable.

From these results, it can be concluded that tunneling and thermionic emission play a minor role in charge carrier transport at low ΔTCO values. There is an additional transport mechanism that dominates in this particular case, *TAT*. In fact, In figure 4.6c the shadow area indicates the TCO energy range at which TAT needs to be implemented in the model in order to obtain the results in accordance with a working solar cell device. The threshold was found at a value of ΔTCO=315 meV.

This statement confirms the initial hypothesis under which TAT was implemented, as indicated in section 3.5. Indeed, TAT is not only present but also necessary for the correct functioning of the cell. Thus, the next step is to identify in which layer this transport mechanism is more relevant. Notice that for the rest of the study, a typical value for ITO, ΔTCO=200meV is taken as the reference value, since it is within the range of typical values for ITO [8].

4.3.2. Influence of TAT in each layer

This section addresses one of the research questions: In which layer of the contact stack is TAT more relevant for the correct functioning of the cell?

In order to answer this question, it is necessary to recall the layers that are involved in both contact stacks. Both the p-contact and n-contact are composed of a thin layer of intrinsic aSi and a thicker layer of p- and n-doped aSi, respectively. Therefore, in this study, 4 different layers are considered: i-aSi/p and i-aSi/n being the intrinsic aSi layer on top of the p and the n contact respectively,

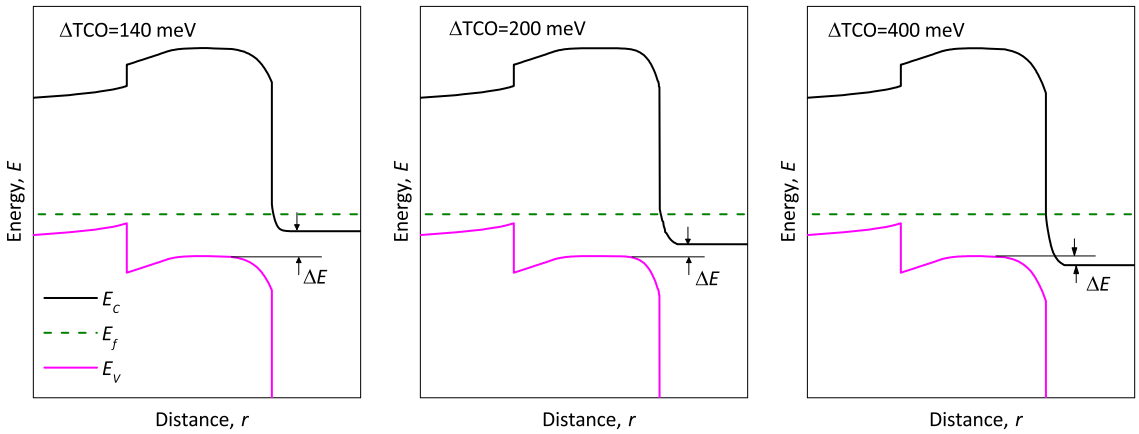

Figure 4.5: p-contact band diagram illustrating the impact of ΔTCO variation on the band alignment (ΔE)

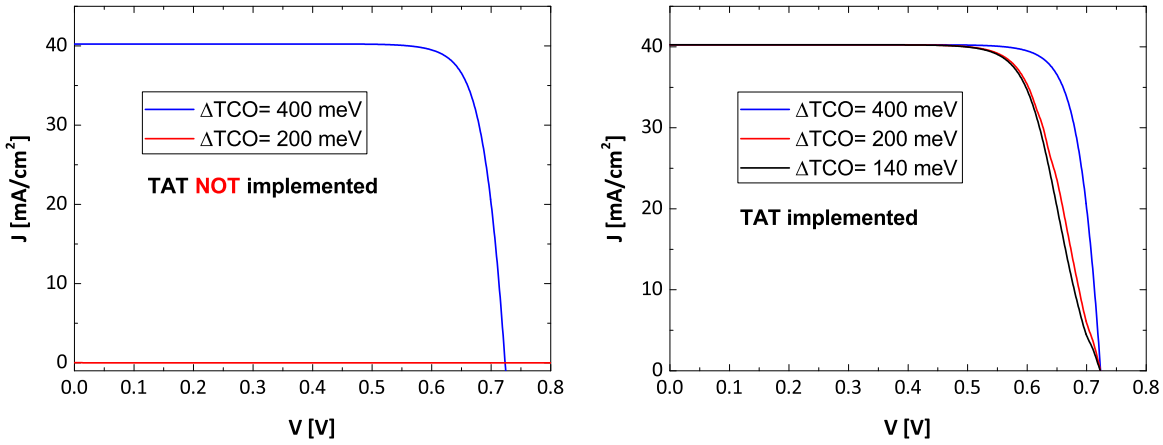

(a) (b)

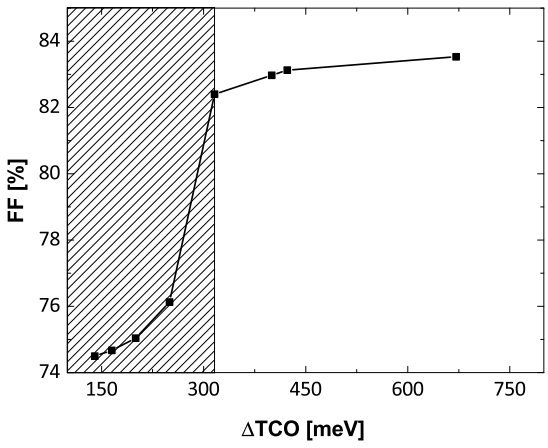

(c)

Figure 4.6: JV curves of IBC-SHJ obtained for different ΔTCO, in **a)** TAT is not implemented while in **b)** TAT is implemented. Figure **c)** shows FF as function of ΔTCO. The shaded area indicates the range in which TAT implementation is necessary for a valid simulation.

and the p-aSi and the n-aSi layer corresponding to the doped aSi of the contact stacks.

The TAT model implemented in the simulations, can be enabled or disables for each layer separately. As simulation approach, the trap assisted tunneling is activated in each layer individually. This process is carried out for two different trap distributions, SET I and SET II, which characteristics values can be found in table 4.2.

The JV curves obtained in the experiments are shown in figure 4.7. Here, it is observed that by activating the TAT in the intrinsic layers only, the cell malfunctions. As seen on the inset of the graph, the cell exhibits resistor behaviour, and there is therefore not an effective carrier collection.

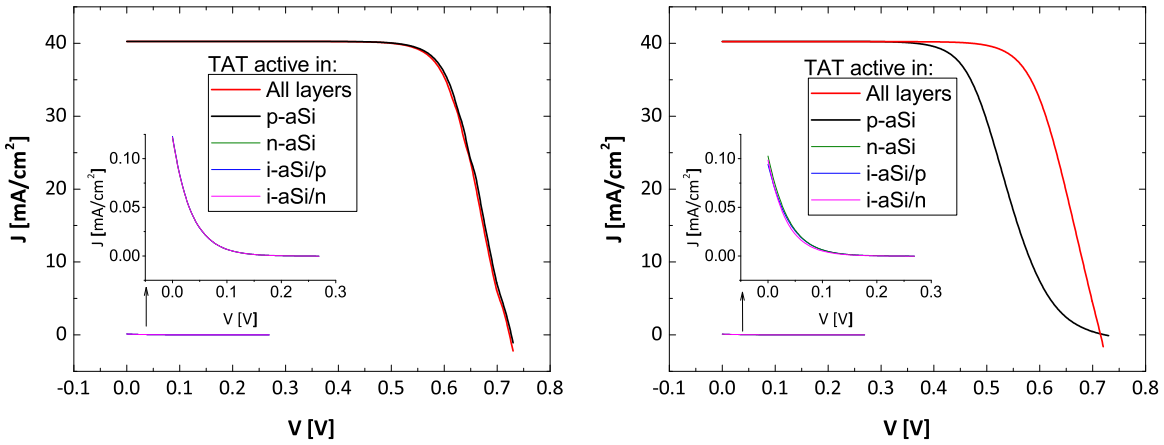

Figure 4.7: JV curves obtained by activating TAT in each aSi layer individually for different trap distributions **a)** Trap SET I and **b)** Trap SET II.

In the case of enabling TAT only in the p-doped layer, the same effect as for the intrinsic layers is shown, trap-assisted transport exhibits a negligible influence in the p contact. In order to explain this results, it is necessary to recall the band diagram of the p contact displayed in figure 4.4. From the figure, it is observed that the electron transport only occurs at the conduction band, therefore the tunneling path that the electron follows does not experience any discontinuity by transitioning to another band, as it is the case of the p contact. Accordingly, the band alignment and the dominant transport mechanisms at the n contact do not vary for lower ΔTCO values.

Lastly, TAT is activated solely in the p-doped layer of the contact stack. Unlike the others, the aSi p-layer appears to have a considerable impact in the performance of the cell. According to the JV curve displayed in figure 4.7a, uniquely enabling TAT in that layer results in the exact curve as activating the mechanism in all the layers simultaneously. Again, analyzing the band diagram displayed in figure 4.4 and in 4.5, it can be seen that the path that the holes follow - from the p-doped aSi valence band to the TCO conduction band - highly depends on the band alignment, represented by ΔE. Concurrently, as previously described, the band alignment directly correlates to the conductivity of the TCO with ΔTCO. Thus, it is expected that, for lower values of ΔTCO, band-to-band tunneling is unlikely to occur since the energy level at both sides of the interface do not match. Therefore, the holes are forced to follow a different path in order to be collected at the TCO. Indeed, from the results it is observed that, for low conductivity TCO, the holes are assisted by traps to hop to the TCO inter-

face. The relevance of this transport mechanism at the p-contact is thus highlighted. However, the results - obtained for SET II - shown in figure 4.7b, slightly differs from the last one. Here, only implementing TAT at the p-layer does not present the same JV curve as when implementing it in all the the layers. Thus, it can be concluded that the trap distribution has an influence on the effectiveness of the TAT.

In summary, in this section, the question - *In which layer of the contact stack is TAT more relevant for the correct functioning of the cell?* - is answered. TAT at the aSi p-doped layer is crucial for the correct cell functioning, in particular, when the energy band exhibits low ΔTCO, at 200 meV. The conclusion becomes evident by the simulation results and the analysis of the band diagrams of both n- and p-contacts. Moreover, different results are obtained for different trap distributions, which raises the next question: how does the trap distribution influence the transport at the p-contact?

4.3.3. Influence of trap distributions in aSi p-dope layer

In this section, the next scientific question is addressed, *how does the trap distribution at the p-doped aSi layer influence the transport?*.

The trap distribution (SET I) of the p-doped aSi layer is illustrated in figure 4.8a. Here, four different distributions can be differentiated: conduction band tail (CBT), valence band tail (VBT), neutral/acceptor dangling bonds ($DB^{0/-}$) and donor/neutral dangling bonds ($DB^{+/0}$).

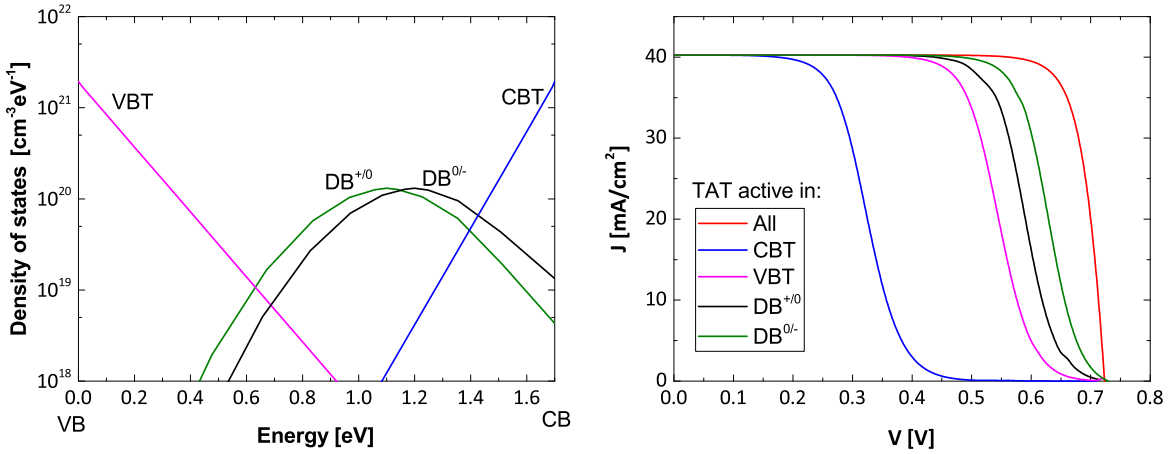

(a) (b)

Figure 4.8: **a)** Trap distribution at the p-doped layer. **b)** JV curves obtained by implementing TAT in each trap distribution (indicated by a)). The impact that dangling bond defects have on TAT transport is highlighted.

The approach followed in this study lies under the same principle as in the previous section. Subsequently, TAT is only implemented for an individual distribution in each experiment. Hence, the remaining trap distributions are considered to contribute to other recombination processes such as SRH. In figure 4.8b, the resulting JV curves from each simulation are shown. Here, it is observed that the trap-assisted transport make use of the traps - represented by each distribution - at different degrees. For instance, when only the CBT participates in TAT, the cell exhibits a remarkably poor transport quality. Whereas, by only considering the dangling bonds traps, the FF becomes closer to the one exhibited by a working solar cell. Consequently, the relevance of each distribution concerning

the hole collection at the p contact, can be ranked as follows:

1. Dangling bonds ($DB^{+/0}$ and $DB^{0/-}$)
2. Valence band tail (VBT)
3. Conduction band tail (CBT)

From the results, it can be concluded that the traps at the aSi do not contribute equally to the transport. Accordingly, at a band diagram level (figure 4.5), it can be observed that the energy level of the TCO conduction band is adjacent to the aSi valence band. Thus, traps located at an energy level near the aSi conduction band, such as the conduction band tail, may not present an appropriate intermediate energy level to assist the transport.

In order to complete the analysis and confirm the initial hypothesis, each distribution is further studied in the next sections.

Influence of the conduction band tail

The first object of the study is the conduction band tail. This distribution is, as its names suggest, a continuation of the conduction band. The defects represented by the CBT are at a shallow energy level. Typically these traps are treated as charged vacancies, as they have low perturbation in the lattice.

As previously mentioned, the CBT is described by an exponential distribution which is defined by its characteristic band tail density of states, N_{C0}. In the overall distribution, the effect of increasing N_{C0} is depicted in figure 4.9a. Then, simulations are carried out to study the effect of such an increase. As a result, a minor decrease in the FF can be observed in 4.9b. In fact, by increasing the defect concentration by an order of magnitude of 2, a decrease of 0.3% in the FF is observed.

Thus, it can be concluded that the effect of the traps in the conduction band tail is nearly negligible. In addition, it is worth noticing that the activation energy of the p-layer remains constant. This suggests that acceptor defects near the conduction band have a negligible influence in a p-doped layer activation energy. This phenomena can be explained by observing that the doping atoms present in this layer (at the valence band energy level), have a stronger influence on the Fermi level position.

Influence of the valence band tail

Similar to the CBT, the valence band tail, is described by an exponential function defined by a characteristic valence band tail density of states, N_{V0}. These defects are also shallow since they do not cause a large disturbance in the lattice. They are treated as donor like states. Consequently, as observed in figure 4.10a, the donor nature of the VBT defects counteract the effect of the acceptor doping atoms at the p-layer. Subsequently, as shown in 4.10b, increasing the density of states of the VBT rapidly increases the activation energy of the p-doped layer, reaching up to 600 meV. Therefore, the experiment is conducted with two doping concentrations: the original doping density denominated as 'low N_A', and a high doping concentration denominated 'high N_A'.

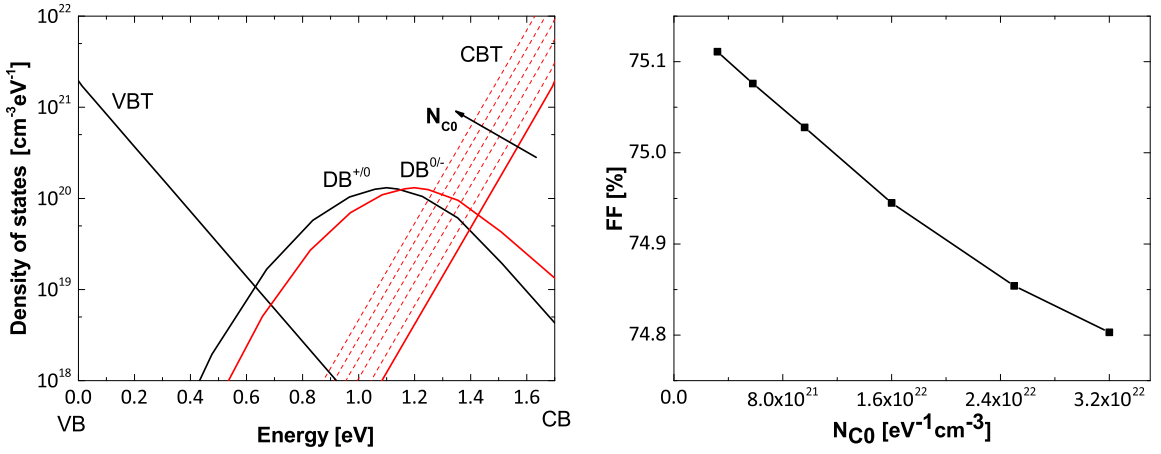

(a) (b)

Figure 4.9: **a)** p-doped aSi layer trap distribution, the dotted line indicates the effect of augmenting the conduction band tail density of states (N_{CO}). **b)** Impact N_{CO} increase in the FF of the cell. Clearly, the decrease in FF is nearly negligible.

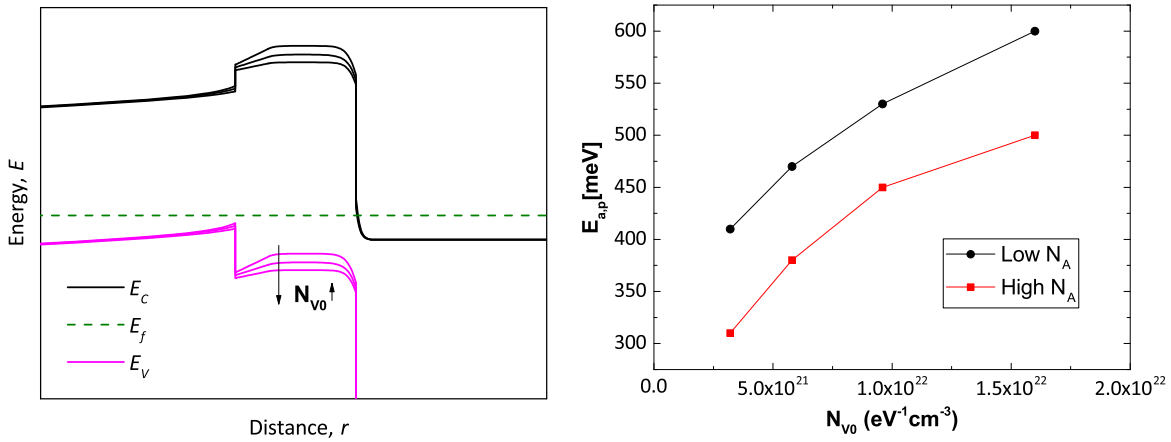

(a) (b)

Figure 4.10: **a)** p-contact band diagram, illustrating the impact that the variation of the valence band tail density of states (N_{V0}) has on band bending. **b)** Activation energy as a function of the N_{V0} for different doping concentrations (N_A). It is observed that N_{VO} decreases the band bending of the valence band, thus causing an augmentation of the activation energy.

The same simulation approach described in the previous section is followed in this case. The characteristic energy of states N_{V0} is increased as indicated in figure 4.11a. Accordingly, the effect of this change in the performance of the cell can be observed in figure 4.11b. Here, for low doping concentrations, a steep decrease in the FF - down to 20% - is observed while N_{V0} increases. This is caused by the aforementioned increase in activation energy. As discussed in literature [3], the effectiveness of the carrier collection is extremely sensitive to the activation energy. However, this effect can be counteracted by increasing the doping concentration, for high doping concentration, the diminution of FF accounts only for 10% as N_{V0} is increased. Again, this behaviour is explained by the activation energy change at the p-layer.

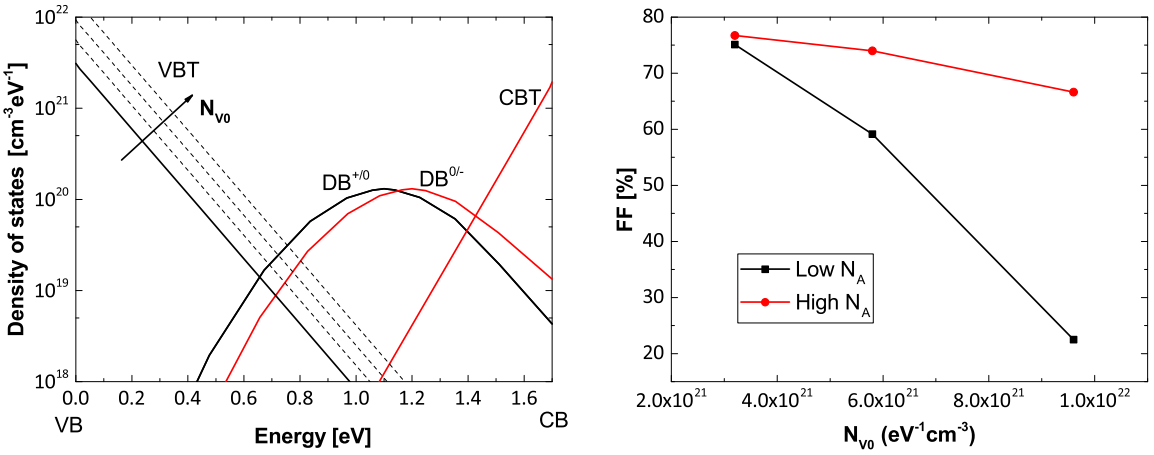

(a) (b)

Figure 4.11: **a)** p-doped aSi layer trap distribution, illustrating the effect of increasing the VBT density of states (N_{V0}) with dotted lines. **a)** FF of the cell as a function of N_{V0} for different doping concentrations. It is observed that increasing the density of states of the VBT causes a decrease in FF.

To summarize, increasing the density of states at the valence band tail results in a rise in the p-layer activation energy. Simultaneously, this escalation causes a worsening of the charge carrier transport as the energy barrier increases. Consequently, the FF rapidly decreases, especially for low doping concentrations.

Influence of the dangling bonds

The dangling bonds are generally considered as deep traps, since they are close to the midgap energy level. They are described by the superposition of two Gaussian distributions: donor ($DB^{+/0}$ and acceptor ($DB^{0}/-$) like. The Gaussian distributions are defined by the characteristic dangling bond density of states N_{db} and the energy level at which the distribution presents its peak, $E_{DB}^{+/0}$ and $E_{DB}^{0/-}$ respectively.

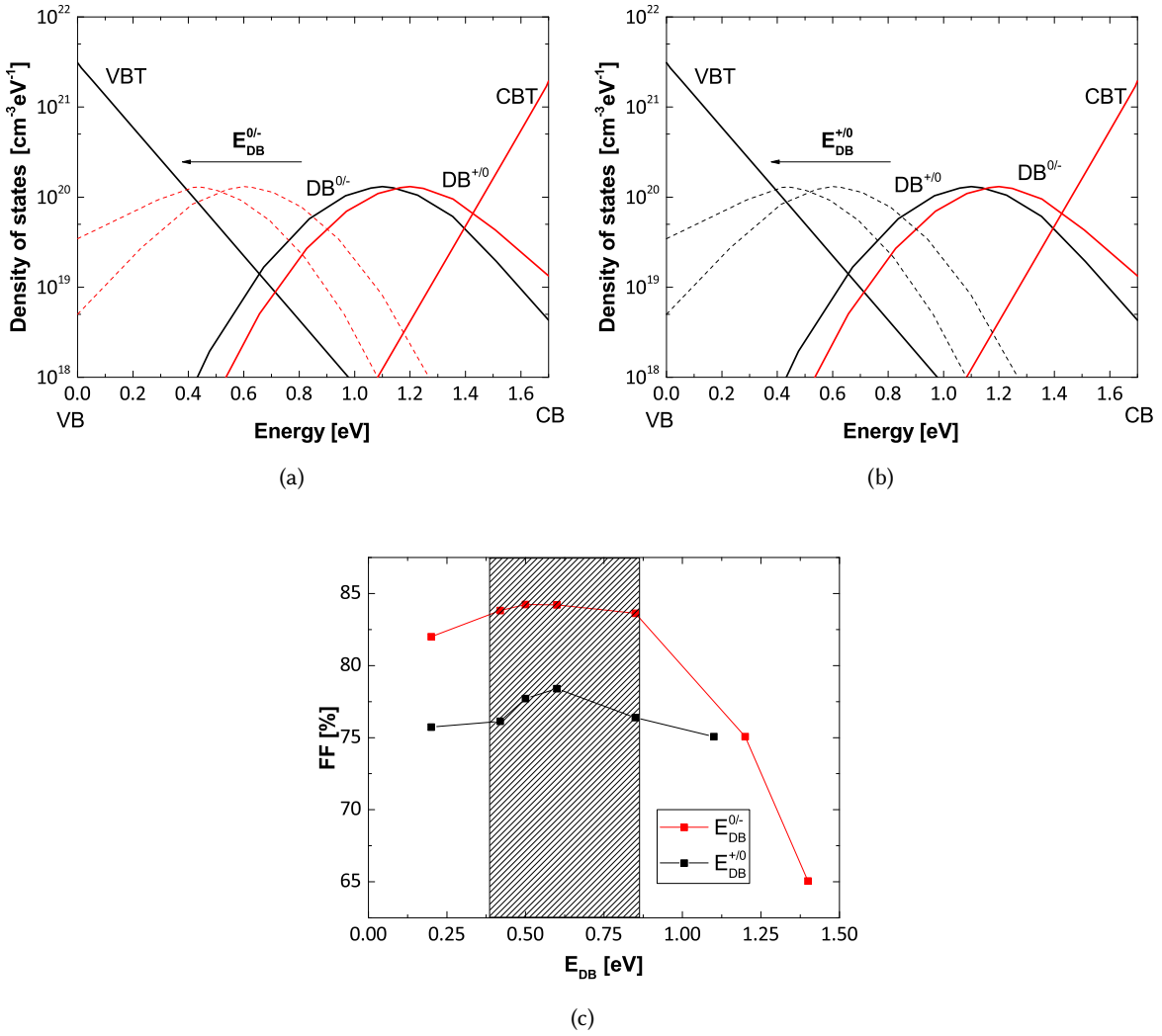

Figure 4.12: p-doped aSi layer trap distribution, illustrating the impact of **b)** Displacing the acceptor-like DB distribution and **a)** Displacing the donor-like DB distribution. **c)** FF as a function of the peak energy level of the DB distributions. Here, the FF reaches a maximum at a peak energy level ranging between 0.4 and 0.8eV.

In this section, the effect of varying the dangling bond distribution parameters on the cell performance is studied. Firstly, as shown in figure 4.12a, the energy level of the peak density of states is altered for each distribution independently. The result of this experiment is shown in figure 4.12c, illustrating the change that the FF experiences by displacing the trap distributions. Interestingly, the FF reaches up to nearly 85% when the acceptor like Gaussian distribution peaks at an energy level between 0.4 and 0.8 eV. Moreover, the result obtained for the $DB_{+/0}$ distribution, showed the maximum FF at the same energy levels, however, the value reached is 7% lower than the first case.

Referring once again to the band diagram (figure 4.4a), the dangling bond peak density energy level at which maximum FF is reached, matches with an energy level ranging from the VB band offset to the midgap. The results therefore suggest that the traps located at that energy level assist the charge carrier transport.

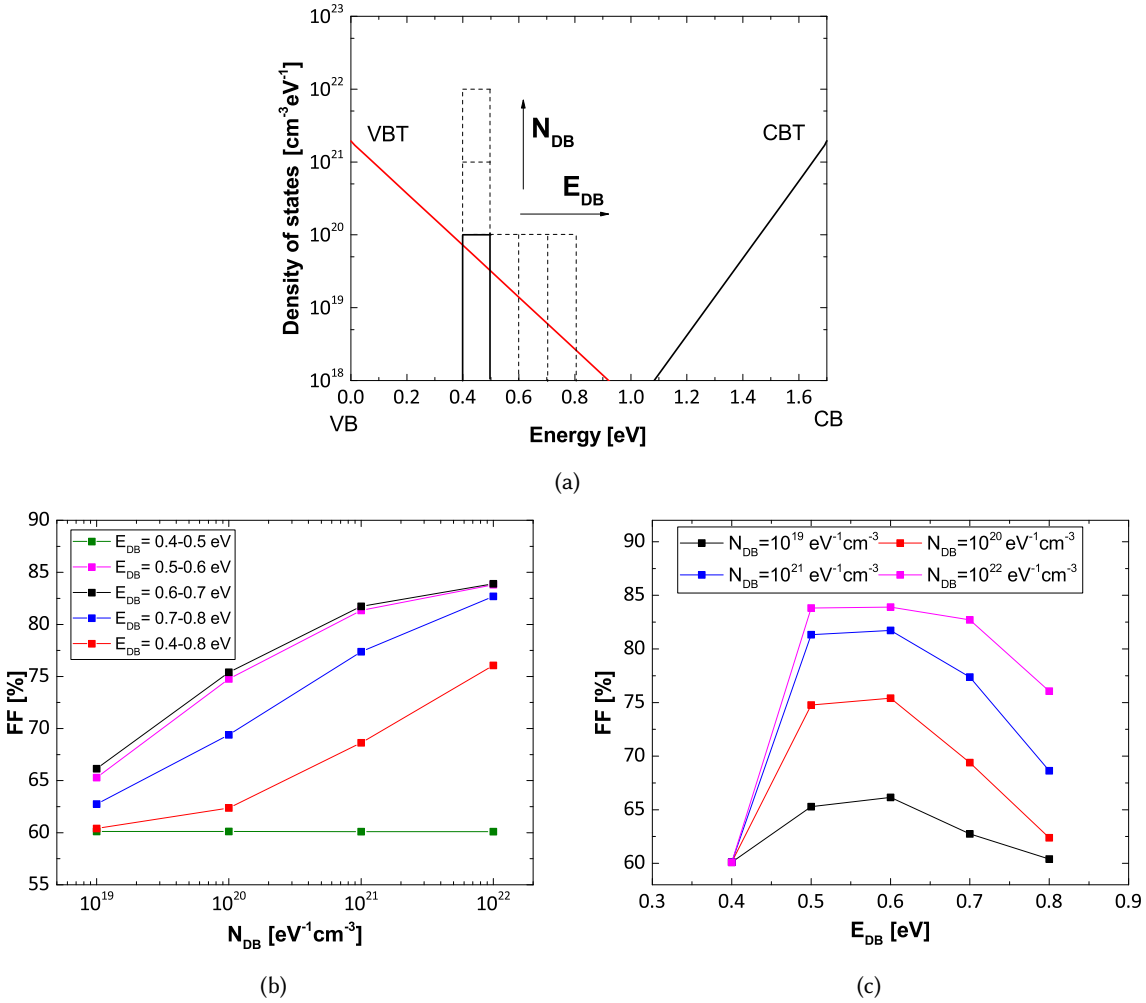

Figure 4.13: **a)** p-doped aSi layer trap distribution, substituting the DB Gaussian distribution by a variable constant distribution. **b)** FF as a function of the dangling bond density for different energy levels. **c)** FF as a function of the dangling bond constant distribution energy level for different DB concentration. It is observed that the FF peaks at 85% for high DB concentration at an energy level ranging from 0.5-0.6eV.

To further analyze the effect of the traps at such energy levels, a constant (neutral) trap distribution, as shown in figure 4.13a, is implemented. Both the energy level and dangling bond density are varied in this study. Consequently, the constant trap distribution is moved from 0.4eV to 0.8eV, obtaining values from 10^{19} to $10^{22} eV^{-1} cm^{-3}$. It is worth noticing that the band tails are also implemented and kept constant throughout the simulations at the values defined by SET I.

From the results in figure 4.13b, it can be observed that by increasing the defect density at an energy level ranging from 0.5eV to 0.8eV, the FF experiences an augmentation of around 20%. The maximum, however, occurs at an energy level of 0.5-0.6eV as shown in figure 4.13c. From the results, the fundamental energy levels for assisting the transport at the heterojunction are made evident. In addition, by observing the FF it can be seen that by increasing the number of traps, the performance of the cell is enhanced.

Finally, in figure 4.14, the FF - as a function of the characteristic energy and density of defects - is visualized. Once again, the simulation results highlight that the presence of traps at 0.5-0.6eV is

crucial for the effectiveness of the transport at the cell.

Remarkably, by comparing the trap distribution and the band diagram energy characteristics, it can be observed that the energy level at which the traps enhance the transport also matches the Fermi level. Interestingly, the transport is favoured by the traps located at the energy level in which the carrier concentration is higher.

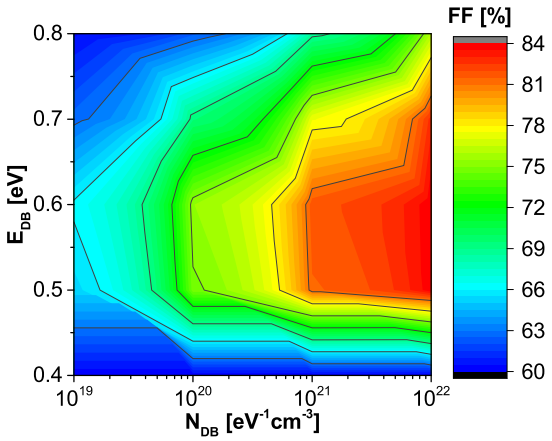

Figure 4.14: FF as a function of the dangling bond density and energy level. It is observed that the higher the density, the higher the FF, peaking at an energy level of 0.5-0.6eV.

After having concluded that certain traps in aSi are not only not detrimental, but are in fact beneficial for the carrier collection in IBC-SHJ configuration, a final question is raised: how are the traps in aSi modified at a physical level? In the next section, some light will be shed in this matter.

aSi defect states manipulation techniques

The light-induced metastability of aSi, or so-called Staebler-Wronsky effect (SWE), is observed after exposing aSi to light. This phenomena is described by an increase in neutral dangling bonds [7] in the aSi layer. The SWE effect has always been considered a problem for aSi solar cells, since a decrease in efficiency of these cells can be detected after they have been exposed to light for a prolonged period of time. Indeed, increasing the defect density may lead to an increase in recombination current, thus, worsening the performance of the cell.

Conversely, as proven in the previous sections, defect states at a certain energy level may enhance the charge collection in IBC-SHJ. Subsequently, the SWE effect may not be detrimental for this configuration. The challenge therefore resides in how to manipulate the defect density.

Melkens et al. [69] suggests three different ways of manipulating sub gap states:

- Light soaking
- Applying a voltage bias
- Thermal annealing

In the aforementioned study, Fourier Transform Photocurrent Spectroscopy (FTPS) was used to monitor the changes in the sub gap states while applying the aforementioned manipulating techniques. It was suggested that light soaking has a considerable impact on the midgap states (0.5-0.8

meV from the valence band). Moreover, Wronski et al. [70], reported the importance of light induced effects at an energy level of 0.4eV below mid gap. Interestingly, the defect energy levels reported by these studies match the energy level at which traps - in this work - have shown to enhance charge carrier transport in IBC-SHJ.

Furthermore, Kobayashi et al. [9] reported an increase of efficiency in silicon heterojunctions induced by light soaking. The results are summarized in figure 4.15 below:

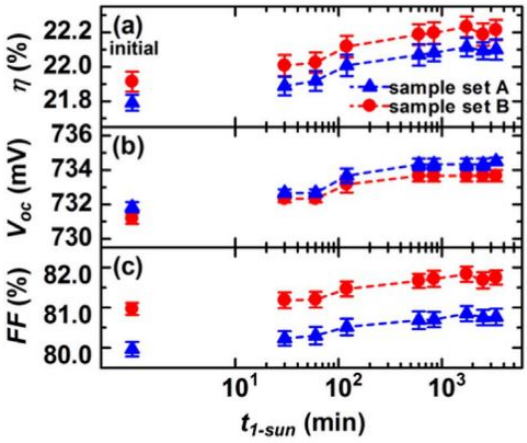

Figure 4.15: Measured efficiency (η), FF and V_{oc} of SHJ cells as a function of prolonged time exposure (t_{1-sun}). Set A was illuminated on the p-side, while set B was illuminated on the n-side. [9]

Accordingly, an hypothesis can be made: charge carrier transport in IBC-SHJ is enhanced by light induced defects due to an increase in the TAT current. This research line has not been developed in this work, however, it is recommended to further study light soaking effects in IBC-SHJ.

4.4. Conclusion and discussion

This chapter discussed the TAT implementation in Sentaurus TCAD. The selection of the non-local TAT model is justified since the IBC-SHJ presents an abrupt heterojunction. Furthermore, additional adjustments in the mesh and aSi trap implementation are described. Besides this, the chapter aimed to present the results obtained after the successful implementation of TAT in the model. Subsequently, a thorough analysis on the relevance of the TAT in the different aSi layers is carried out. Furthermore, the effect that the trap distribution has on the transport is studied further.

In order to answer the main research question: *Is TAT a dominating carrier transport mechanism in IBC-SHJ?*

The following subquestions are raised throughout the chapter:

- *In which contact stack layer is TAT mechanism more relevant for the effective carrier collection?*
- *How do the aSi trap distribution influence the charge carrier transport?*

It is concluded that the TCO has a clear impact on the mechanisms through which the charge carriers are transported in the p-contact. This is due to the band alignment being sensitive to changes in the TCO carrier concentration. By means of simulations, TAT was proven relevant for cases in which

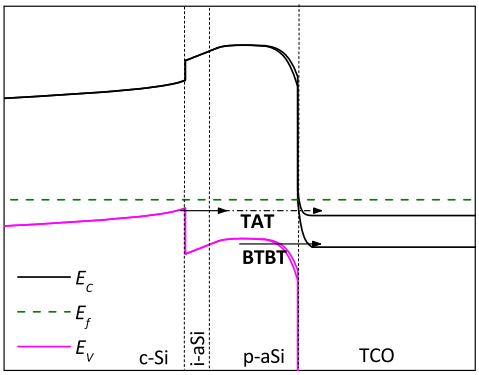

	Dominant transport mechanism
$E_{a,p} > \Delta TCO$	TAT
$E_{a,p} < \Delta TCO$	BTBT

Figure 4.16: Summary of the dominant transport mechanisms in the p-contact for different values of ΔTCO. It is shown that band-to-band tunneling dominates the transport for high ΔTCO, while TAT is relevant for lower values of ΔTCO.

$\Delta TCO < E_p$, as shown in figure 4.16. Therefore, it is concluded that TAT tunneling is dominant in the p-doped aSi layer. Moreover, the trap distribution in the aSi shows an effect on the quality of the transport at the heterojunction. It is observed that by increasing the trap density at the VBT, the FF decreases. Conversely, augmenting the defect density at the dangling bonds may have a strong positive impact on the FF. Furthermore, the effect of the trap energy level is studied, with the main results being summarized in figure 4.17, suggesting that at a range of 0.5-0.7eV the traps greatly contribute to the charge carrier transport. Finally, light is shed on aSi defect manipulation techniques, showing that, unlike for other types of configurations, aSi light induced effects might make a positive contribution in IBC-SHJ.

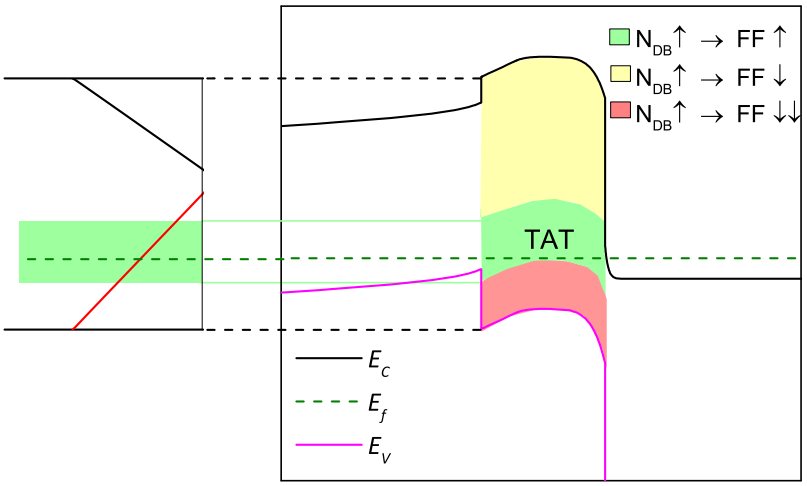

Figure 4.17: Overview of the impact of increasing the trap density, at different energy levels, on the transport at the p-contact. It is shown that the traps near the band offset and the Fermi level assist the charge collection.

5

Opto-electrical Calibration Results

In this chapter, the calibration of the reference IBC-SHJ cell will be developed. The purpose of the calibration is to assess whether the model accurately describes the device physics. Firstly, the optical calibration will be presented, followed by the electrical calibration. Furthermore, a comparison will be made between the calibration of the model described in chapter 3 and the model (with TAT implemented) used in chapter 4. In order to perform the calibration, the measured external parameters such as EQE, reflectance (R), J_{sc}, V_{oc}, FF and efficiency are compared to the ones obtained by means of the simulation.

This chapter aims to answer the last research question: *Can Sentaurus reproduce, in detail, the opto-electrical behaviour of an IBC-SHJ with aSi and ITO contact stacks?*

Note that the data provided by the reference cell (table 4.1) will be used in the simulations.

5.1. Optical calibration

The simulation approach described in chapter 3 needs calibration in order to asses whether the model describes the device physics in detail. To calibrate the optical parameters, the reflectance (R) curve is used since it exclusively depends on the optical properties of the device. In addition, the measured external quantum efficiency (EQE) is also compared to the simulation figures.

Initially, maintaining the parameters as defined in table 4.1, the simulated reflectance exhibits a mismatch with respect to the measured curved, as observed in figure 5.1. Particularly, for wavelengths ranging between 300-450nm and 1050-1200nm, the difference between the curves is more evident. As previously described in section 3.3, due to the limitations of the TMM method, the optical modelling is differentiated in two ranges of wavelength. Subsequently, the calibration is categorized in two parts, namely, 'short wavelength' and 'long wavelength'.

5.1.1. Short wavelength

Since short wavelength photons are generally absorbed or reflected in the top layers of the cell, the parameters that described the ARC layers need to be thoroughly adjusted. Subsequently, as the

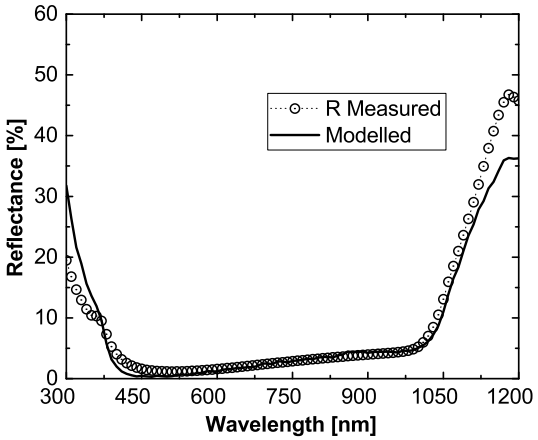

Figure 5.1: Simulated and measured reflectance as a function of wavelength prior to calibration.

optical properties (n&k) are provided, the ARC layers thicknesses are slightly varied.

As described in figure 5.2b, by decreasing the thickness of the SiN layer from the original value - 75nm - the overall reflectance of the cell decreases. This effect can be explained by the *destructive interference*, based on the principle that the thickness of the layer influences the wave interference, and thus the reflectance. Accordingly, an acceptable SiN is found at 70nm.

Furthermore, the impact of varying the aSi layer is illustrated in figure 5.2a. As in the previous simulation, it is observed that the overall reflectance increases with the thickness of the layer. In this case, the effect is less remarkable since the thickness of aSi is an order of magnitude lower than SiN. Consequently, the value that replicates the curve more accurately ranges between 2 to 4nm. The value is selected at 3nm.

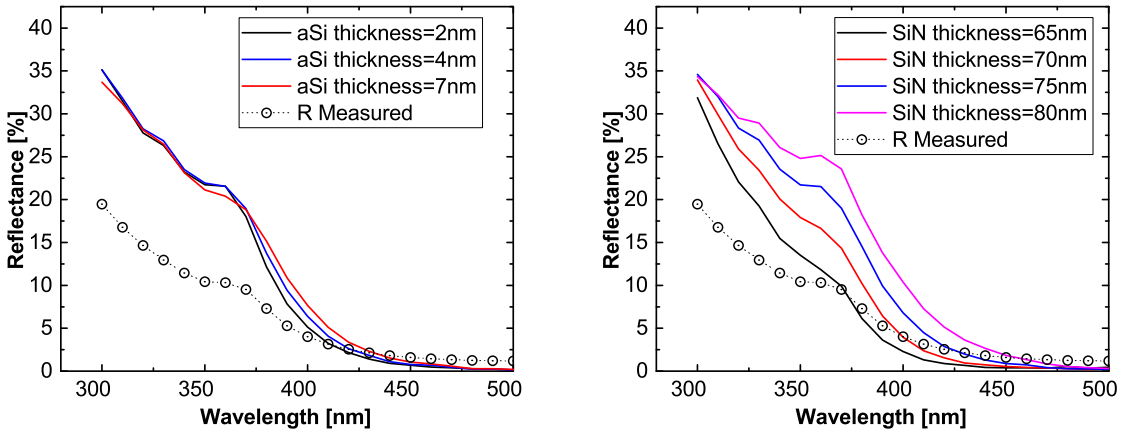

(a) (b)

Figure 5.2: Reflectance as a function of wavelength for different **a)** Front aSi thicknesses and **b)** SiN thicknesses. It is observed that reflectance increases with the thickness of the layer.

5.1.2. Long wavelength

Wavelengths between 850nm and 1200nm are comprised in the long wavelength category. In this range, the model assumes that the rays that are back reflected escape the cell, thus underestimating the long-wavelength photons scattering. As already described in section 3.3.2, a screen layer is placed above the illumination plane to reflect back a part of the photons that the model neglects. This screen layer is characterized with a reflectance value R_2, considered as a fitting parameter.

The effect of varying the reflectance of the screen layer is illustrated in figure 5.3. Here, the reflectance of the cell is evaluated as a function of the wavelength for both measured and experimental results. It is observed that by decreasing R_2, the overall reflectance increases. The increase in reflectance is explained by the fact that by lowering the reflectance of the screen layer, the model lowers the probability of a primary reflected photon being reflected back to the cell. Subsequently, based on the figures, the value of R_2 that fits the measured reflectance more accurately is selected. In this case, R_2 is selected to be 0.7.

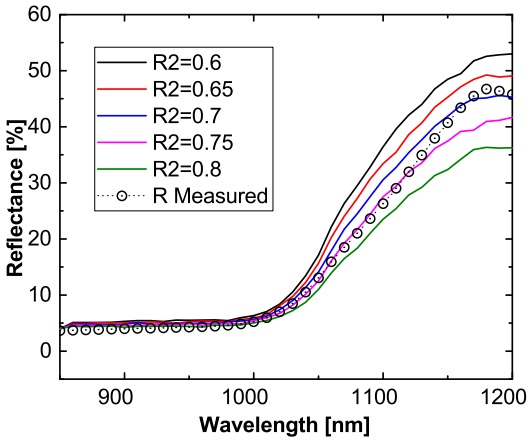

Figure 5.3: Reflectance as a function of wavelength for different R_2 values. R_2=0.7 resulting in most accurate fitting for the measured curve.

5.1.3. Optical calibration evaluation

The final optical fitting is shown in figure 5.4a, describing the reflectance and the EQE as a function of the wavelength. Here, a comparison between the measured and the final fitting results can be made. While the reflectance at long wavelengths is reproduced accurately, this is not the case for short wavelengths. From 300nm to 500nm, there is a mismatch in reflectance and EQE represented by the shaded area. Concerning the reflectance, the difference may be explained by the fact that the reference cell has a special front texture, that is not well represented by the random pyramids texture implemented in the model. The mismatch in EQE (0.8% of the total current), however, is not only due to the reflectance, but also because the model underestimates additional charge carrier generation. This discrepancy can be explained by a recent discovery - charge carrier recycling [71] - which states that the majority of the carriers generated in the aSi layer can be injected in to the bulk and eventually be collected. However, the simulation template only simulates the parasitic absorption of aSi, neglecting the carrier generation in the layers. Regarding long wavelengths, a

slight difference between the simulated curves, and the measured EQE and R, can be appreciated. Thus, a possible interpretation of the divergence, can lie in an overestimation of the absorption in the copper layer. As suggested by Temple [72], the absorption of a metal decrease with the size of the particles. Subsequently, it is recommended to analyze and modify the n&k data provided by [2] for copper.

Furthermore, the opto-electrical model used allows for estimation and quantification of the losses related to transmittance, free carrier absorption (FCA) and parasitic absorption of the IBC-SHJ. In figure 5.4b, the breakdown of the losses as a function of the wavelength is illustrated. The contribution of each loss is quantified by means of *implied current*, calculated by integrating the spectral loss with the AM1.5 photon flux. From the results, on the one hand, it is observed that at low wavelengths, the major loss is due to the parasitic absorption of the aSi layer, whereas SiN has a negligible effect. Due to the aSi's excellent absorption properties (section 2.2.2), even an extremely thin layer may have a significant impact on the parasitic absorption. On the other hand, regarding long wavelength, a considerable contribution to the losses is made by the p-contact stack, whereas the n-contact stack accounts for a fourth part of that quantity. The discrepancy can be explained by means of the area difference of both contacts, the p-contact being four times larger than the n-contact.

To conclude, the optical calibration is assumed valid from 500nm. Whereas for shorter wavelengths, further improvements in the model are needed in order to account the aforementioned phenomena. Overall, the relative error between the simulated EQE and the measured is 2%. Thus, it is worth noticing that since there is an underestimation of the optical generation profile, the error will be reflected in the electrical modelling as well, obtaining a current around 2% lower than the actual.

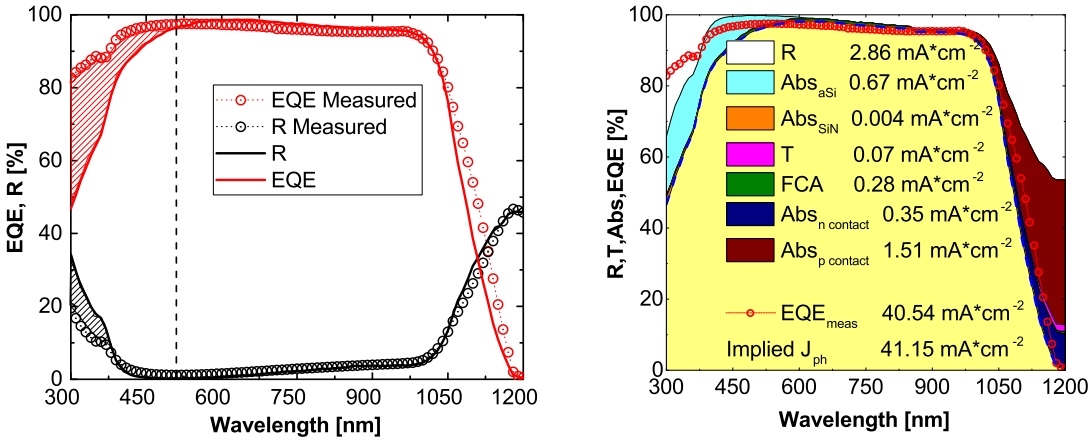

(a) (b)

Figure 5.4: **a)**Measured and simulated EQE and reflectance as a function of wavelength. The shadowed area indicates the mismatch between the fitting and the measured curve. **b)**Optical losses breakdown. Reflectance, transmittance, free carrier absorption and parasitic absorption in the front layers as well as contact stacks.

5.2. Electrical calibration

As described in section 2.1.3, the recombination processes can be categorized as intrinsic and extrinsic. Intrinsic recombination is inherent to the properties of the material, whereas the extrinsic

recombination is subject to external variables such as quality of the wafer, passivation techniques, etc. Therefore, the parameters characterizing extrinsic recombination, such as SRH (described in section 2.1.3, need to be adjusted to reproduce the behaviour of the real device. Accordingly, SRH bulk lifetime ($\tau_{Bulk,SRH}$) relates to the quality of the wafer, while the surface recombination velocity of the front (SRV_{front}), and surface recombination velocity at the interface between cSi and i-aSi in the p-contact region (SRV_p) and n-contact region (SRV_n), are related to passivation quality. Thus, these parameters are considered as variables in the following sections.

5.2.1. SRH bulk lifetime effect

Firstly, the influence of varying the bulk lifetime is studied. It is worth noticing that the lifetime of electrons and holes is set at the same value, indicating that the traps in the cSi are located at an intermediate energy level (section sec:shockley). Accordingly, the parameter is varied from 1 ms to 12ms, typical values range from 3-10ms [58]. Subsequently, in figure 5.5, the impact that such variation has on the short circuit current (J_{sc}), open circuit voltage (V_{oc}), efficiency, and fill factor (FF) is illustrated. Here, the red constant line represents the measurements reported from the reference cell for all of the four parameters. It is observed that for none of the lifetime values, the desired short circuit current is reached. The reason lies in the mismatch found in the optical calibration. On the other hand, the contrary occurs to the V_{oc}, where the reported value is achieved at an extremely low lifetime. Regarding the FF, it suffers from a rapid decrease for lifetimes lower than 3ms. Lastly, the efficiency decreases steadily from 12 to 5 ms, and continues to drop more steeply for lower values.

From the results it can be observed that lifetimes lower than 3-5ms make a considerable impact on the performance of the IBC-SHJ. However, the most remarkable influence is made in the FF, since a steep decrease is observed for low bulk lifetimes. This can be explained by the fact that charge carriers recombine in the bulk before reaching the contact, resulting in a worsening of the charge carrier transport and thus FF.

5.2.2. Surface recombination effect

As previously mentioned, the SRH surface recombination velocity can be divided into three categories: front surface, and cSi/i-aSi interface at the p- and n-contact regions. In order to study the individual effect of these three parameters, simulations are conducted by varying the surface recombination velocity from 0.1 to 1×10^6 cm/s. In figure 5.6, the impact of the SRV variation on J_{sc}, V_{oc}, efficiency and FF is described. As with the previous results, the reference cell measurement is defined by the red constant line. From the figures, it is observed that the front SRV has a considerable influence on all the parameters. However, the effect of interface recombination only starts being noticeable from SRV values of more than 100 cm/s. It is interesting to note the FF trend when increasing the front SRV, since it exhibits a minimum. This can be explained by observing that the V_{oc} and I_{sc} decrease at different rates.

The final values selected for the electrical calibration are presented in the next section for two different cases.

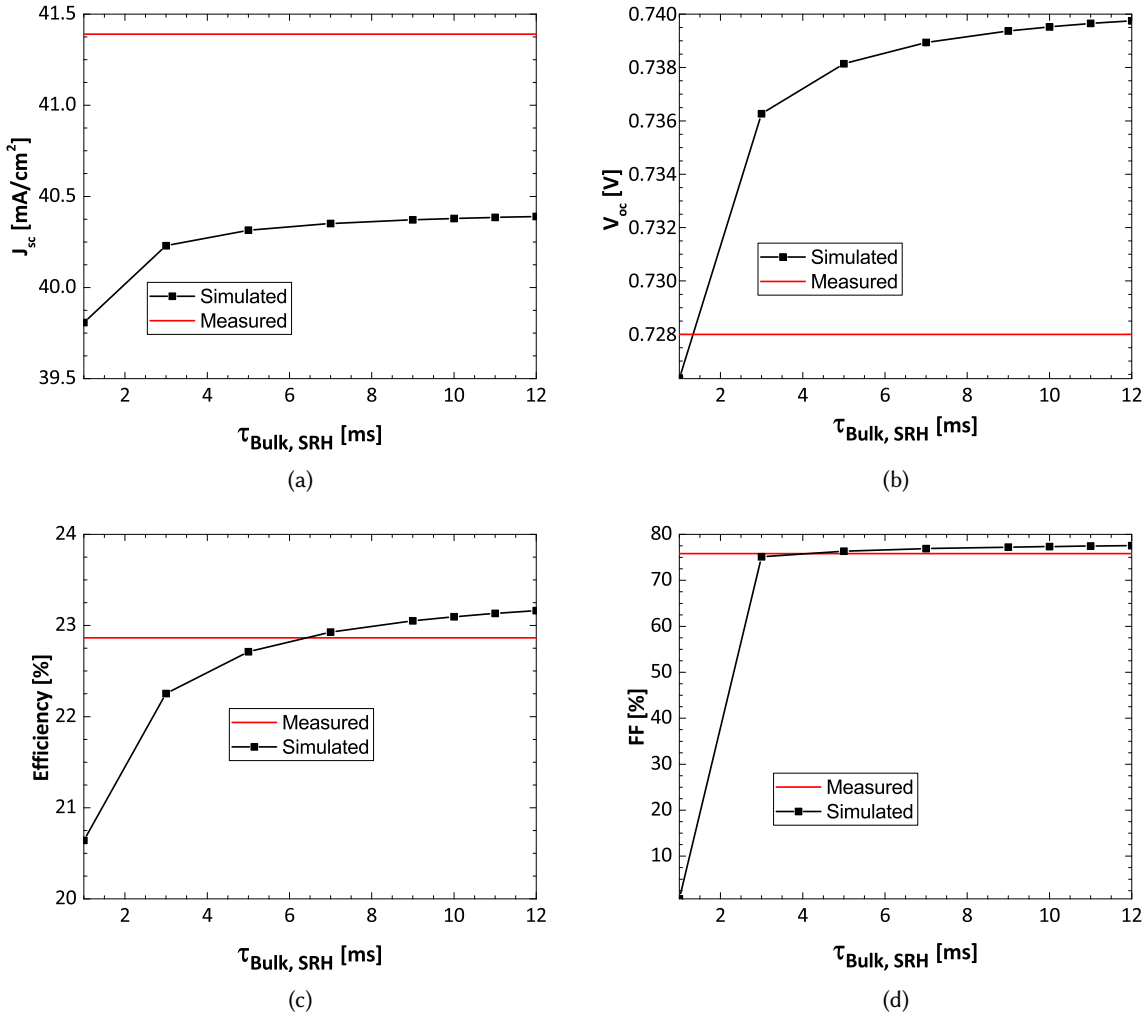

Figure 5.5: Impact of varying SRH bulk lifetime in **a)**Short circuit current **b)**Open circuit voltage **c)**Efficiency and **d)**FF. The red line represents the real device measured parameters.

5.2.3. Calibration comparison: TAT vs non-TAT

The calibration of the aforementioned parameters is done with two different approaches (referring to table 4.16):

- $E_{a,p} < \Delta TCO$, with typical high conductive TCO (ΔTCO= 400meV) $\rightarrow$ Simulated with original model.
- $E_{a,p} > \Delta TCO$, with typical ITO (ΔTCO= 165meV) $\rightarrow$ Simulated with Upgraded model - TAT implemented.

In section 4.3.1, the influence of the TCO conductivity (high carrier concentration) in the FF was studied. It was concluded that the TCO conductivity, represented by ΔTCO, has a considerable effect on the FF. For high ΔTCO, the FF exhibits higher values than for low conductive TCO.

It is thus expected that the FF obtained by the simulation with the original model exceeds the FF measurement retrieved from the reference cell. Indeed, under ideal recombination parameters, the FF reaches nearly 78%, exceeding the measured parameter by 5%. Likewise, the V_{oc} and the efficiency

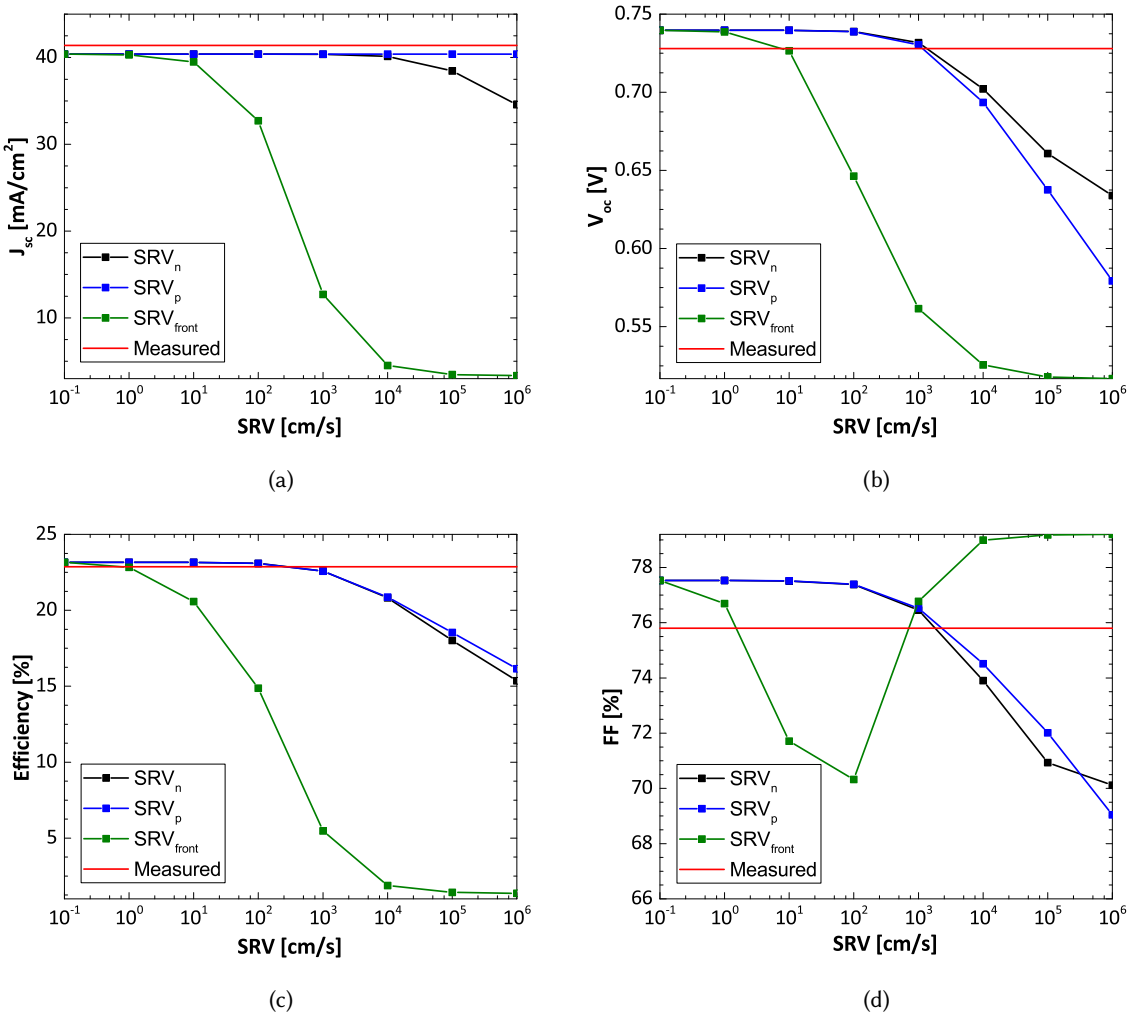

Figure 5.6: Impact of varying SRV (front, cSi/aSi interface) in **a)**Short circuit current **b)**Open circuit voltage **c)**Efficiency and **d)**FF. The red line represents the real device measured parameters.

are also overestimated. Hence, the recombination variables need to be further adjusted in order to reproduce the real device's results. The fitting achieved is shown in figure 5.7a where it can once again be observed that the short circuit current does not match by around 2% of the current, due to the optical calibration mismatch. On the other hand, as seen in table 5.2, the values obtained for FF and V_{oc} adjust well to the measurements. However, to achieve that, it was necessary to select interface SRV values that differ - by two orders of magnitude - from the typical values for passivated surfaces (3-4cm/s), as highlighted in table 5.1. Regarding the dark JV curve, further improvements in the fitting can be done. Here, a mismatch towards higher voltages can be observed, indicating an underestimation of the series resistance.

Next, the calibration is conducted for the model with TAT incorporated. In this case, the ΔTCO used is in accordance with the values reported for ITO in literature. It is worth noticing that, as discussed in chapter 4, it is crucial to implement TAT in the model in order to have valid results for ΔTCO values below 300 meV. Firstly, ideal passivation is assumed, resulting in a lower FF than the one reported by the previous case at higher TCO conductivity. Then, the calibration is performed by

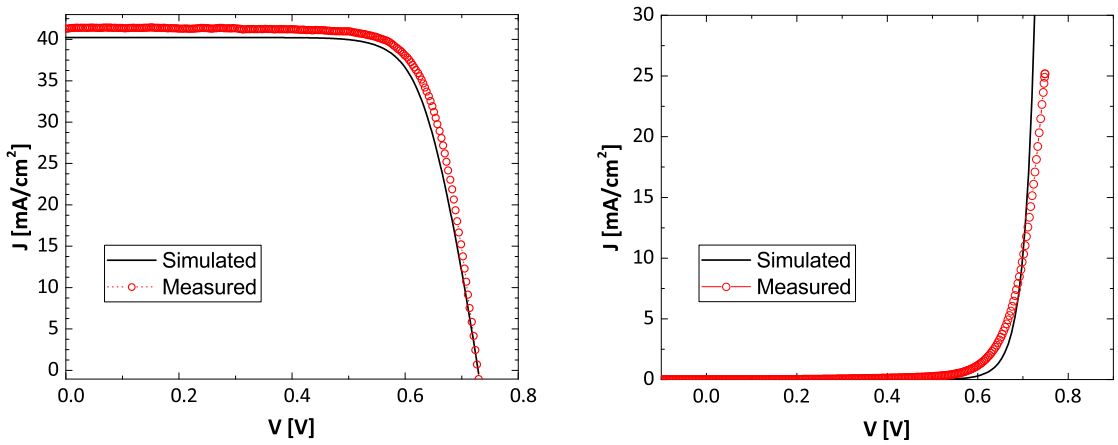

Figure 5.7: Measured and simulated JV curves **a)**Under illumination and **b)**Dark conditions. Fitting performed with original model and ΔTCO=400meV.

means of figures 5.5 and 5.6. The adjustments required in this scenario are minor since the simulated curve initially exhibited considerably similar characteristics to the measured JV.

The final JV fitting is shown in figure 5.8a, adopting the parameter values shown in table 5.1. The ranges in which the parameters are selected are in accordance with the typical reported values for IBC-SHJ structures. Besides this, the dark JV curve presents the same slope as the measured curve. Consequently, it is concluded that the TCO conductivity and the TAT implementation play a fundamental role in the modelling of IBC-SHJ structures presenting aSi contact stacks and low ΔTCO.

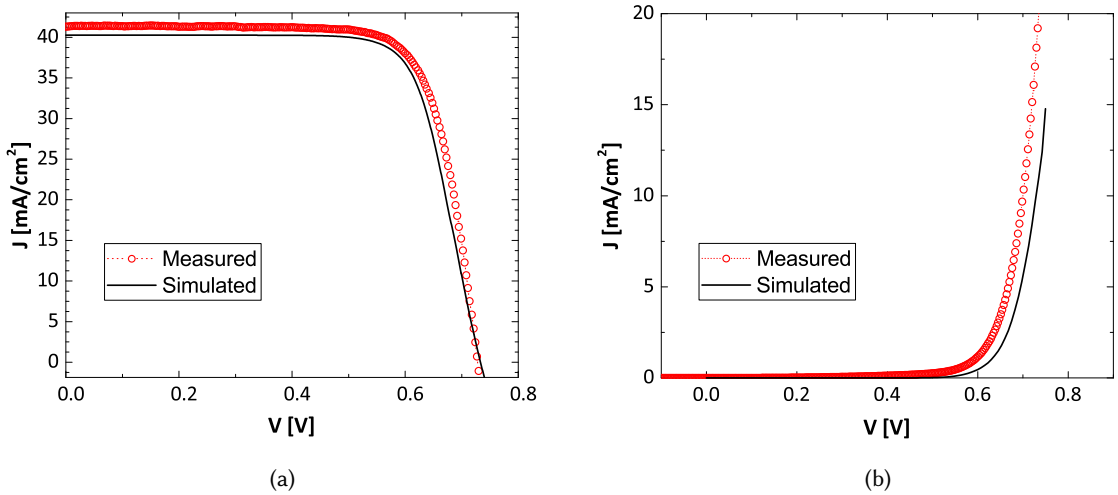

Figure 5.8: Measured and simulated JV curves **a)**Under illumination and **b)**Dark conditions. Fitting performed with upgraded model and ΔTCO=165meV.

Table 5.1: Final calibration parameters for the reference IBC-SHJ cell, for original and upgraded model.

	$\tau_{Bulk,SRH}$	SRV_{front}	SRV_p	SRV_n
Original (no TAT) $\Delta TCO = 400meV$	>7 ms	1.5 cm/s	100 - 1000 cm/s	100 - 1000 cm/s
Upgraded (TAT) $\Delta TCO = 165meV$	>7 ms	1.5 cm/s	0.1-10cm/s	0.1-10cm/s

Table 5.2: Comparison of measured short circuit current, open circuit voltage, FF and efficiency of the real device and the calibrated model simulation results.

	J_{sc} (mA/cm^2)	V_{oc} (V)	FF(%)	Efficiency(%)
Measured	41.4	0.73	75.8	22.8
Fitting Original (no TAT)	40.3	0.73	75.4	22.1
Fitting Upgraded (TAT)	40.3	0.73	75.2	22.2

5.3. Conclusion

Firstly, the optical calibration was performed for short and long wavelength. Regarding the short wavelength range, the thicknesses of the ARC layers - aSi and SiN - were adjusted to fit the measured reflectance curve provided by the reference cell. However, it is found that further improvements can be implemented in the model in order to reproduce the reflectance and EQE for wavelengths from 300 to 500 nm more accurately. Subsequently, light is shed in the possible phenomena that are responsible for the 1% error in the fitting, such as a special front texturing and aSi charge carrier recycling. On the other hand, for long wavelengths, the fitting parameter R_2, introduced in section 3.3, was calibrated to match the reflectance of the cell. After calibration, the simulation produced results that were closely in agreement with the measured EQE and reflectance, with but an additional 1% error. Lastly, it was concluded that further improvements can be implemented in the future, particularly for low wavelengths.

Then, the electrical calibration was performed by adjusting the extrinsic recombination parameters - SRH bulk lifetime and surface recombination velocities of front surface and cSi/aSi interface. Subsequently, the effect of varying these parameters on the cell performance was studied. Respectively, bulk lifetime effect becomes significant for values below 3ms; front recombination velocity considerably affects the performance of the cell from 1cm/s, and the impact of the surface recombination velocity at the interface starts being noticeable from 100-1000cm/s. By means of the these observations, the calibration for the cell was carried out. Two approaches were taken in accordance to the conclusions of chapter 4: 1) BTBT dominant ($\Delta TCO = 400meV$) 2)TAT dominant ($\Delta TCO = 165meV$). The JV fitting (illuminated and dark) was obtained for both cases, concluding that the calibration values for 1), such as SRV_p and SRV_n, differed from typical values for such cell configuration. Conversely, the values obtained for 2) were considered to reproduce the physical characteristics of the device more accurately. Furthermore, the optical generation mismatch was

accounted responsible for the underestimation of the short circuit current.

To conclude, Sentaurus can reproduce detailed opto-electrical behaviour of an IBC-SHJ cell comprising ITO and aSi in its structure. TAT implementation was proven necessary in order to perform the simulations of IBC-SHJ featuring aSi contacts and low TCO carrier concentration. However, further improvements in the optical calibration are suggested.

6

Conclusions and Outlook

In this chapter, the final conclusions of this study will be summarized. The aim is to answer the main research questions presented in 1.1:

1. *Is TAT a dominating carrier transport mechanism in IBC-SHJ?*
2. *Can Sentaurus reproduce in detail the opto-electrical behaviour of an IBC-SHJ with aSi and ITO contact stacks?*

Throughout chapter 2 and 3, the physics and the modelling of semiconductor devices, particularly IBC-SHJ, were discussed. It was concluded that thermionic emission, tunneling and TAT tunneling are charge carrier transport mechanisms in heterojunctions, and thus relevant for IBC-SHJ contact stack - where 3 different materials are present: cSi, aSi and TCO. This raises the need of understanding the relevance of the aforementioned transport mechanisms in this type of configurations and what the impact of the material properties is. Therefore, the subsequent study was carried out.

6.1. TAT in IBC-SHJ

In section 4, the implementation of TAT in TCAD Sentaurus was discussed. Accordingly, a range of available TAT models in Sentaurus were outlined in section 4.1 from which non-local TAT model was selected - due to its accuracy for calculating tunneling in abrupt heterojunctions. Such model required further adjustments in the mesh - as described in section 4.1.2 - in order to guarantee valid numerical results.

To answer the first research question, three sub-questions are raised:

- 1.1) *In which contact stack layer is TAT mechanism more relevant for effective carrier collection?*
- 1.2) *How does the aSi trap distribution influence the charge carrier transport?*
- 1.3) *How does the aSi trap energy level influence the charge carrier transport?*

After the successful implementation of TAT in section 4.3.1, the influence of the TCO and the aSi in the carrier transport of IBC-SHJ was studied. Firstly, it was observed that the band alignment at

the p-contact, was considerably sensitive to changes in TCO carrier concentration (represented by ΔTCO, figure 4.5), thus compromising the band-to-band tunneling path. Indeed, it was observed that for good band alignments, being $E_{a,p} < \Delta TCO$, BTB tunneling dominates the transport. However, for $E_{a,p} > \Delta TCO$, TAT is the dominating transport mechanism. Therefore question number 1.1 was answered.

Regarding question number 1.2, it was observed that the aSi defect density affects the transport. A study was conducted, considering each individual aSi trap distribution (described in section 2.2.2), namely, the valence band tail (VBT), conduction band tail (CBT) and dangling bonds ($DB^{+/0}$ and $DB^{0/-}$). It was observed that by increasing the trap density at the VBT, the FF decreases. Conversely, augmenting the defect density of the dangling bonds may have a strong positive impact on the FF.

Finally, question number 1.3. was addressed, concluding that traps at an energy range of 0.5-0.7eV over the valence band, greatly contribute to the charge carrier transport, as summarized in figure 4.17. In addition, light is shed on aSi defect manipulation techniques [69], showing that, unlike for other types of configurations, light induced degradation and bias voltage in aSi, might make a positive contribution in IBC-SHJ by increasing the defects in the aforementioned energy range.

It is concluded that TAT plays an important role in IBC-SHJ carrier transport. Moreover, the study suggests that, increasing the trap density at an energy level over 0.5-0.7eV from the valence band, would contribute positively to the hole transport, and thus would increase FF.

6.2. Opto-electrical calibration of IBC-SHJ

The model calibration of the reference IBC-SHJ cell was discussed in order to answer the question: *Can Sentaurus reproduce in detail the opto-electrical behaviour of an IBC-SHJ with aSi and ITO contact stacks?*

Firstly, the optical calibration was performed for short and long wavelength. Regarding the short wavelength range, the thicknesses of the ARC layers - aSi and SiN - were adjusted to fit the measured reflectance curve provided by the reference cell. However, it is found that further improvements can be implemented in the model in order to reproduce the reflectance and EQE for wavelengths from 300 to 500 nm more accurately. Subsequently, light is shed in the possible phenomena that are responsible for the 1% error in the fitting, such as a special front texturing and aSi charge carrier recycling. On the other hand, for long wavelengths, the fitting parameter R_2, introduced in section 3.3, was calibrated to match the reflectance of the cell. After calibration, the simulation produced results that were closely in agreement with the measured EQE and reflectance, with but an additional 1% error. Lastly, it was concluded that further improvements can be implemented in the future, particularly for low wavelengths.

Then, the electrical calibration was performed by adjusting the extrinsic recombination parameters - SRH bulk lifetime and surface recombination velocities of front surface and cSi/aSi interface. Subsequently, the effect of varying these parameters on the cell performance was studied. Respectively, bulk lifetime effect becomes significant for values below 3ms; front recombination velocity considerably affects the performance of the cell from 1cm/s, and the impact of the surface recombination velocity at the interface starts being noticeable from 100-1000cm/s. By means of the these observations, the calibration for the cell was carried out. Two approaches were taken in accor-

dance to the conclusions of chapter 4: 1) BTBT dominant ($\Delta TCO = 400meV$) 2)TAT dominant ($\Delta TCO = 165meV$). The JV fitting (illuminated and dark) was obtained for both cases, concluding that the calibration values for 1), such as SRV_p and SRV_n, differed from typical values for such cell configuration. Conversely, the values obtained for 2) were considered to reproduce the physical characteristics of the device more accurately. Furthermore, the optical generation mismatch was accounted responsible for the underestimation of the short circuit current.

To conclude, Sentaurus can reproduce detailed opto-electrical behaviour of an IBC-SHJ cell comprising ITO and aSi in its structure. TAT implementation was proven necessary in order to perform the simulations of IBC-SHJ featuring aSi contacts and low TCO carrier concentration. However, further improvements in the optical calibration are suggested.

6.3. Outlook

After the conclusions drawn from this study, several research lines are opened. It is suggested to investigate the defect dynamics on aSi in IBC-SHJ, by conducting experiments with light soaking, annealing and applying a bias potential.

Following the research line of this study, an analysis of the transport mechanisms in front contacted SHJ can be conducted. To this end, it is recommended to investigate the influence of the TCO carrier concentration and asi defect distribution in this configuration. Thus, enabling a comparison of transport in SHJ for both cell architectures.

Regarding optical modelling, in order to avoid an underestimation of the optical generation profile in cells featuring aSi at the front, it is recommended to include the carrier recycling effect.

Bibliography

[1] Fraunhofer Institute for Solar and Systems. Photovoltaics report. (June):p. 43, 2018.

[2] L-2016.03. *Sentaurus ™ Device User*, 2014.

[3] Paul Procel, Guangtao Yang, Olindo Isabella, and Miro Zeman. Theoretical evaluation of contact stack for high efficiency ibc-shj solar cells. *Solar Energy Materials and Solar Cells*, 186:66 – 77, 2018. ISSN 0927-0248. doi: https://doi.org/10.1016/j.solmat.2018.06.021.

[4] Andreas Gehring and Siegfried Selberherr. Modeling of Tunneling Current and Gate Dielectric Reliability for Nonvolatile Memory Devices. *IEEE Transactions on Device and Materials Reliability*, 4(3):306–319, September 2004. ISSN 1530-4388. doi: 10.1109/TDMR.2004.836727. Retrieved from: http://ieeexplore.ieee.org/document/1369191/.

[5] Raghu V.K. Chavali, Stefaan De Wolf, and Muhammad A. Alam. Device physics underlying silicon heterojunction and passivating-contact solar cells: A topical review. *Progress in Photovoltaics: Research and Applications*, , 2018. ISSN 1099159X. doi: 10.1002/pip.2959.

[6] Bhushan Sopori. Thin-film Silicon Solar Cells. *Handbook of Photovoltaic Science and Engineering*, 8:1–51, 2003. doi: 10.1016/B978-0-12-385934-1.00008-8.

[7] Ruud E I Schropp and Miro Zeman. Amorphous and Microcrystalline Silicon Solar Cells: Modeling, Materials and Device Technology. *Science*, :19–19, 1998. ISSN 1098-6596. doi: 10.1007/978-1-4615-5631-2. Retrieved from: http://books.google.com/books?id=cowidBsuzw8C&pgis=1.

[8] Andreas Klein, Christoph Körber, Andŕe Wachau, Frank Säuberlich, Yvonne Gassenbauer, Steven P. Harvey, Diana E. Proffit, and Thomas O. Mason. Transparent conducting oxides for photovoltaics: Manipulation of fermi level,work function and energy band alignment. *Materials*, 3(11):4892–4914, 2010. ISSN 19961944. doi: 10.3390/ma3114892.

[9] Eiji Kobayashi, Stefaan De Wolf, Jacques Levrat, Antoine Descoeudres, Matthieu Despeisse, Franz Josef Haug, and Christophe Ballif. Increasing the efficiency of silicon heterojunction solar cells and modules by light soaking. *Solar Energy Materials and Solar Cells*, 173(June):43–49, 2017. ISSN 09270248. doi: 10.1016/j.solmat.2017.06.023. Retrieved from: https://doi.org/10.1016/j.solmat.2017.06.023.

[10] [IEA-PVPS] - Internation Energy Agency Photovoltaics Power Systems. 2018 Snapshot of Global Photovoltaic Markets - IEA PVPS. :1–16, 2018. doi: 978-3-906042-58-9. Retrieved from: http://www.iea-pvps.org/fileadmin/dam/public/report/statistics/.

[11] ITRPV. International Technology Roadmap for Photovoltaic (ITRPV). Technical Report March, 2018. Retrieved from: http://www.itrpv.net.

[12] Silvia, Antoine Descoeudres, Jonas Geissbuhler, Stefaan De Wolf, and Christophe Ballif. Back-Contacted Silicon Heterojunction Solar Cells With Efficiency 21%. *IEEE Journal of Photovoltaics*, 4(4):1046–1054, 2014. ISSN 2156-3381. doi: 10.1109/JPHOTOV.2014.2320586.

[13] Guangtao Yang, Andrea Ingenito, Olindo Isabella, and Miro Zeman. IBC c-Si solar cells based on ion-implanted poly-silicon passivating contacts. *Solar Energy Materials and Solar Cells*, :1–7, 2016. ISSN 09270248. doi: 10.1016/j.solmat.2016.05.041. Retrieved from: http://dx.doi.org/10.1016/j.solmat.2016.05.041.

[14] Kunta Yoshikawa, Wataru Yoshida, Toru Irie, Hayato Kawasaki, Katsunori Konishi, Hirotaka Ishibashi, Tsuyoshi Asatani, Daisuke Adachi, Masanori Kanematsu, Hisashi Uzu, and Kenji Yamamoto. Exceeding conversion efficiency of 26% by heterojunction interdigitated back contact solar cell with thin film Si technology. *Solar Energy Materials and Solar Cells*, 173(June):37–42, 2017. ISSN 09270248. doi: 10.1016/j.solmat.2017.06.024.

[15] Armin Richter, Stefan W. Glunz, Florian Werner, Jan Schmidt, and Andres Cuevas. Improved quantitative description of Auger recombination in crystalline silicon. *Physical Review B*, 86 (16):165202, 2012. ISSN 1098-0121. doi: 10.1103/PhysRevB.86.165202. Retrieved from: http://link.aps.org/doi/10.1103/PhysRevB.86.165202.

[16] Kazushige Horio and Hisayoshi Yanai. Numerical Modeling of Heterojunctions Including the Thermionic Emission Mechanism at the Heterojunction Interface. *IEEE Transactions on Electron Devices*, 37(4):1093–1098, 1990. ISSN 15579646. doi: 10.1109/16.52447.

[17] Basic Principles. *Semiconductor physics and devices*, volume 9. McGraw-Hill, 2006. ISBN 0072321075. doi: 10.1016/S1369-7021(06)71498-5. Retrieved from: http://linkinghub.elsevier.com/retrieve/pii/S1369702106714985.

[18] MeiKei Ieong, P.M. Solomon, S.E. Laux, H.-S.P. Wong, and D. Chidambarrao. Comparison of raised and Schottky source/drain MOSFETs using a novel tunneling contact model. *International Electron Devices Meeting 1998. Technical Digest (Cat. No.98CH36217)*, :733–736, 1998. ISSN 0163-1918. doi: 10.1109/IEDM.1998.746461. Retrieved from: http://ieeexplore.ieee.org/document/746461/.

[19] Ramachandran Ammapet Vijayan, Stephanie Essig, Stefaan De Wolf, Bairava Ganesh Ramanathan, Philipp Loper, Christophe Ballif, and Muthubalan Varadharajaperumal. Hole-Collection Mechanism in Passivating Metal-Oxide Contacts on Si Solar Cells: Insights from Numerical Simulations. *IEEE Journal of Photovoltaics*, 8(2):473–482, 2018. ISSN 21563381. doi: 10.1109/JPHOTOV.2018.2796131.

[20] Christoph Messmer, Martin Bivour, Jonas Schon, Stefan W. Glunz, and Martin Hermle. Numerical Simulation of Silicon Heterojunction Solar Cells Featuring Metal Oxides as Carrier-

Selective Contacts. *IEEE Journal of Photovoltaics*, 8(2):456–464, 2018. ISSN 21563381. doi: 10.1109/JPHOTOV.2018.2793762.

[21] F. Jiménez-Molinos, F. Gámiz, A. Palma, P. Cartujo, and J. A. López-Villanueva. Direct and trap-assisted elastic tunneling through ultrathin gate oxides. *Journal of Applied Physics*, 91(8): 5116–5124, 2002. ISSN 00218979. doi: 10.1063/1.1461062.

[22] B. Ricco, G. Gozzi, and M. Lanzoni. Modeling and simulation of stress-induced leakage current in ultrathin sio/sub 2/ films. *IEEE Transactions on Electron Devices*, 45(7):1554–1560, July 1998. ISSN 0018-9383. doi: 10.1109/16.701488.

[23] Daniele Ielmini, Alessandro S. Spinelli, Andrea L. Lacaita, Andrea Martinelli, and Gabriella Ghidini. A recombination- and trap-assisted tunneling model for stress-induced leakage current. *Solid-State Electronics*, 45(8):1361–1369, 2001. ISSN 00381101. doi: 10.1016/S0038-1101(01)00173-3.

[24] Wai Jyh Chang, Mau Phon Houng, and Yeong Her Wang. Simulation of stress-induced leakage current in silicon dioxides: A modified trap-assisted tunneling model considering Gaussian-distributed traps and electron energy loss. *Journal of Applied Physics*, 89(11 I):6285–6293, 2001. ISSN 00218979. doi: 10.1063/1.1367399.

[25] Mau Phon Houng, Yeong Her Wang, and Wai Jyh Chang. Current transport mechanism in trapped oxides: A generalized trap-assisted tunneling model. *Journal of Applied Physics*, 86(3): 1488–1491, 1999. ISSN 00218979. doi: 10.1063/1.370918.

[26] Andreas Gehring. *Simulation of Tunneling in Semiconductor Devices*. PhD thesis, Technischen Universität Wien, 2003. Retrieved from: http://www.iue.tuwien.ac.at/phd/gehring/.

[27] Frank Feldmann, Martin Bivour, Christian Reichel, Martin Hermle, and Stefan W. Glunz. Passivated rear contacts for high-efficiency n-type Si solar cells providing high interface passivation quality and excellent transport characteristics. *Solar Energy Materials and Solar Cells*, 120(PART A):270–274, 2014. ISSN 09270248. doi: 10.1016/j.solmat.2013.09.017.

[28] K. Masuko, M. Shigematsu, T. Hashiguchi, D. Fujishima, M. Kai, N. Yoshimura, T. Yamaguchi, Y. Ichihashi, T. Mishima, N. Matsubara, T. Yamanishi, T. Takahama, M. Taguchi, E. Maruyama, and S. Okamoto. Achievement of More Than 25% Conversion Efficiency With Crystalline Silicon Heterojunction Solar Cell. *IEEE Journal of Photovoltaics*, 4(6):1433–1435, 2014. ISSN 2156-3381. doi: 10.1109/JPHOTOV.2014.2352151.

[29] Luana Mazzarella, Ana Belen Morales-Vilches, Max Hendrichs, Simon Kirner, Lars Korte, Rutger Schlatmann, and Bernd Stannowski. Nanocrystalline n-Type Silicon Oxide Front Contacts for Silicon Heterojunction Solar Cells: Photocurrent Enhancement on Planar and Textured Substrates. *IEEE Journal of Photovoltaics*, 8(1):70–78, 2017. ISSN 21563381. doi: 10.1109/JPHOTOV.2017.2770164.

[30] Bertrand Paviet-Salomon, Andrea Tomasi, Damien Lachenal, Loris Barraud, Antoine Descoeudres, Gabriel Christmann, Nicolas Badel, Antonin Faes, Hikaru Watanabe, Sylvain Nicolay, Stefaan De Wolf, B. Strahm, Matthieu Despeisse, and Christophe Ballif. Development of photolithography-free, large-area, back-contacted silicon heterojunction solar cells. In *Proceedings of the 7th Workshop on Back Contact Solar Cell and Module Technology*, 2015.

[31] Luana Mazzarella, Simon Kirner, Onno Gabriel, Sebastian S. Schmidt, Lars Korte, Bernd Stannowski, Bernd Rech, and Rutger Schlatmann. Nanocrystalline silicon emitter optimization for Si-HJ solar cells: Substrate selectivity and CO ₂ plasma treatment effect. *Physica Status Solidi (a)*, 214(2):1532958, 2017. ISSN 18626300. doi: 10.1002/pssa.201532958. Retrieved from: http://doi.wiley.com/10.1002/pssa.201532958.

[32] Antoine Descoeudres, Zachary C. Holman, Loris Barraud, Sophie Morel, Stefaan De Wolf, and Christophe Ballif. >21% Efficient Silicon Heterojunction Solar Cells on n- and p-Type Wafers Compared. *IEEE Journal of Photovoltaics*, 3(1):83–89, 2013. ISSN 2156-3381. doi: 10.1109/JPHOTOV.2012.2209407. Retrieved from: http://ieeexplore.ieee.org/lpdocs/epic03/wrapper.htm?arnumber=6263260.

[33] Z.C. Holman, A. Descoeudres, L. Barraud, F.Z. Fernandez, J.P. Seif, S. De Wolf, and C. Ballif. Current Losses at the Front of Silicon Heterojunction Solar Cells. *IEEE Journal of Photovoltaics*, 2(1):7–15, 2012. ISSN 2156-3381. doi: 10.1109/JPHOTOV.2011.2174967.

[34] A. Smets and M. van de Sanden. Relation of the Si-H stretching frequency to the nanostructural Si-H bulk environment. *Physical Review B*, 76(7):073202, 2007. ISSN 1098-0121. doi: 10.1103/PhysRevB.76.073202. Retrieved from: http://link.aps.org/doi/10.1103/PhysRevB.76.073202.

[35] R.A. Street. Hydrogenated amorphous silicon. *Cambridge University Press*, :62–91, 1991. ISSN 0717-6163. doi: 10.1007/s13398-014-0173-7.2.

[36] T F Schulze. *Structural, electronic and transport properties of amorphous/crystalline silicon heterojunctions*. PhD thesis, TU Berlin, 2011.

[37] M. J. Powell and S. C. Deane. Improved defect-pool model for charged defects in amorphous silicon. *Physical Review B*, 48(15):10815–10827, 1993. ISSN 01631829. doi: 10.1103/PhysRevB.48.10815.

[38] Elvira Fortunato, David Ginley, Hideo Hosono, and David C Paine. Transparent conducting oxides for photovoltaics. *MRS Bulletin*, 32(3):242–247, 2007. doi: 10.1557/mrs2007.29.

[39] Ana Kanevce and Wyatt K. Metzger. The role of amorphous silicon and tunneling in heterojunction with intrinsic thin layer (HIT) solar cells. *Journal of Applied Physics*, 105(9), 2009. ISSN 00218979. doi: 10.1063/1.3106642.

[40] Felix Haase, Soren Schafer, Christina Klamt, Fabian Kiefer, Jan Krugener, Rolf Brendel, and Robby Peibst. Perimeter Recombination in 25%-Efficient IBC Solar Cells With Passivating POLO

Contacts for Both Polarities. *IEEE Journal of Photovoltaics*, 8(1):23–29, 2017. ISSN 21563381. doi: 10.1109/JPHOTOV.2017.2762592.

[41] Christian Reichel, Filip Granek, Martin Hermle, and Stefan W Glunz. Back-contacted back-junction n-type silicon solar cells featuring an insulating thin film for decoupling charge carrier collection and metallization geometry. *Progress in Photovoltaics: Research and Applications*, 21 (5):1063–1076, March 2013. ISSN 10627995. doi: 10.1002/pip.2204.

[42] Junichi Nakamura, Naoki Asano, Takeshi Hieda, Chikao Okamoto, Hiroyuki Katayama, and Kyotaro Nakamura. Development of heterojunction back contact Si solar cells. *IEEE Journal of Photovoltaics*, 4(6):1491–1495, 2014. ISSN 21563381. doi: 10.1109/JPHOTOV.2014.2358377.

[43] Pablo Ortega, Eric Calle, Guillaume von Gastrow, Päivikki Repo, David Carrió, Hele Savin, and Ramón Alcubilla. High-efficiency black silicon interdigitated back contacted solar cells on p-type and n-type c-Si substrates. *Progress in Photovoltaics: Research and Applications*, 23(11): 1448–1457, November 2015. ISSN 10627995. doi: 10.1002/pip.2664.

[44] Constantin Bulucea. Recalculation of Irvin's resistivity curves for diffused layers in silicon using updated bulk resistivity data. *Solid State Electronics*, 36(4):489–493, 1993. ISSN 00381101. doi: 10.1016/0038-1101(93)90257-Q.

[45] Meijun Lu, Stuart Bowden, Ujjwal Das, and Robert Birkmire. a-Si/c-Si heterojunction for interdigitated back contact solar cell. *Proceedings of the 22 nd European Photovoltaic Solar Energy Conference, Milano, Italie*, 22(September):924–927, 2007. ISSN 01608371. doi: 10.1109/PVSC.2008.4922757.

[46] Rolf Stangl, Caspar Leendertz, and Jan Haschke. Numerical simulation of solar cells and solar cell characterization methods: the open-source on demand program afors-het. In Radu D Rugescu, editor, *Solar Energy*, chapter 14. IntechOpen, Rijeka, 2010. doi: 10.5772/8073.

[47] S. Michael, a.D. Bates, and M.S. Green. Silvaco ATLAS as a solar cell modeling tool. *Conference Record of the Thirty-first IEEE Photovoltaic Specialists Conference, 2005.*, :719–721, 2005. ISSN 0160-8371. doi: 10.1109/PVSC.2005.1488232.

[48] *Open source graphical user interface in Matlab for two-dimensional simulations solving the fully coupled semiconductor equations using COMSOL*, 2010.

[49] A. Fell. A free and fast three-dimensional/two-dimensional solar cell simulator featuring conductive boundary and quasi-neutrality approximations. *IEEE Transactions on Electron Devices*, 60(2):733–738, Feb 2013. ISSN 0018-9383. doi: 10.1109/TED.2012.2231415.

[50] Pierre Saint-Cast, Milan Padilla, Achim Kimmerle, and Christian Reichel. An analytical model for interdigitated back contact solar cells. *IEEE Journal of Photovoltaics*, 4(1):114–121, 2014. ISSN 21563381. doi: 10.1109/JPHOTOV.2013.2287771.

[51] Models for numerical device simulations of crystalline silicon solar cells - A review, 2011. ISSN 15698025.

[52] Paul Procel, Andrea Ingenito, Raffaele De Rose, Silvio Pierro, Felice Crupi, Marco Lanuzza, Giuseppe Cocorullo, Olindo Isabella, and Miro Zeman. Opto-electrical modelling and optimization study of a novel IBC c-Si solar cell. *Progress in Photovoltaics: Research and Applications*, 25(6):452–469, June 2017. ISSN 10627995. doi: 10.1002/pip.2874. Retrieved from: http://dx.doi.org/10.1002/pip.2874http://doi.wiley.com/10.1002/pip.2874.

[53] Ayesha A Al-Shouq and Adel B Gougam. *Review of Interdigitated Back Contacted Full Heterojunction Solar Cell (IBC-SHJ): A Simulation Approach*, 309–327. Springer International Publishing, Cham, 2016. ISBN 978-3-319-20481-9. doi: 10.1007/978-3-319-20481-9_17.

[54] Pv lighthouse resistivity calculator. https://www.pvlighthouse.com.au/resistivity.

[55] David Thorp and Stuart R. Wenham. Ray-tracing of arbitrary surface textures for light-trapping in thin silicon solar cells. *Solar Energy Materials and Solar Cells*, 48(1-4):295–301, 1997. ISSN 09270248. doi: 10.1016/S0927-0248(97)00116-5.

[56] Victor Moroz, Joanne Huang, Kapila Wijekoon, and David Tanner. Experimental and theoretical analysis of the optical behavior of textured silicon wafers. In *2011 37th IEEE Photovoltaic Specialists Conference*, 002900–002905, 2011. ISBN 978-1-4244-9965-6. doi: 10.1109/PVSC.2011.6186552.

[57] M. Born and Emil Wolf. *Principles of optics: Electromagnetic Theory of Propagation, Interference and Diffraction of Light*. 1994. ISBN 0521642221. doi: 10.1016/S0030-3992(00)00061-X.

[58] Andreas Fell, Keith R. McIntosh, Pietro P. Altermatt, Gaby J. M. Janssen, Rolf Stangl, Anita Ho-Baillie, Heiko Steinkemper, Johannes Greulich, Matthias Muller, Byungsul Min, Kean C. Fong, Martin Hermle, Ingrid G. Romijn, and Malcolm D. Abbott. Input Parameters for the Simulation of Silicon Solar Cells in 2014. *IEEE Journal of Photovoltaics*, 5(4):1250–1263, July 2015. ISSN 2156-3381. doi: 10.1109/JPHOTOV.2015.2430016.

[59] Pietro P. Altermatt, Andreas Schenk, Frank Geelhaar, and Gernot Heiser. Reassessment of the intrinsic carrier density in crystalline silicon in view of band-gap narrowing. *Journal of Applied Physics*, 93(3):1598–1604, 2003. ISSN 00218979. doi: 10.1063/1.1529297.

[60] Andreas Schenk. Finite-temperature full random-phase approximation model of band gap narrowing for silicon device simulation. *Journal of Applied Physics*, 84(7):3684–3695, 1998. ISSN 00218979. doi: 10.1063/1.368545.

[61] D. B.M. Klaassen. A unified mobility model for device simulation-I. Model equations and concentration dependence. *Solid State Electronics*, 35(7):953–959, 1992. ISSN 00381101. doi: 10.1016/0038-1101(92)90325-7.

[62] C. Canali, G. Majni, R. Minder, and G. Ottaviani. Electron and Hole Drift Velocity Measurements in Silicon and Their Empirical Relation to Electric Field and Temperature. *IEEE Transactions on Electron Devices*, 22(11):1045–1047, 1975. ISSN 15579646. doi: 10.1109/T-ED.1975.18267.

[63] D. Schroeder. *Modelling of Interface Carrier Transport for Device Simulation*. 1994. ISBN 978-3-7091-7368-8. doi: 10.1007/978-3-7091-6644-4.

[64] G. A.M. Hurkx, D. B.M. Klaassen, and M. P.G. Knuvers. A New Recombination Model for Device Simulation Including Tunneling. *IEEE Transactions on Electron Devices*, , 1992. ISSN 15579646. doi: 10.1109/16.121690.

[65] A. Schenk. A model for the field and temperature dependence of Shockley-Read-Hall lifetimes in silicon. *Solid State Electronics*, , 1992. ISSN 00381101. doi: 10.1016/0038-1101(92)90184-E.

[66] L. Colalongo, M. Valdinoci, G. Baccarani, P. Migliorato, G. Tallarida, and C. Reita. Numerical analysis of poly-TFTs under off conditions. *Solid-State Electronics*, 41(4):627–633, 1997. ISSN 00381101. doi: 10.1016/S0038-1101(96)00201-8.

[67] R. Varache, C. Leendertz, M.E. Gueunier-Farret, J. Haschke, D. Muñoz, and L. Korte. Investigation of selective junctions using a newly developed tunnel current model for solar cell applications. *Solar Energy Materials and Solar Cells*, , 2015. ISSN 09270248. doi: 10.1016/j.solmat.2015.05.014.

[68] Joost Willemen. *Modelling of Amorphous SIlicon Single- and Multi-Junction Solar Cells*. PhD thesis, Delft University of Technology, 1998.

[69] J. Melskens, M. Schouten, R. Santbergen, M. Fischer, R. Vasudevan, D. J. Van Der Vlies, R. J.V. Quax, S. G.M. Heirman, K. Jäger, V. Demontis, M. Zeman, and A. H.M. Smets. In situ manipulation of the sub gap states in hydrogenated amorphous silicon monitored by advanced application of Fourier transform photocurrent spectroscopy. *Solar Energy Materials and Solar Cells*, 129:70–81, 2014. ISSN 09270248. doi: 10.1016/j.solmat.2014.03.022. Retrieved from: http://dx.doi.org/10.1016/j.solmat.2014.03.022.

[70] Christopher R. Wronski and Xinwei Niu. The Limited Relevance of SWE Dangling Bonds to Degradation in High-Quality a-Si:H Solar Cells. *IEEE Journal of Photovoltaics*, 4(3):778–784, may 2014. ISSN 2156-3381. doi: 10.1109/JPHOTOV.2014.2311498. Retrieved from: http://ieeexplore.ieee.org/document/6783732/.

[71] A Paduthol, M.K. Juhl, Ziv Hameiri, Gizem Nogay, Phillip Löper, and Thorsten Trupke. Efficient carrier injection from amorphous silicon into crystalline silicon determined from photoluminescence. *33rd European Photovoltaic Solar Energy Conference and Exhibition*, (April):238–241, 2017. ISSN 10627995. doi: 10.4229/EUPVSEC20172017-2AO.4.2.

[72] Tristan Leigh Temple. Optical properties of metal nanoparticles and their influence on silicon solar cells. *Philosophy*, :186, 2009.